Chemical characterization of Gd(III) and Mn(II) complexes formed with chelating ligands containing malonate pendants

Thesis for the Degree of Doctor of Philosophy (PhD)

Abraham Estifanos Debretsion
Supervisor: Dr. Ferenc K. Kálmán

UNIVERSITY OF DEBRECEN
Doctoral Council for Natural Sciences and Engineering
Doctoral School of Chemistry
Debrecen, 2025

Hereby I declare that I have prepared this thesis within the Doctoral Council for Natural Sciences and Engineering, Doctoral School of Chemistry, University of Debrecen in order to obtain a PhD Degree in Natural Sciences / Engineering at Debrecen University.
The results published in the thesis are not reported in any other PhD theses.

Debrecen, 2025. 06. 12.

…….
signature of the candidate

Hereby I confirm that Abraham Estifanos Debretsion candidate conducted his studies with my supervision within the Coordination Chemistry Doctoral Program of the Doctoral School of Chemistry between 2021 and 2025. The independent studies and research work of the candidate significantly contributed to the results published in the thesis.
I also declare that the results published in the thesis are not reported in any other theses.
I support the acceptance of the thesis.

Debrecen, 2025. 06. 12. ……
signature of the supervisor

Chemical characterization of Gd(III) and Mn(II) complexes formed with chelating ligands containing malonate pendants

Dissertation submitted in partial fulfilment of the requirements for the doctoral (PhD) degree
in Chemistry

Written by Abraham Estifanos Debretsion certified organic chemist.

Prepared in the framework of the Doctoral School of Chemistry, University of Debrecen, Coordination Chemistry programme.

Dissertation supervisor: Dr. Ferenc Krisztián Kálmán

The official opponents of the dissertation:

Dr. ……..
Dr. ……..

The evaluation board:

chairperson:	Dr. ……..
members:	Dr. ……..
	Dr. ……..
	Dr. ……..
	Dr. ……..

The date and venue of the dissertation defence: …20 ……

Acknowledgement

Above all, I would like to express my deepest gratitude to my supervisor, Dr. Ferenc Kálmán, and my co-supervisor, Dr. Szilvia Bunda, for your extraordinary mentorship and constant support throughout my project. I am really shaped my progress as a researcher due to your deep passion and hardworking attitude for scientific research. This thesis would have been difficult to complete without your help, guidance and encouragement.

I am also grateful to the Department of Physical Chemistry at the University of Debrecen, especially to Prof. Imre Tóth and Dr. Gyula Tircsó, with their students, for creating a supportive and collaborative atmosphere. Special thanks to Ms. Katalin Takács for keeping the lab well-organized and giving technical assistance throughout the project.

I am very thankful to Prof. Éva Jakab-Tóth and Dr. Zoltán Garda, for dedicating their time and offering thoughtful, valuable comments on my work and Dr. Norbert Lihi, for his assistance with the DFT calculation.

Finally, my deepest gratitude goes to my wife Yohana Tecleab, my daughters Sara Abraham and Eliana Abraham, for your patience and love while I am away from you to do my PhD. To my father Estifanos Debretsion and my mother Mbraq Habte, thank you for your love and endless encouragement. To my brothers Gidewon, Medhanie, Ambasager, Filmon, Biniam, and my sister Bisrat, thank you for your constant moral support. I could not have accomplished my study without your love and emotional support. I acknowledge the support of the Doctoral School of Chemistry (University of Debrecen) in the framework of Stipendium Hungaricum Scholarship.

Contents

I. Introduction

Over the past forty years, magnetic resonance imaging (MRI) has emerged as a highly effective diagnostic technique for soft tissues of human anatomy, physiology, and pathophysiology. MRI is a medical imaging technique with high spatial resolution and no ionizing radiation.[1,2] MRI uses the principle of nuclear magnetic resonance (NMR), thus radio frequency generates diagnostic images thanks to the interaction of that with water protons. Since, circa 60% of our body is water, MRI can provide images of various tissue types by measuring the T_1 (longitudinal) and T_2 (transverse) relaxation rates of protons due to the different water content in the healthy and diseased tissues.[3,4]

When a powerful magnetic field (B_0) is applied, the spin (magnetic moment) of water protons aligns to be either parallel or anti-parallel with that, however most protons line up parallel to B_0 as this provides a lower energy state. When radio waves are pulsed through the human body, the hydrogen atoms of the water (and fat) are excited and spin out of their original position. As the radiation is turned off, the nuclei return to their original alignment and send back signals by releasing their energy in a process called relaxation (T_1 and T_2). These signals are converted to a digital format on a screen. The relaxation rate of the protons can be enhanced by means of the so-called MRI contrast agents (CAs) administered intravenously to the patients, thus improving the quality of the MRI images.

In the U.S., the demand for gadolinium-based contrast agents has grown to approximately 30% to 45% of all clinical MRI diagnoses every year.[5] Most of the MRI contrast agents in the market are gadolinium-

based contrast agents (GBCAs), even though manganese-based one also existed.[6]

The general criteria for metal chelates to be MRI contrast agents are high relaxivity (relaxation enhancement effect of the complex in solution regarding to 1 mM concentration), high thermodynamic stability, high inertness, good solubility, low osmolality and so on. Obviously, high relaxivity is a key parameter, since with higher relaxivity, less complex needs to be administered to achieve the same contrast enhancement. Furthermore, the suitable thermodynamic stability and high inertness collectively determine the lower toxicity of the CAs by preventing the *in vivo* dissociation of the applied chelates, the liberation of the paramagnetic metal ion. The free Gd^{3+} ion is toxic, its LD_{50} value is around 0.1-0.3 mmol/kg, so that has to be enclosed by ligands.

In order to prevent the liberation of the Gd^{3+} in the body, that is complexed with polyamino-polycarboxylate chelators bearing high stability and inertness. Upon the release of the Gd^{3+}, it can interact with the small bioligands (carbonate, phosphate, amino acids, etc.), proteins, enzymes and interfere with biological processes (signaling paths). Since the ionic size of Gd^{3+}, 0.99 Å, is close to that of Ca^{2+}, the Ca^{2+} can be replaced by Gd^{3+} in essential molecules.[7] Furthermore, the Gd^{3+} ion can accumulate in different tissues and organs.[8]

Initially, the risk of GBCAs was considered negligible, but in 2006, the illness known as nephrogenic systemic fibrosis (NSF) was recognized as a debilitating and fatal disease and linked to the *in vivo* dissociation of Gd^{3+} chelates. In September 2010, the US Food and Drug Administration (FDA) ordered screening for those who have acute

kidney harm or severe renal disease. Finally, they classified the clinically approved GBCAs as Group I agents for linear (gadodiamide, gadopentetate dimeglumine, gadoversetamide) and Group II agents for macrocyclic (gadobenate dimeglumine, gadobutrol, gadoteric acid, gadoteridol). Later, the FDA and the European Medicines Agency (EMA) decided to partially suspend the linear GBCAs gadodiamide, gadopentetic acid, and gadoversetamide.[9]

The discovery of NSF induced a still growing research to replace the compromised agents with safer alternatives. A solution to this problem is to prevent the decomplexation of GBCAs by increasing their inertness through developing more rigid chelates.[10–12] On the other hand, the desired goal of reducing the risk of serious intoxication can be achieved by applying essential paramagnetic metal ions, such as Mn(II) or Fe(III), to development biocompatible CAs.[10,13,14]

II. Literature review

II.1. Chemistry of lanthanides and Gd-based Contrast agents

The lanthanides (Ln) are a series of 15 metallic elements starting from lanthanum (Z=57) to lutetium (Z=71) (Figure 1).

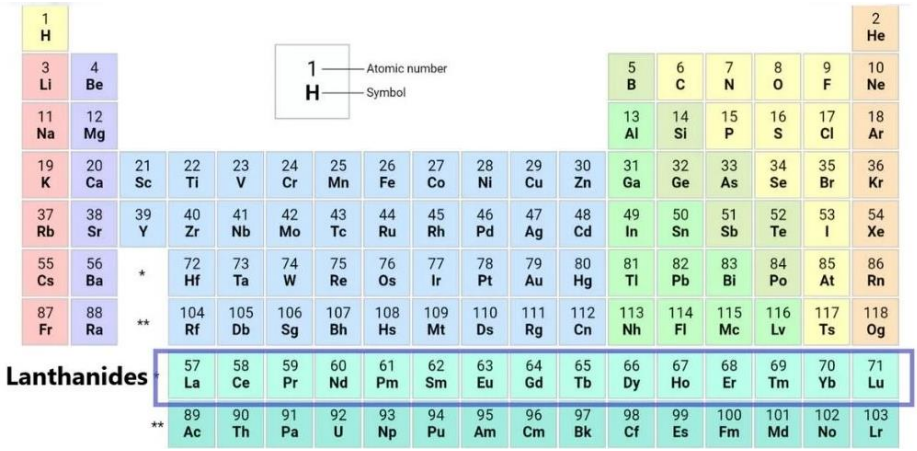

Figure 1. The periodic table

In the lanthanide series the electron configuration changes from $[Xe]4f^0$ to $[Xe]4f^{14}$. The 4f electrons of the lanthanides are shielded from the surrounding of the ions by the $5s^2$ $5p^6$ $5d^1$ $6s^2$ electrons, but, at the same time, the latter ones are not shielded from the increasing nuclear charge due to the overlap between the subshells, the poor shielding coefficient of the f electrons. This behavior results in the so-called lanthanide contraction, the decrease of the atomic and ionic size along the series. This phenomenon causes the monotonous change in the physico-chemical properties of the Lns. Because of the electron configuration $[Xe]4f^{0\text{-}14}5d^16s^2$ their oxidation state in compound is mostly +3. In the Ln^{3+}-aqua complexes the most common coordination numbers (CN) are 8 and 9, which decreases with the decreasing of the

ionic radius. The trivalent Ln ions have hard character, so those prefer the coordination of hard donor atoms, such as O and F. Ln^{3+} ions are paramagnetic (except La^{3+} and Lu^{3+}) owing to the unpaired F electrons. Their paramagnetism is independent of the coordination environment and they have sharp line-like electronic spectra. The f-f transitions are forbidden resulting long excited lifetimes and low extinction coefficient.[15,16]

The ground state electron configuration of gadolinium is $[Xe]4f^75d^16s^2$. The presence of seven unpaired electrons in Gd^{3+} gives it the most paramagnetic nature. The paramagnetic behavior of Gd^{3+} interacts with the magnetic nature of water protons, shortening their relaxation times.[17]

The linear GBCA named gadolinium diethylenetriamine pentaacetic acid $[Gd(DTPA)(H_2O)]^{2-}$ was the first contrast agent on the market accepted in 1988,[18,19] which was followed by the $[Gd(DOTA)]^-$.[20] GBCAs approved by the FDA are linear and macrocyclic chelates composed of polyamino-polycarboxylate ligands (PP) containing O and N donors for the coordination. The first CAs were negatively charged, so their i.v. injection sometimes caused pain for the patients. For this reason, neutral CAs were also developed and marketed, such as [Gd(DTPA-BMA)], [Gd(DTPA-BMEA)], [Gd(HP-DO3A)] and [Gd(DO3A-B)]. The most CAs applied in the daily routine excrete through the kidneys due to their hydrophilic character.[21] The hydrophilic CAs are not suitable for the investigation of the blood vessels, brain or liver, therefore CAs bearing lipophilic moieties were developed. The *in vivo* lifetime of these CAs is longer and their excretion occurs mainly through the liver.

Table 1. Clinically used contrast agents

Short name	Generic name	Trade name	Properties
Gd-DTPA	Gadopentate dimeglumine	Magnevist	ionic-linear
Gd-DOTA	Gadoterate meglumine	Dotarem, Artirem	ionic-macrocyclic
Gd-DTPA-BMA	Gadodiamide injection	Omniscan	nonionic-linear
Gd-HP-DO3A	Gadoteridol injection	ProHance	nonionic-macrocylic
Gd-DTPA-BMEA	Gadoversetamide	OptiMARK	nonionic-linear
Gd-DO3A-butrol	Gadobutrol	Gadovist	nonionic-macrocyclic
Gd-BOPTA	Gadobenate dimeglumine	MultiHance	ionic-linear
MS-325[a]	Gadofosveset	AngioMARK, Vasovist, Ablavar	ionic-linear/BPCAs
Gd-EOB-DTPA[b]	Gadoxetate	Primovist, Eovist	ionic-linear/liver
–	Gadopiclenol	Elucirem	nonionic-macrocyclic

[a] MS-325 is blood poor contrast agent (BPCAs), [b] Gd-EOB-DTPA is liver targeted contrast agent[22]

Macrocyclic GBCAs are more stable and inert compare to linear ones. So, those are more resistant against the *in vivo* dissociation triggered by the endogenous metal ions, such as Zn^{2+} or Cu^{2+}, and the bioligands.[1]

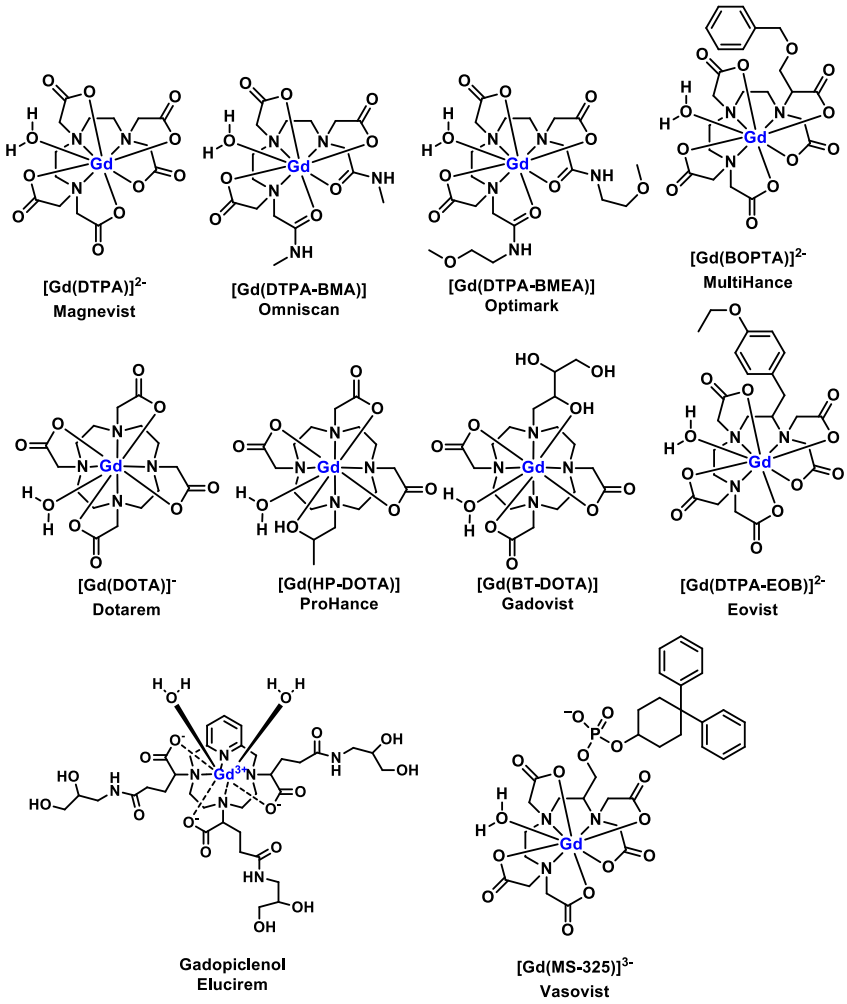

Figure 2. Clinically used contrast agents (CAs) based on Gd(III) complexes.[4]

II.2. Chemistry of manganese and Mn-based Contrast agents

The drawback of GBCAs in clinical applications is related to the toxicity of the free Gd^{3+} ion. Currently, researchers are attempting to synthesize manganese-based CAs as an effective alternative to Gd^{3+} ones. The Mn^{2+} ion possesses five unpaired electrons in 3d orbitals contributing to its paramagnetic nature, furthermore it possesses slow electronic relaxation and relatively fast water exchange, which not limits

the relaxivity of its complexes in contrast with that of Gd^{3+}. The coordination number of the Mn^{2+} usually 6 or 7. Manganese is an essential metal ion, existing mostly in Mn^{2+} form in the living systems utilized for mitochondrial and cellular activities. The ability of Mn^{2+} to be transported in nerve cells makes it preferable for neuroimaging purposes. Its ^{52}Mn isotope exhibits positron emission in its decay, which can be utilized for positron emission tomography (PET) imaging, which provides opportunity for designing Mn-based contrast agents for combined PET/MR imaging.[23] The normal concentration of manganese in serum is around 0.5-1.2 μg/dL. Its function is to stimulate some enzymes, for example manganese superoxide dismutase,[24] regulation of vitamins and sugar in the blood, and enlargement of the immune and nervous system functions (circa 80% of the manganese is in the brain).[25]

The liver controls the storage, redistribution, and elimination of Mn as it spreads throughout the body. When Mn levels are excessive, it can also be removed through the kidneys. Similarly to the Gd^{3+}, the Mn^{2+} has similar ionic radius to Ca^{2+} and it can replace the Ca^{2+} in many biological processes. The Mn^{2+} exhibits a strong affinity to proteins[19] and nucleic acids,[26] furthermore it can step across the Blood-Brain Barrier, which means in high concentration the Mn^{2+} is neurotoxic resulting in the so-called manganism (similar to Parkinson's disease).[27] In the recent decades a specific field called MEMRI (manganese-enhanced magnetic resonance imaging) has emerged using free Mn^{2+} to visualize brain function. The main disadvantage of this technique is the toxicity of the free Mn^{2+} which is almost the same as that of the Gd^{3+}.[28] Thus, the Mn^{2+} ion has to be also encapsulated in the form of complexes for the safe applications. However, Mn^{2+} ions have zero ligand-field

stabilization energy (ZFSE, d^5 configuration), which makes its complexes less stable and labile compared to those of Gd^{3+} ion. Additionally, there is a probability of oxidation from Mn^{2+} to Mn^{3+}, which can decrease its paramagnetic nature due to the loss of one unpaired electron.[29]

Since, the Mn^{2+} forms complexes with lower thermodynamic stability (due to the lack of the ZFSE) than other transition metals, the inertness of the potential Mn-based CAs became the most important parameter in the *in vivo* stability. In general, the linear Mn^{2+} complexes, even those have suitable stability for biological application, possess very low inertness.[30] However, in the recent years, several macrocyclic contrast agents delivering excellent features for MRI applications, have been developed and proposed for human imaging.[31–35]

Liposome-encapsulated $MnCl_2$ salt (LumenHance®) was the first Mn-based MRI CA used in an oral formulation for gastrointestinal imaging. However, the aforementioned neurodegenerative disorder, the manganism was observed due to an overdose of Mn^{2+} ions. Now, this CA is no longer commercialized.[36]

The second Mn-based CA used in the clinic practice was the $[Mn(DPDP)]^{6-}$ (mangafodipir) known as Teslascan™ from the GE Healthcare approved by the FDA in 1997. Mangafodipir was applicable specifically for the liver in the hepatobiliary system.[37] The inertness of the $[Mn(DPDP)]^{6-}$ is very low, its contrast enhancement effect was originated from its fast dissociation in the liver, the liberation of the Mn^{2+} ion. This CA is also not available anymore due to the low demand for this type of investigations.

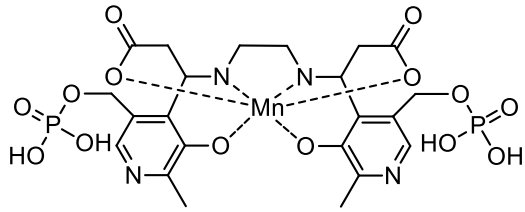

Figure 3. $[Mn(DPDP)]^{6-}$, Teslascan

In the recent years, several chelators have been synthetized for Mn^{2+} complexation and their complexes proposed for MRI applications, but none of those could break the monopoly of GBCAs, so far.[38] Beside the cyclen-based ligands,[13,35,39] the most extensively studied ligands are the pyclen and bispyclen derivatives, where the incorporation of pyridine ring(s) increases significantly the rigidity of the complexes, positively influencing the inertness of those.[32,40]

II.3. Stability of the complexes in solution

II.3.1. Thermodynamic stability

Thermodynamic stability refers to the equilibrium constant (stability constant, K_{ML}) of the formation reaction, when thermal equilibrium is attained. Assuming that the ligand is not protonated, the thermodynamic stability constant can be expressed by equation (1). The standard concentration, $c^0 = 1$ M, was omitted from the equations for simplicity.

$$K_{ML} = \frac{[ML]}{[M][L]} \quad (1)$$

, where [ML], [M], and [L] are the equilibrium concentrations of the complex, the metal ion and deprotonated ligand, respectively (the

charges are not assigned for simplicity). Since the ligands usually have protonable donor atoms and the complex formation is competitive reaction between the protons and the metal ion, the determination of the protonation constants (pK_as) is also important. The protonation constant of the ligand can be expressed as:

$$K_i^H = \frac{[H_iL]}{[H_{i-1}][H^+]} \quad (2)$$

, where i = 1, 2, . . . , n, and $[H^+]$, $[H_{i-1}L]$, and $[H_iL]$ are the equilibrium concentrations of H^+, $H_{i-1}L$, and H_iL species, respectively.

Furthermore, the complex itself can be protonated in lower pH range, which can be described by the following equation:

$$K_{MH_iL} = \frac{[M(H_iL)]}{[M(H_{i-1}L)][H^+]} \quad (3)$$

, where i = 1, 2, . . . , n, and $[H^+]$, $[M(H_{i-1}L)]$, and $[M(H_iL)]$ are the equilibrium concentrations of H^+, $M(H_{i-1}L)$, and $M(H_iL)$ species, respectively.

Additionally, the water molecule coordinated in the inner sphere of the complex can deprotonate or OH^- ion can bound to the metal center. These processes can be described by the following equations:

$$K_{M(OH)L} = \frac{[ML]}{[M(OH)L][H^+]} \quad (4)$$

$$K_{MLOH} = \frac{[ML(OH)]}{[ML][OH^-]} \quad (5)$$

Due to the competition occurs between the metal ions and protons for the donor atoms of the ligand, the conditional stability of a complex at a given pH can be expressed by the conditional stability constants, $K^{C}_{M(L)}$:

$$K^{C}_{ML} = \frac{[ML]}{[M][L]_t} = \frac{[ML]}{[M][L]\alpha_H} \quad (6)$$

, where $[L]_t = [L] + [HL] + [H_2L] + \ldots + [H_nL]$; $\alpha_H = 1 + K_1[H^+] + K_1K_2[H^+]^2 + K_1K_2K_3[H^+]^3 + \ldots + K_1K_2 \ldots K_n [H^+]^n$ and so $K^{C}_{ML} = K_{ML}/\alpha_H$.

In short, if we are in possession of the protonation and stability constants as well as the concentration of the components, any conditional stability constant and the equilibrium concentrations can be calculated. The concentration of the free metal ion ($[M^{z+}]$) in equilibrium can be used as an indicator for the stability of the complex in the given circumstance. The so-called pM value can be gained by calculating the $-\log[M^{z+}]$, which is a preferable way of comparison of stabilities.[41]

The overall basicity ($\sum pKa$) of ligands is the sum of the protonation constants of each donor atom of the ligand. Usually, higher basicity results higher stability constants during the calculation, however the direct comparison of the $\log K_{ML}$ values can be misleading. For Gd^{3+} complexes, when one carboxylate group of DOTA is replaced by alcohol donating group, the stability decreases due to the lower basicity of nitrogen atoms (the lack of H-bond between the carboxylic O and macrocyclic N donors) and weaker donor ability of the alcohol

group.[42] For example, the stability of $[Gd(DOTA)]^-$ was found to be 2-4 orders of magnitude higher than that of [Gd(HP-DO3A)] and [Gd(BT-DO3A)].[43] In order to reach high stability, the chelate ring forming with the participation of the metal ion and the donor atoms (N–Gd–N and N–Gd–O) should be at least five-membered to decrease the steric strain. The coordination cavity should be of optimum size for the metal ion and should be preorganized.[44]

II.3.2. Kinetic stability

The high thermodynamic stability of a complex do not ensure its resistance against dissociation in a highly complex system such as human blood.[45] The presence of endogenous metal ions and bioligands in the blood gives real opportunity for exchange reactions, which leads to the liberation of the paramagnetic metal ion. A 2009 data analysis of FDA showed that the NSF occurrence of different GBCAs is inversely related to inertness of the contrast agent.[46] This observation led to that the inertness of the applied chelates is more important than their thermodynamic stability. The main pathways to potential dissociation in biological conditions are:

(i) Acid-catalyzed dechelation of the complex (this is the main dissociation pathway for macrocylic complexes).[47]

$$GdL \rightarrow Gd^{3+} + L$$

(ii) Transmetallation of the chelate by endogenous metal ions, especially Cu^{2+} and Zn^{2+}.[48]

$$GdL + [M]^{2+} \rightarrow Gd^{3+} + [ML]^{-}$$

(iii) Dissociation of Gd^{3+} chelate induced by endogenous ligands (A) like citrate, phosphate or bicarbonate, which is also important for non-macrocyclic contrast agents.

$$GdL + A \rightarrow GdA + L$$

The same dissociation pathways are operative in the case of Mn^{2+} chelates as well.

The role of ligand-ligand exchange is negligible for macrocyclic CAs because it has been found no formation of ternary compounds (GdLA).[49] In other study, the presence of endogenous ligand made the rate of dissociation of [Gd(DTPA-BMA)] to be one or two orders of magnitude higher than that of $[Gd(DTPA)]^{2-}$. This can be reasoned by the formation and faster dissociation of ternary complexes of low stability.[50]

Generally speaking the dissociation of macrocyclic complexes is slower than the open-chain ones but some examples have been provided for non-linear complexes with poor kinetic inertness.[51] The lower basicity ($\Sigma \log K_i^H$) of a ligand can help to increase the inertness of its complex just like in the case of DOTA-tetraamide ligands. The lower capacity of the DOTA-tetraamide to bind H^+ ion decreases the competition occurs between H^+ and M^{z+} for the donor atoms.[52] Rigidity of the ligand is a key role parameter to reach high inertness. Ln^{3+} complexes of DCTA are kinetically more stable than Ln^{3+} complexes of EDTA, which can be explained by rigidity of DCTA complex due to the presence of cyclohexane ring. The free rotation of the ethylene backbone of the EDTA is hindered by the cyclohexane ring.[53] Although, the ligand CyPic3A is heptadentate, so its Gd^{3+} complex contains two inner sphere water molecule, it was found to be kinetically inert and as good as to the clinically approved octadentate ligands.[54] The Gd^{3+} complex of the

[Gd(HYD)] was found to be 25-fold times inert than the commercial available $[Gd(DTPA)]^{2-}$.[55] The $[Ln(cb\text{-}tedpa)]^{+}$, a rigid, cross-bridged cyclam derivative possesses exceptionally high kinetic inertness, higher than that was determined for the "gold-standard" $[Ln(DOTA)]^{-}$ complex.[56] The report on the Gd^{3+} complex of the open-chain ligand $cddadpa^{4-}$, exhibiting exceptional kinetic inertness comparable to macrocyclic ligands, serves as evidence that the rigidification of open-chain ligands plays a significant role in increasing kinetic inertness.[10] Speaking of Mn^{2+} complexes, some open-chain ligands can also form kinetically inert complex with Mn^{2+}, containing rigid backbone like DCTA.[30] Furthermore, several macrocyclic ligands have been synthetized for Mn^{2+} complexation in recent years, own very high inertness.[34,57,58]

II.4. Relaxivity

Longitudinal (spin-lattice) relaxation time. The time it takes for M_z (the magnetization along the z-axis) of nucleus to return to its equilibrium state after the pulse has been applied, is called the spin-lattice relaxation time, or T_1. This process determines how energy is transferred from the spinning nuclei to the surrounding molecules (called "lattice").

There are three criteria for T_1 energy transfer:

1. The nuclei must gain or lose energy, creating a fluctuating magnetic field.
2. This fluctuating magnetic field must match the Larmor frequency, v_0.
3. Only the x and y components of the local magnetic field can cause T_1 relaxation.

The rate of this process is influenced by temperature because molecular motion depends on it. At equilibrium, the total magnetization (M_0) aligns with the applied magnetic field (B_0).

The equation describing how magnetization returns to equilibrium during this process is the following:

$$M_Z=M_0\left(1\text{-}e^{-\tau/T_1}\right) \quad (7)$$

, where, M_z, M_0 and τ are the longitudinal magnetization, the total magnetization at full recovery and the delay time following the 90^0 RF pulse, respectively.

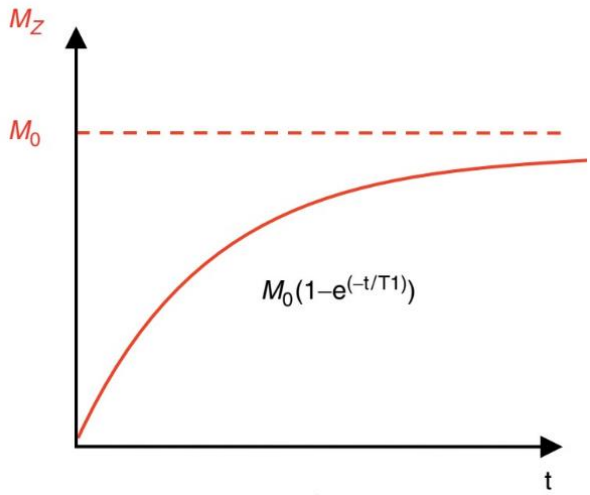

Figure 4. Longitudinal (T_1) relaxtion[2]

Positive contrast agents are those that shorten T_1 (the longitudinal relaxation time of the tissue), increasing the intensity of T_1-weighted MR images. T_1 shortening agents are MRI contrast agents based on Gd^{3+} or Mn^{2+} compounds.[4,59]

Transverse (spin-spin) relaxation time. T_2 refers to how fast the nuclear spins lose their alignment (get out of phase with one another) in the x,y-plane after a 90° pulse. Initially, the spins all move in the same direction, but over time, they gradually lose their coherence because of non-uniform magnetic field and/or interactions between the spins. This process takes place without energy transfer to the surrounding molecules (the lattice). However, T_2 depends on T_1 relaxation because any increase in magnetization along the z-axis (T_1) causes a decrease in magnetization in the x,y-plane back to zero at equilibrium. Interestingly, the T_2 relaxation time is always shorter than T_1. T_2 relaxation time determines the rate of disappearance of the transverse magnetization (M_{xy}) created by a pulse.

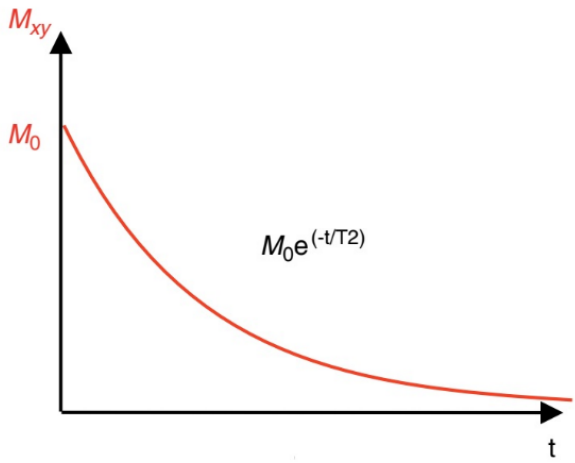

Figure 5. Transverse (T_2) relaxation[2]

A negative contrast agent in MRI is a substance that reduces signal intensity by shortening the transverse relaxation time (T_2) of water molecules, making the image appear darker.

T_2-weighted MRI is less commonly used compared to T_1-weighted MRI. Among others, iron oxide and gadolinium-based nanoparticles can be used to create T_2-weighted images.[60]

The relaxation mechanisms of protons in the presence of paramagnetic center were described by Solomon, Bloembergen and others.[61] The observed relaxation rate of solvent protons, $1/T_{i,obs}$, is the sum of both the diamagnetic term $1/T_{i,d}$ and paramagnetic term $1/T_{i,p}$.

$$\frac{1}{T_{i,obs}} = \frac{1}{T_{i,d}} + \frac{1}{T_{i,p}} \qquad i=1,2 \tag{8}$$

The relaxation rate is directly proportional to the concentration of paramagnetic metal:

$$\frac{1}{T_{i,obs}} = \frac{1}{T_{i,d}} + r_i[Gd] \qquad i=1,2 \tag{9}$$

The source of proton relaxation is from the interaction of dipole-dipole proton nuclear spin and the magnetic field caused by parallel electron spin of paramagnetic agent. The total paramagnetic relaxation arise from an inner spheres water molecule coordinated to M^{z+} ion and outer sphere water molecules which are found in second coordination sphere. The outer sphere influence is the result of electron spin metal interaction with bulk water molecules that diffuse around the paramagnetic agent.

The overall paramagnetic relaxation rate enhancement due to the paramagnetic substance is given as in Eq. (10), or expressed in relaxivities as in Eq. (11):

$$\left(\frac{1}{T_{i,p}}\right) = \left(\frac{1}{T_{i,p}}\right)^{IS} + \left(\frac{1}{T_{i,p}}\right)^{OS} \quad (10)$$

$$r_i = r_i^{IS} + r_i^{OS} \quad (11)$$

, where IS and OS stand for the inner and outer sphere, respectively.

The following equation (12) shows the paramagnetic relaxation is directly proportional to water exchange at M^{z+} center and inversely proportional to water residence time τ_m.[62,63]

$$\left(\frac{1}{T_1}\right) = \frac{cq}{55.5}\left[\frac{1}{(T_{1m}+\tau_m)}\right] = P_m q\left[\frac{1}{(T_{1m}+\tau_m)}\right] \quad (12)$$

, where $1/T_1$ is the longitudinal relaxation rate, c is molar concentration, q is the number of water molecules directly coordinated to M^{z+}, and P_m is the mole fraction of water coordinated to the metal center.

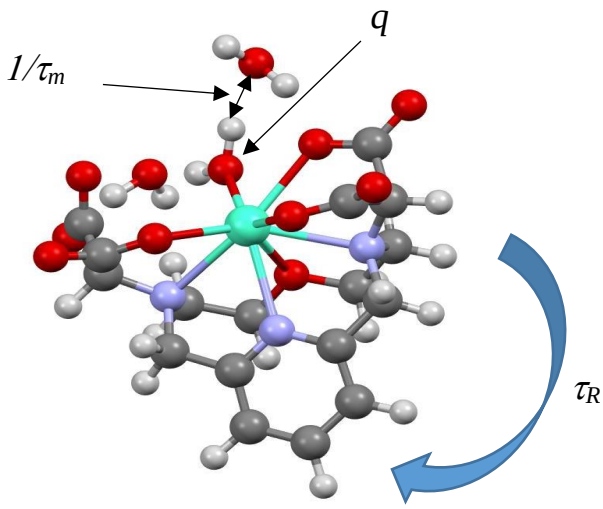

Figure 6. Factors affect the relaxivity of paramagnetic metal ion complexes.

Based on Solomon-Bloembergen-Morgan theory the factors that must be optimized in designing the ligands to increase relaxivity are (Figure 6):

1. Hydration number of the complex (q): Based on the aforementioned reasons, as the q increases, the inner-sphere relaxivity also increases. Unfortunately, the number of q is inversely proportional to the thermodynamic stability and inertness of the chelates, since to increase the coordination sites for water molecules, the number of the ligand donor atoms must be reduced. Chemists are conducting intensive studies to design MRI contrast agents based on two-water-coordination systems. For example, HOPO based complexes with 2 inner sphere water molecules was developed by Raymond and his colleagues.[1,64,65] The following Gd(III) complexes are systems are coordinated with two water molecules in inner sphere with promising thermodynamic stability and kinetic inertness.
2. Residence time of the coordinated water molecule (τ_m): It is the inverse of the water exchange rate between the inner sphere and the bulk ($k_{ex}=1/\tau_m$). Water molecules directly coordinated to M^{z+} are the main contribution to T_1 rate improvement. When the bound water exchanges fast, the effect can spread quickly to the bulk water. However, if the exchange is too fast, the water molecule coordinated to the metal center does not have enough time for complete relaxation. The water exchange rate should be optimized to successfully transmit the paramagnetic nature to the solution.[66] Generally, an increase in water exchange rises when the bond between the metal ion and oxygen of water molecule (M^{z+}-O_w) is weakened by any of the factors.

Studies have been done to improve the water residence time by replacing the donor groups of common polyaminocarboxylate ligands with amide and hydroxyl functional groups.[1] The $[Gd(DOTA)]^-$ complex with four carboxylate groups has a mean residence time of 244 ns, while tetramethylamide analog (DOTMA) with four amide groups exhibits a much longer mean residence time (19 μs). The Gd^{3+} in DOTA complex has a lower positive charge density that leads to a higher water exchange rate by weakening the bond between the Gd^{3+} and the O_W lone pair.[67]

Steric compression around the water-coordinating site can also facilitate the water exchange rate. For example, τ_m = 3.7 ns was found for the $[Gd(TRITA)(H_2O)]^-$ when an ethylene bridge in the DOTA ligand was substituted by a propylene moiety. Even though a small decrease in stability was observed, still that would be acceptable for MRI investigations.[68–70]

The stereochemistry of cyclen-based ligands affects the water exchange rate, as well. The second way of increasing steric compression is by regulating the isomeric distribution of the chelate. The two diastereomeric conformations of cyclen-based chelates are square antiprismatic (SAP) and twisted square antiprismatic (TSAP). The twist angle between chelating oxygen and chelating nitrogen atoms of SAP and TSAP are ~40° and ~25°, respectively. The lower twist angle in TSAP isomer provides more sterically crowded surroundings around the water coordinating site to increase water exchange rate.[71]

3. Rotational correlation time (τ_R): the best way of optimizing τ_R is increasing the size of the MRI contrast agent. Since, large molecules

tumble more slowly than smaller ones, their relaxivities are increasing significantly, which goal can be achieved by *in vivo* interaction with large molecules like human serum albumin (HSA) or self-assembled as well as multimeric structure.[72]

4. Electron spin relaxation rates ($1/T_{1,2e}$): Electron relaxation time influences both inner and outer sphere mechanism, even though it provides an effective contribution to relaxivity at low fields, which are not applicable in clinical practice. At this time research is being conducted as an option for high-field scanners using Mn^{2+}-based CAs at variable field. For example, the application of fast-field cycling MRI using Mn^{2+}-liposomes offers considerable improvement in sensitivity and specificity.[73–75]

III. The objectives of this research

As previously mentioned, kinetic inertness has become of critical importance compared to thermodynamic stability for MRI contrast agents intended for practical use. The increase in the inertness of the complexes can be achieved by increasing the rigidity of the macrocyclic ring, for example, by incorporating the donor atoms into rigid structures (amine → pyridine), or in order to avoid the fast dechelation, the highly basic donor atoms can be replaced with less basic ones (amine → etheric oxygen). However, these modifications also come with disadvantages, as they cause the loss of the substitutability of the given atom(s), resulting in a drop in the denticity of the ligand. Nevertheless, the proper denticity can be achieved by incorporating side chain(s) which contains more than one donors. Based on previous results, we knew that the O-pyclen macrocycle has a rigid structure, so it seemed to be a good platform for designing ligands suitable for the coordination of both Gd(III) and Mn(II) ions using malonate pendants. Furthermore, since the coordination number of the Mn(II) ion is lower (its complexes typically exhibit a coordination number (CN) of 7) than that of the Gd(III) (CN = 9), the H_2OPMMA with its 6 donor atoms appeared to be suitable for Mn(II) complexation, while the H_2OPDMA (8 donors) for the chelation of Gd(III). Thus, in both cases, there is also possibility for a water molecule to be coordinated in the inner sphere of the complexes.

For these reasons, the objectives of this research were:

(i) To synthesize O-pyclen-based macrocyclic ligands bearing malonate pendant arms for Gd^{3+} and Mn^{2+} complexation as potential MRI agents.

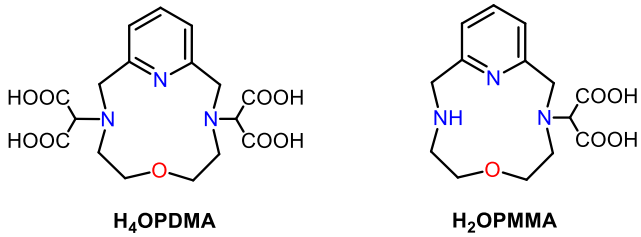

H_4OPDMA **H_2OPMMA**

Figure 7. Structure of the investigated ligands.

(ii) To characterize the relaxation properties of the complexes to understand the relations between the structure of the chelates and the parameters influencing their relaxivities.

(iii) To investigate the thermodynamic stability and inertness of the complexes, the two factors, which are essential for the safe *in vivo* applications.

IV. Materials and Methods

The commercial reagents/solvents purchased from Sigma-Aldrich (St. Louis, MO, USA) and Fluorochem Ltd. (Hadfield, United Kingdom) were used without further purification. The metal salts and other materials used in the studies were purchased from commercial sources and used without further purification (the purity of the compounds was higher than metal salts is 99.0%). Standardized Na_2H_2EDTA was used to determine the concentration of the metal ion solutions using complexometric titrations in the presence of different indicators (Ln^{3+} - xylenol orange, Cu^{2+} - murexide). The complexes were prepared by mixing known concentrated solutions of the components in 1:1 stoichiometric ratio, followed by pH adjustment. Deionized Milli-Q water was used for the preparation of all aqueous solutions (equilibrium/kinetic/relaxometric studies).

IV.1. HPLC measurement

A Waters Alliance 2690 HPLC unit equipped with Waters 996 PDA detector, and a Phenomenex Luna C18(2) 100Å 150 x 4.6 mm 5 micron column were used to follow the synthetic reactions. This system was also used to confirm the formation of the complexes and to investigate the stability of the solutions. The separation and purification of the ligands were carried out with a YL9100 HPLC system (Korea) equipped YL9101S degasser, YL9110S pump, YL9120S UV/VIS detector, Phenomenex Luna Prep C18(2) 100Å 250 × 21.2 mm 5 micron 00G-4252-P0-AX column and Sigma-Aldrich CHROMASOLV® Plus solvents.

Table 2. Applied gradient flow of analytical HPLC (Column: Luna C18(2) 150 mm×4.6 mm, 100 Å, 3 μm) for the purity control of OPMMA diethyl ester and OPDMA tetraethyl ester ligands.

	Solvent A (5 mM TFA solution)	**Solvent B** (MeCN)
0.0 min	95%	5%
15.0 min	5%	95%
16.0 min	95%	5%

Table 3. Applied gradient flow of analytical HPLC (Column: Luna C18(2) 150 mm× 4.6 mm, 100 Å, 3 μm) for the purity control of H_2OPMMA and H_4OPDMA ligands.

	Solvent A (H_2O)	**Solvent B** (MeCN)
0.0 min	100%	0%
15.0 min	40%	60%
16.0 min	100%	0%

Table 4. Applied gradient flow of analytical HPLC (Column: Luna C18(2) 150 mm× 4.6 mm, 100 Å, 3 μm) for the purity control of [Cu(OPMMA)] and [Mn(OPMMA)] complexes.

	Solvent A (H_2O)	**Solvent B** (MeCN)
0.0 min	100%	0%
15.0 min	40%	60%
16.0 min	100%	0%

Table 5. Applied gradient flow of analytical HPLC (Column: Luna C18(2) 150 mm×4.6 mm, 100 Å, 3 μm) for the purity control of $[Gd(OPDMA)]^-$ and $[Eu(OPDMA)]^-$ complexes.

	Solvent A (H_2O)	**Solvent B** (MeCN)
0.0 min	100%	0%
15.0 min	40%	60%
16.0 min	100%	0%

IV.2. Mass spectrometry measurement

Mass spectra were recorded in the Laboratory of Instrumental Analysis, Department of Inorganic and Analytical Chemistry, University of Debrecen by using a maXis II UHR ESI-QTOF MS Bruker instrument. The purity of the final products were higher than 98.0% determined by reverse-phase HPLC with UV−Vis detection at 220 and 260 nm.

IV.3. pH potentiometric studies

The pH potentiometry is most common technique for describing the equilibrium of the metal ion complexes. The H^+ concentration of a solution containing ligand and metal ion is influenced by the basicity of the ligand and the interaction between the protonated ligand species and the metal ion. As it was mentioned before, the knowledge of the protonation constants of the ligands is necessary for the calculation of the stability constants.

Unfortunately, not all equilibrium systems can be studied by pH potentiometry. Direct titrations can be performed only when the equilibration is fast, which is generally happens in the case of open-

chain metal ion complexes, since their formation rate is high even in acidic conditions. On the contrary, for example, the formation of Ln-based macrocyclic chelates frequently takes days or weeks when the so-called batch (out-of-cell) technique can be used. The batch method needs at least 8-10 samples prepared in the desired pH range with known metal, ligand and H^+ concentrations. The pH of the samples (sometimes other parameters as well) is measured after reaching the equilibrium and analyzed.

Another disadvantage of pH potentiometry, is the accuracy of the measured pH. The working pH range of pH potentiometry is around 1.5 – 12.5, since below pH 1.5 the acid error, while above pH 12.5 the alkaline error affect the measured pH values. Therefore, to describe the electrode answer for the change in the H^+ concentration, the difference between the measured and calculated pH values are always determined with the method proposed by Irving.[76] From these strong acid – strong base titrations the ion product of water (K_w) can also be evaluated. If the equilibrium is out of the range of pH potentiometry, then other techniques such as NMR or spectrophotometry are frequently used to describe the system.

Protonation constant of the ligands (H_4OPDMA and H_2OPMMA) and the protonation and stability constants of their metal ion complex were determined using pH-potentiometric titrations supported by relaxometric measurements in the case of the $[Gd(OPDMA)]^-$. The analytical concentration of the ligand stock solutions was calculated from the ligand titrations. A Metrohm 888 Titrando workstation equipped with a Metrohm-6.0233.100 combined electrode were used for the pH-potentiometric titrations. KH-phthalate (pH=4.005) and borax

(pH=9.177) buffers were applied for the the electrode calibration. The samples were kept under N_2 atmosphere during the titrations to avoid the effect of CO_2. The 6.0 mL samples were at 25 °C and stirred. 0.15 M NaCl was used to keep the ionic strength constant. The titrations were performed by using 0.2 M NaOH (dwell time = 40 s). The concentration of the ligand and the metal ions were in the range of 1.5 - 2.0 mM in 1 to 1 ratio. 130-200 volume–pH data pairs were recorded in the titrations in the pH range of 1.7-12.0. The Irving factor of the electrode and the K_w were evaluated from acid-base titration in which 0.01 M HCl was used.[76] PSEQUAD program was used to gain the equilibrium constants.[77] Since the formation of the $[Gd(OPDMA)]^-$ occurs under pH 2, 11 out-of-cell samples were prepared in the acid concentration range 0.001-0.08 M (I=$[Na^+]$+$[H^+]$=0.15 M) and their T_1 and T_2 relaxation times were measured after equilibration time (2 hours). In order to avoid the misleading information may be originated from the slow complex formation in acidic condition, the pre-prepared $[Gd(OPDMA)]^-$ complex was mixed with HCl solution. To determine the relaxation times, Bruker Minispec MQ-60 NMR Analyzer was used (more details below).

IV.4. UV-Vis spectrophotometry

Since, the absorption spectra of the metal ions and ligands containing chromophores change upon complexation the UV-Vis spectrophotometry can be used for kinetic and structural investigation of metal ion complexes. In our case, spectrophotometry was applied to describe the dissociation kinetics of the $[Gd(OPDMA)]^-$ and [Mn(OPMMA)] complexes.

The rate of the transmetallation occurs between the $[Gd(OPDMA)]^-$ complex and Cu(II) ions was studied at 37 °C in the presence of 0.15 M NaCl by monitoring the absorbance change at 260 nm using a Cary 100 Bio UV-vis spectrophotometer (pH range 2.0 – 4.0). The concentration of the complex was 0.1 mM, while that of the Cu(II) ion was 10-, 20- and 40-times higher to ensure pseudo-first order conditions. The pH was maintained by means of chloroacetic acid (pK_a=2.9) and 1,4-dimethylpiperazine (pK_a=4.2) buffers in 50 mM concentration.

Based on preliminary experiments, the dissociation rate of the [Mn(OPMMA)] was found to be fast for conventional spectrophotometry, therefore stopped-flow technique was used to investigate the reaction occurs between the complex and the Cu(II) ion. The concentration of the complex and the Cu(II) 0.1 and 2.0 mM, respectively. The reactions were carried out at 25 °C, in the presence of 0.15 M NaCl by an Applied Photophysics DX-17MV stopped-flow machine. The decomplexation was followed at 280 nm in the pH range 3.9–5.0 For pH stabilization, N-methylpiperazine (NMP, log K_2^H = 4.90) was used in 20 mM concentration, as a buffer.

The k_{obs} (pseudo-first-order rate constant) values were evaluated by fitting the absorbance-time data pairs to the Equation (13)

$$A_t = (A_0 - A_e)e^{-k_{obs}t} + A_e \qquad (13)$$

, where A_t, A_0 and A_e are the absorbance at time t, at the start and at equilibrium of the reactions, respectively. The Micromath Scientist computer program (version 2.0, Salt Lake City, UT, USA) was used to

fit the time-absorbance data pairs by using a standard least-squares procedure.

IV.5. ^{1}H-relaxometry

The number of the water molecules coordinated to the free paramagnetic metal ion or in the inner sphere of a paramagnetic complex has a significant influence on the relaxivity of a system. It means that the ^{1}H relaxometry can be effectively used to study the formation and dissociation reactions of the Gd^{3+} and Mn^{2+} complexes. Generally speaking, every process, which modify the q can be followed by this technique.

For this reason, the dissociation reaction of the $[Gd(OPDMA)]^-$ (1.0 mM) in the presence of Eu(III) ion (20 mM) at 37 °C and 0.15 M NaCl ionic strength was studied by measuring the $1/T_2$ relaxation rates of the samples on a Bruker Minispec MQ-60 NMR Analyzer (pH range 2.0 – 4.0). The $1/T_2$ values of the samples were determined with the Carl–Purcell–Meiboom–Gill (CPMG) spin-echo pulse sequence.[78] The pH was maintained by means of chloroacetic acid (pK_a=2.9) and 1,4-dimethylpiperazine (pK_a=4.2) buffers in 50 mM concentration. The experimental data were analyzed by the Scientist program calculating the k_{obs} values according to equation (13) (using the measured relaxation rates instead of absorbances).

The ^{1}H longitudinal (T_1) for $[Gd(OPDMA)]^-$ and [Mn(OPMMA)] as well as the transverse (T_2) relaxation times for [Mn(OPMMA)] complex were determined by using Bruker Minispec MQ-20 and MQ-60 NMR analyzers. The temperature was set to 25 or 37 (±0.2) °C, and maintained with a circulating water bath thermostat. For T_1 determination, inversion recovery method (180°–τ–90°; 6–8 data points

at 10 different τ delay times) was used, while the T_2 relaxation times were determined by the aforementioned CPMG method in the presence of HEPES buffer (50 mM, pH = 7.4) and 0.15 M NaCl.

IV.6. NMR measurements

The NMR spectra were recorded on Bruker Avance II 500 MHz spectrometer (Bruker, Billerica, MA, USA) using deuterated solvents (chemical shifts are given as δ values with reference to the deuterated solvents (D_2O, CD_3CN) and the coupling constants are reported in Hz).

IV.7. ^{1}H NMRD and ^{17}O NMR studies

In order to determine the parameters govern the relaxivity of the paramagnetic metal complexes ^{1}H NMRD and ^{17}O NMR measurements were carried out. The nuclear magnetic relaxation dispersion (NMRD) profiles can deliver information about the interaction mechanisms and dynamic processes affecting the relaxivity. In NMRD experiments the r_{1p} values are measured in the function of the ^{1}H Larmor frequencies. Since several parameters influence the relaxivity, some of those have to be determined independently by different techniques such as variable temperature ^{17}O NMR, which delivers information about the water exchange rate (k_{ex}^{298}), rotational-correlational time (τ_R), the hyperfine coupling constant ($A/\hbar$) and q by measuring the differences between the chemical shifts ($\Delta\omega_r$) of the bulk and bound water molecules, the T_1 and T_2 relaxation times of the ^{17}O nucleus. In addition, given the large number of parameters, some of those need to be fixed based on reasonable estimates, literature evidences during the calculations. In order to get reliable access to these parameters the simultaneous fitting of the data obtained by different methods is advised.

The equations used for the fitting of ^{17}O NMR and ^{1}H NMRD data are the followings:

^{17}O NMR data have been fitted according to the Swift-Connick equations,[62,63] the Solomon−Bloembergen−Morgan theory of paramagnetic relaxation[79,80] for the description of the inner-sphere water ^{1}H and ^{17}O relaxation and the Freed model for the outer-sphere contribution to relaxivity.[81]

The reduced transverse ^{17}O relaxation rates, $1/T_{2r}$, and reduced ^{17}O chemical shifts, ω_r, are calculated from the measured relaxation rates and angular frequencies of the paramagnetic solution ($1/T_2$, ω) and of the diamagnetic reference ($1/T_{2A}$ and ω_A), equations (14) and (15):

$$\frac{1}{T_{2r}} = \frac{1}{P_m}\left[\frac{1}{T_2} - \frac{1}{T_{2A}}\right] = \frac{1}{\tau_m}\frac{T_{2m}^{-2} + \tau_m^{-1}T_{2m}^{-1} + \Delta\omega_m^2}{(\tau_m^{-1} + T_{2m}^{-1})^2 + \Delta\omega_m^2} \qquad (14)$$

$$\Delta\omega_r = \frac{1}{P_m}(\omega - \omega_A) = \frac{\Delta\omega_m}{(1 + \tau_m T_{2m}^{-1})^2 + \tau_m^2\Delta\omega_m^2} \qquad (15)$$

, where T_{2m} is the transverse relaxation time of ^{17}O, $\Delta\omega_m$ is determined by the hyperfine or scalar coupling constant, $A_O/\hbar$, where B represents the magnetic field, S is the electron spin and g_L is the isotropic Landé g factor (16).

$$\Delta\omega_m = \frac{g_L \mu_B}{3k_B T}(S(S+1)B \times \frac{A}{\hbar} \qquad (16)$$

The scalar contribution, $1/T_{2sc}$, can be given by equation (17).

$$\frac{1}{T_{2m}} \cong \frac{1}{T_{2sc}} = \frac{S(S+1)}{3}\left(\frac{A}{\hbar}\right)^2 \times (\tau_{s1} + \frac{\tau_{s2}}{1+\tau_{s2}^2\,\omega_s^2}) \qquad \frac{1}{\tau_{si}} = \frac{1}{\tau_m} + \frac{1}{T_{ie}} \qquad (17)$$

, where τ_{si} is the correlation time characteristic for scalar (contact) mechanism, T_{ie} (T_{1e} and T_{2e}) is the longitudinal or transverse electron spin relaxation times of the metal ion, thus τ_{s1} and τ_{s2} describe the correlation time of the longitudinal and transverse relaxations, respectively.

The temperature dependence of the exchange rate (k_{ex}; or inverse binding time, τ_m) of the inner sphere water molecule can be described by the Eyring equation (18):

$$\frac{1}{\tau_m} = k_{ex} = \frac{k_B T}{h}\exp\left\{\frac{\Delta S^{\ddagger}}{R} - \frac{\Delta H^{\ddagger}}{RT}\right\} = \frac{k_{ex}^{298} T}{298.15}\exp\left\{\frac{\Delta H^{\ddagger}}{R}\left(\frac{1}{298.15} - \frac{1}{T}\right)\right\} \qquad (18)$$

, where $\Delta S^{\ddagger}$ and $\Delta H^{\ddagger}$ are the activation entropy and enthalpy, k_{ex}^{298} is the exchange rate at 298.15 K.

The electronic relaxation is mainly governed by modulation of the transient zero-field splitting. Furthermore, McLachlan has developed equations (19-21)[82] for describing the electron spin relaxation rates, $1/T_{1e}$ and $1/T_{2e}$.

$$\left(\frac{1}{T_{1e}}\right) = \frac{32}{25}\Delta^2\left(\frac{\tau_v}{1+\omega_S^2\tau_v^2} + \frac{4\tau_v}{1+4\omega_S^2\tau_v^2}\right) \qquad (19)$$

$$\left(\frac{1}{T_{2e}}\right) = \frac{32}{50}\Delta^2\left[3\tau_v + \frac{5\tau_v}{1+\omega_S^2\tau_v^2} + \frac{2\tau_v}{1+4\omega_S^2\tau_v^2}\right] \qquad (20)$$

$$\tau_v = \tau_v^{298} \exp\left\{\frac{E_v}{R}\left(\frac{1}{T} - \frac{1}{298.15}\right)\right\} \quad (21)$$

where Δ^2 is the trace of the square of the transient zero-field-splitting (ZFS) tensor, τ_v is the correlation time for the modulation of the ZFS with the activation energy E_v, and ω_s is the Larmor frequency of the electron spin.

The proton relaxivities originate from the inner- and outer-sphere contributions and the inner-sphere term can be given by the aforementioned equations (11 and 12).

The dipolar contribution of the longitudinal relaxation rate $1/T_{1m}{}^{H}$ can be describes by equation (22):

$$\frac{1}{T_{1m}^{H}} \cong \frac{1}{T_1^{DD}} = \frac{2}{15}\left(\frac{\mu_0}{4\pi}\right)^2 \frac{\hbar^2 \gamma_S^2 \gamma_I^2}{r_{MH}^6} S(S+1)\left[\frac{3\tau_{d1H}}{1+\omega_I^2 \tau_{d1H}^2} + \frac{7\tau_{d2H}}{1+\omega_S^2 \tau_{d2H}^2}\right] \quad (22)$$

, where $T_1{}^{DD}$ is the relaxation time of ^{1}H governed by the dipol-dipol mechanism, r_{MH} is the effective distance between the metal ion electron spin and the water protons, ω_I is the proton resonance frequency, τ_{diH} (τ_{diH} is the correlation time characteristic for dipol-dipol mechanism, τ_{d1H} and τ_{d2H} describe the correlation time of the longitudinal and transverse relaxations) is given by equation (23):

$$\frac{1}{\tau_{diH}} = \frac{1}{\tau_m} + \frac{1}{\tau_{RH}} + \frac{1}{T_{ie}} \qquad i = 1, 2; \quad (23)$$

, where τ_{RH} is the rotational correlation time of the metal ion–H_{water} vector.

The outer-sphere contribution to the overall relaxivity is described by equation (24), where N_A is the Avogadro constant, and J_{os} is a spectral density function (25).

$$r_1^{os} = \frac{32N_A\pi}{405}\left(\frac{\mu_0}{4\pi}\right)\frac{\hbar^2\gamma_S^2\gamma_I^2}{\alpha_{GdH}D_{GdH}}S(S+1)[3J_{os}(\omega_I,T_{1e})+7J_{os}(\omega_S,T_{2e})] \quad (24)$$

$$J_{os}(\omega,T_{je}) = Re\left[\frac{1+{}^1/_4\left(i\omega\tau_{MH}+\frac{\tau_{MH}}{T_{je}}\right)^{1/2}}{1+\left(i\omega\tau_{MH}+\frac{\tau_{MH}}{T_{je}}\right)^{1/2}+{}^4/_9\left(i\omega\tau_{MH}+\frac{\tau_{MH}}{T_{je}}\right)+{}^1/_9\left(i\omega\tau_{MH}+\frac{\tau_{MH}}{T_{je}}\right)^{3/2}}\right] \; j = 1, 2 \quad (25)$$

, where α_{GdH} is the closest distance of the water proton nuclear spin (I) and the gadolinium electron spin (S), D_{GdH} is the diffusion coefficient for relative diffusion of the spins, $D_{GdH} = D_I + D_S$.

The temperature dependence of the diffusion coefficient for the diffusion of a water proton away from a complex, D_{MH}, described by equation (26), with its activation energy E_{MH}:

$$D_{MH} = D_{MH}^{298}\exp\left\{\frac{E_{MH}}{R}\left(\frac{1}{298.15}-\frac{1}{T}\right)\right\} \quad (26)$$

It is obvious based on the equations that ^1H relaxivity is governed by several parameters. In one limiting case, when $T_{1m} << \tau_m$, the exchange rate will be the determining factor for relaxivity (Equation 12). In reverse case, when $\tau_m << T_{1m}$, the relaxivity will be determined by the relaxation rate of the coordinated protons (T_{1m}), which depends on the rate of proton exchange, rotation and electronic relaxation. Furthermore, variables such as Gd–proton distance (r_{GdH}) and the hydration number (q) also influence the relaxivity. It is easy to understand that two inner-sphere water molecules instead of one, will double the inner-sphere

relaxivity (Equation 12), or a longer distance between the metal center and the H atom results in a significant decrease in that because of its sixth-power dependence (Equation 22). However, it is harder to assume the influence of τ_R, the proton exchange rate or T_{1e}, which becomes more complicated by knowing the fact that these parameters strongly depends on the magnetic field.

A relaxivity maximum can be attained when the inverse of the correlation time, $1/\tau_{d1}$, equals the proton Larmor frequency (Equation 23). However, τ_m appears also in Equation 12, which indicates a higher r_1 for shorter τ_m value. Therefore, τ_m should be decreased but not so much that it starts to limit T_{1m}. So, τ_R and the proton exchange rate have to be optimized at the same time in order to gain maximum r_1 values, which values of the prameters are, of course, dependent on the magnetic field.

^{1}H NMRD measurements were performed on samples containing the [Gd(OPDMA)]$^-$ (pH = 7.4) and [Mn(OPMMA)] (pH = 8.0) in 1.0 mM concentration (in the case of [Mn(OPMMA)] 10% ligand excess was applied) at 25 and 37 °C, on a Stelar SMARTracer Fast Field Cycling relaxometer (0.01−10 MHz) and a Stelar high field relaxometer (10-128 MHz). The temperature was maintained by a VTC91 temperature control unit and gas flow, and it was calibrated by a Pt resistance probe.

The transverse ($1/T_2$) relaxation rates and chemical shifts of an aqueous solution of the complexes (the concentration and the pH were set to 21.4 mM and 7.0 for the [Gd(OPDMA)]$^-$ as well as 6.4 mM and 8.0 for the [Mn(OPMMA)], respectively) and of a diamagnetic reference ($HClO_4$ acidified water, pH = 3.3) were measured in the

temperature range 273–348 K using a Bruker Avance 400 (9.4 T, 54.2 MHz) spectrometer. The temperature was determined according to the method proposed by Raiford.[83] The $1/T_2$ values were determined by CPMG technique.[78] In order to avoid the susceptibility corrections to the chemical shifts, a glass sphere in an 10 mm NMR tube was applied. ^{17}O enriched water (10% $H_2{}^{17}O$, CortecNet) was added to the solutions to reach around 1% enrichment. The least-squares fit of the ^{17}O NMR and NMRD data was performed by means of Visualiseur/Optimiseur[84] running on a MATLAB 8.3.0 (R2014a) platform.

IV.8. Determination of *q* for [Gd(OPDMA)]$^-$

In order to determine the number of the water molecules in the inner sphere of the [Gd(OPDMA)]$^-$ luminescence lifetimes of the [Eu(OPDMA)]$^-$ complex were measured on an Agilent Cary Eclipse Fluorescence spectrophotometer. The decay of the emission intensity at 614 nm followed by an excitation at 268 nm was recorded. Measurements were performed in both H_2O and D_2O solutions. The settings were as follows: gate time: 0.1 ms (1 ms in D_2O); delay time: 0.1 ms; flash count: 1; total decay time: 5 ms (15 ms in D_2O); 10 cycles; PMT detector: 650 mV. At least three decay curves were collected for each sample, and all lifetimes were analyzed as monoexponential decay. The reported lifetimes are an average of at least three measurements . The number of q, 1.2[85]/1.3[86] was found to be the same at pH = 3 and pH = 7.

IV.9. DFT calculations

The ground state geometry of the $[Gd(OPDMA)]^{-}$ was computed using the Gaussian 09 software package[87] (ES64L-G09 RevE.01) at the DFT level of theory. In this calculation, the TPSSh exchange-correlation functional[88,89] in combination with Grimme's DFT-D3 approach including BJ-damping[90] was used together with the quasi-relativistic effective core potential including 53 electrons in the core (ECP53MWB) with the corresponding (7s6p5d)/[5s4p3d] basis sets for Gd.[91,92] All other atoms were treated with the 6-311G(d,p) basis set. The effect of the solvent was taken into account by using the polarizable continuum model (PCM).[93] Single-point frequency calculations at the same level of theory were also carried out for the ground state geometry, which represented a true energy minimum (0 imaginary frequencies) on the potential energy surface.

Geometry optimization of the [Mn(OPMMA)] complex was computed by using Gaussian 09[87] (EM64L-G09RevC.01) at DFT level of theory using the hybrid-meta-GGA TPSSh[89] functional combined with the aug-cc-pVTZ-J for Mn(II) which is described by a (25s17p10d3f2g)/[17s10p7d3f2g] contraction scheme.[94] The *def2*-TZVP basis set was used for non-metal atoms (H, C, N and O). All calculations accounted for solvent effect using the continuum model (PCM) for water.[95] Single-point frequency calculations were carried out with the same functional and basis sets for the ground state geometries which represented true minima on the potential energy surface.

Single-point calculation for the optimized geometry was carried out to predict the ^{17}O hyperfine coupling constant. This calculation was computed through the ORCA[96] package using the TPSSh functional. In

this calculation, the aug-cc-pVTZ-J basis set was used for Mn(II) and the other atoms were treated by the EPR-III basis sets of Barone[97] which triple-ζ basis set includes diffuse functions, double d-polarizations and a single set of f-polarization functions. The resolution of identity and chain of spheres exchange (RIJCOSX) approximation[98,99] was used to accelerate the calculations and tight SCF convergence criteria were employed.

V. Results

V.1. Synthesis of the ligands

The synthesis of the O-pyclen platform was first accomplished by E. Weber and F. Vögtle,[100] which method was modified by Csupász and his coworkers.[33]

Condensation reaction occurring between the tosyl-protected bis(2-aminoethyl)ether and the 2,6-bis(chloromethyl)pyridine was used to synthesis the O-pyclen macrocycle (Figure 8). The starting material bis(2-chloroethyl)ether was aminated with potassium phthalimide by using Gabriel synthesis,[101] followed by the protection of the obtained amine groups by means of tosyl chloride. The 2,6-bis(chloromethyl)pyridine was synthesized following the method suggested by H. Su and coworkers.[102] The macrocyclization step, was carried out in dry solvent (abs. MeCN) under an inert atmosphere using K_2CO_3 as a base. The deprotection of the tosyl groups was carried out in concentrated H_2SO_4 at elevated temperature (110 °C), delivered the O-pyclen macrocycle in a nearly quantitative yield.

The synthesize of H_4OPDMA ligand was performed via the alkylation of the secondary amino groups of the O-pyclen, by reacting them with various amounts of diethyl bromomalonate in anhydrous MeCN (K_2CO_3, inert atmosphere). The diethyl-bromomalonate was added in portions to the reaction mixture, and the conversion was followed by analytical HPLC technique. Since, the monosubstituted (OPMMA diethyl ester) and disubstituted (OPDMA tetraethyl ester) products have different retention times in HPLC at reverse-phase, we

were able to get information about the ratio of those. The formation of by-products was negligible.

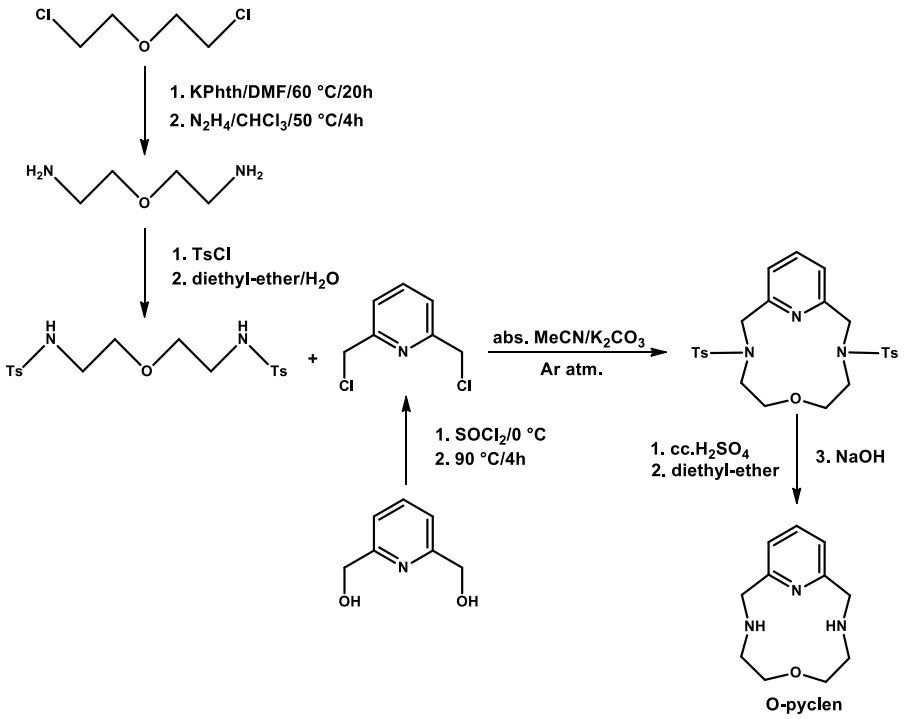

Figure 8. Synthetic route of O-pyclen macrocycle.[33]

The products were purified by preparative HPLC technique, while MS and NMR measurements were carried out to identify the compounds. The ethyl protecting groups of the macrocycle OPMMA diethyl ester and OPDMA tetraethyl ester were saponoficated using NaOH, and which was converted to its acidic form (H_2OPMMA, H_4OPDMA) during the purification procedure using the preparative HPLC technique. The ^{1}H-NMR, ^{13}C-NMR and MS spectra, as well as the analytical HPLC chromatograms of the products, can be found in the Appendix (Figures A1–A16).

Tosyl-protected O-pyclen

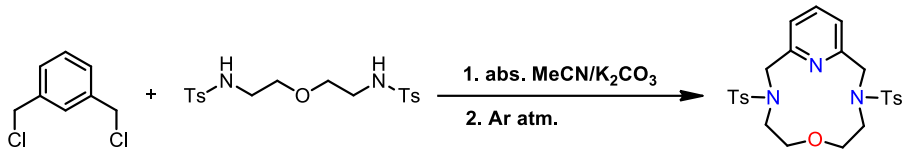

Figure 9. Condensation reaction of the tosyl-protected O-pyclen macrocycle.

The 2,6-bis(chloromethyl)pyridine (1.28 g, 7.27 mmol, 1.0 eq.) was dissolved in 25 mL dry acetonitrile and added, dropwise, to the heated reaction mixture containing the *N*,*N*-(oxydiethane-2,1-diyl)bis(4-methylbenzenesulfonamide) (3.00 g, 7.27 mmol, 1.0 eq.) in dry MeCN (10 mL) and K_2CO_3 (10.05 g, 72.7 mmol, 10 equivalent) The reaction was stirred at reflux temperature under argon atmosphere. The precipitate was filtered, after the completion of the reaction and the solvent from the filtrate was removed using reduced pressure. The residue was purified. (Flash chromatography, dichloromethane-methanol).

Yield: 2.21 g (59 %) as a white solid powder.

^{1}H-NMR (CD_3CN) δ (ppm): 7.77 (4H, t, *J* = 8.2 Hz, aromatics), 7.65 (1H, t, *J* = 7.6 Hz, aromatics), 7.42 (4H, d, *J* = 8.2 Hz, aromatics), 7.20 (2H, d, *J* = 7.6 Hz, aromatics), 4.29 (4H, s, -C*H*$_2$-), 3.51 (4H, t, *J* = 4.7 Hz, -C*H*$_2$-), 3.16 (4H, t, *J* = 4.7 Hz, -C*H*$_2$-), 2.42 (6H, s, -C*H*$_3$).

^{13}C-NMR (CD_3CN) δ (ppm): 157.1, 144.7 (2×2C, C_q, aromatics), 138.2 (1C, aromatics), 136.5 (2C, C_q, aromatics), 130.7, 128.3 (2×4C, aromatics), 123.6 (2C, aromatics), 70.5, 56.1, 50.6 (3×2C, -*C*H$_2$-), 21.5 (2C, -*C*H$_3$).

ESI-MS (m/z, positive mode): $(M+H)^+_{calc.}$: 516.1621, $(M+H)^+_{found}$: 516.1622

O-pyclen

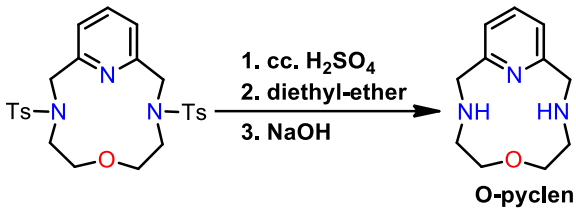

Figure 10. Deprotection of the ditosyl-O-pyclen macrocycle.

The ditosylated O-pyclen (0.50 g, 0.970 mmol, 1.0 eq.) was dissolved in 2.00 mL of cc. H_2SO_4 then the reaction was carried out in a microwave reactor (110 °C, 20 W, 5 min.). After the reaction, the mixture was cooled down first to room temperature and later it was cooled to 0 °C, by using a water–ice cooling mixture. Cold diethyl ether was added to the mixture in small portions resulting in precipitation. The solvent was decanted from the precipitate (dihydrogen sulphate salt of O-pyclen), and the residue was dissolved in 20 mL of distilled water. The pH of the solution was set to 13.2 with solid NaOH, and the product was extracted 3 times using 20 mL chloroform. The combined organic phase was dried over $MgSO_4$ and evaporated under vacuum.

Yield: 0.19 g (95%) as an orange oil.

ESI-MS (m/z, positive mode): $(M+H)^+_{calc.}$: 208.1444, $(M+H)^+_{found}$: 208.1443.

^{1}H-NMR (CD_3CN) δ (ppm): 7.57 (1H, t, *J* = 7.6 Hz, aromatics), 7.04 (2H, d, *J*= 7.6 Hz, aromatics), 3.83 (4H, s, -C*H*$_2$-), 2.96 (4H, t, *J* = 4.7 Hz, -C*H*$_2$-), 2.65 (4H, t, *J*= 4.7 Hz, -C*H*$_2$-).

^{13}C-NMR (CD_3CN) δ (ppm): 161.2 (2C, C_q, aromatics), 137.4 (1C, aromatics), 121.5 (2C, aromatics), 69.9, 54.4, 50.0 (3×2C, -CH_2-).

OPMMA diethyl ester

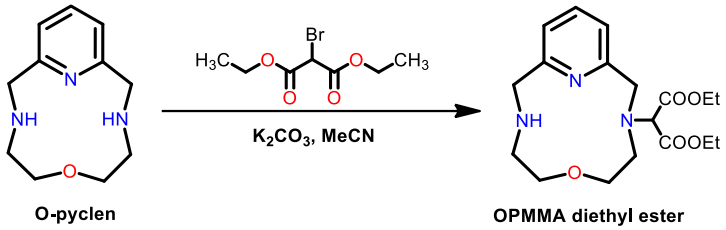

Figure 11. Alkylation reaction of O-pyclen macrocycle by diethyl bromomalonate resulting OPMMA diethyl ester.

Solid K_2CO_3 (670 mg, 4.85 mmol, 5.0 eq.) and O-pyclen macrocycle (200 mg, 0.97 mmol, 1.0 eq.) was dissolved in MeCN (5 ml). The diethyl bromomalonate (330 µl, 1,93 mmol, 2.0 eq.) was added dropwise to the basic solution under stirring. After the addition, the stirring was continued for 1 hour, while yellow precipitate formed, then the solvent was removed under reduced pressure. The product was dissolved in 2 mL of distilled water-MeCN mixture and the pH was adjusted to 5.0. The compound was purified by preparative HPLC technique. The product was a yellow powder (Figure A1-A3).

Yield: 140.0 mg, 0.38 mmol, 80%.

ESI-MS (m/z, positive mode): $[M+H]^+_{calc.}$: 366.2024; $[M+H]^+_{found}$: 366.2023.

^{1}H-NMR (500 MHz, CD_3CN) δ (ppm): 7.90 (1H, *t*, J_1=7.6 Hz, J_2=7.6 Hz, aromatic), 7.37 (2H, *t*, J_1=9.1 Hz, J_2=9.1 Hz, aromatic), 4.88 (1H, *s*, -C*H*-), 4.52 (2H, *s*, -CH_2-), 4.44 (2H, *s*, -CH_2-), 4.16 (4H, *m*, -CH_2-), 3.40 (2H, *m*, -CH_2-), 3.31 (4H, *d*, J_1=7.8 Hz, -CH_2-), 3.18 (2H, *m*, -CH_2-), 1.17 (6H, *t*, *J*=7.1 Hz, -CH_3).

^{13}C-NMR (125 MHz, CD_3CN) δ (ppm): 167.5 (2 × 1C, *C*=O), 157.3 (1 × 1C, aromatic), 151.2 (1 × 1C, aromatic), 140.6 (1 × 1C, aromatic), 122.4 (2 × 1C, aromatics), 70.8 (1 × 1C, -*C*H-), 67.7 (1 × 1C, -*C*H_2-), 66.1 (1 × 1C, -*C*H_2-), 63.0 (2 × 1C, -*C*H_2-), 58.0 (1 × 1C, -*C*H_2-), 57.7 (1 × 1C, -*C*H_2-), 50.6 (1 × 1C, -*C*H_2-), 48.1 (1 × 1C, -*C*H_2-), 14.1 (2 × 1C, -*C*H_3).

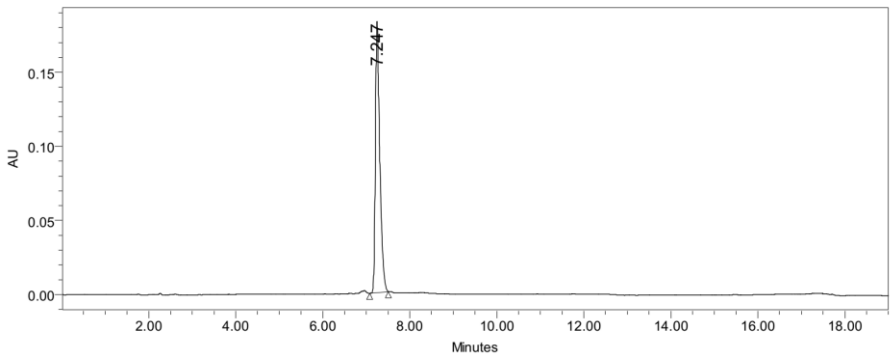

Figure 12. Analytical HPLC chromatogram of OPMMA diethyl ester. (t_R= 7.247 min).

H_2OPMMA

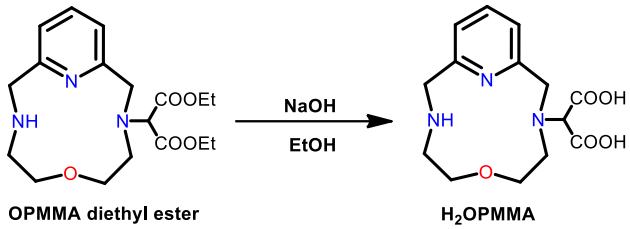

Figure 13. Deprotection of OPMMA diethyl ester.

The ethyl protecting groups were removed in alkaline condition (5 eq. NaOH). The reaction was monitored by analytical HPLC method. After the completion of the reaction the pH was adjusted to near 5.0 and the product was purified by preparative HPLC.

Final product was a yellow powder (Figure A4-A10).

Yield: 68.0 mg, 0.22 mmol, 58%.

ESI-MS (m/z, positive mode): $[M+Na]^+_{calc.}$: 332.1217; $[M+Na]^+_{found}$: 332.1216.

^{1}H-NMR (500 MHz, D_2O) δ (ppm): 7.82 (1H, *t*, J_1=7.4 Hz, J_2=7.6 Hz, aromatic), 7.32 (2H, *t*, J_1=6.6 Hz, J_2=6.9 Hz, aromatic), 4.30 (2H, *s*, -C*H*$_2$-), 4.20 (1H, *s*, -C*H*-), 4.15 (2H, *s* -C*H*$_2$-), 3.21 (2H, *s*, -C*H*$_2$-), 3.10 (4H, *s*, -C*H*$_2$-), 2.93 (2H, *s*, -C*H*$_2$-).

^{13}C-NMR (125 MHz, D_2O) δ (ppm): 174.1 (2 × 1C, C=O), 157.0 (2 × 1C, aromatics), 138.6 (1 × 1C, aromatic), 121.4 (1 × 1C, aromatic), 120.9 (1 × 1C, aromatic), 76.5 (1 × 1C, -*C*H-), 67.7 (1 × 1C, -*C*H$_2$-), 66.3 (1 × 1C, -*C*H$_2$-), 58.2 (1 × 1C, -*C*H$_2$-), 54.6 (1 × 1C, -*C*H$_2$-), 52.0 (1 × 1C, -*C*H$_2$-), 47.6 (1 × 1C, -*C*H$_2$-).

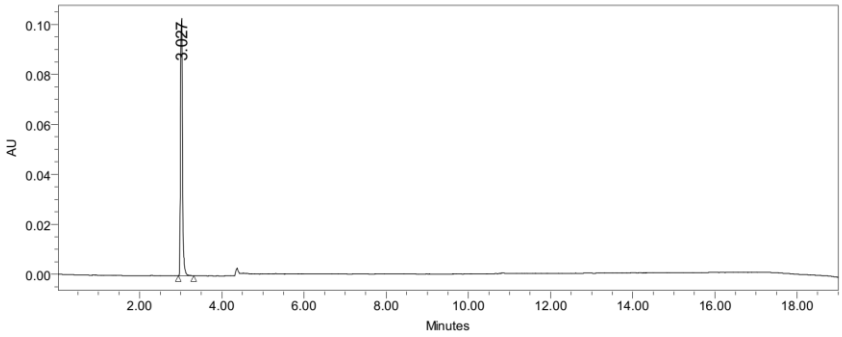

Figure 14. Analytical HPLC chromatogram of H_2OPMMA (t_R= 3.027 min).

OPDMA tetraethyl ester

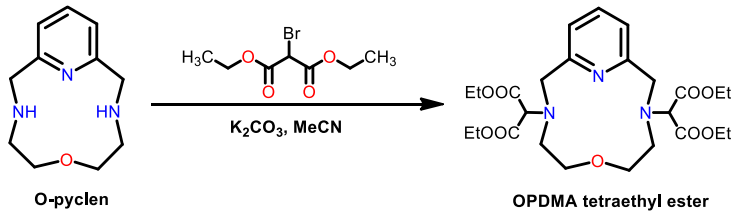

Figure 15. Alkylation reaction of O-pyclen macrocycle by diethyl bromomalonate resulting OPDMA tetraethyl ester.

Solid K_2CO_3 (670 mg, 4.85 mmol, 5.0 eq.) and O-pyclen macrocycle (200 mg, 0.97 mmol, 1.0 eq.) were dissolved in 5 ml MeCN. The diethyl bromomalonate (330 µl, 1,93 mmol, 2.0 eq.) was added dropwise to the basic solution under stirring. After the addition, the reaction mixture was stirred during one hour, while yellow precipitate appeared. After completion of the reaction, the mixture was filtered through a G3 glass filter and the solvent from the filtrate was removed under reduced pressure. The product was dissolved in 2 mL of distilled water-MeCN mixture and the pH was adjusted to 5.0. The compound was purified by preparative HPLC method. The product was a yellow powder (Figure A11-A13).

Yield: 275.0 mg, 0.52 mmol, 55%.

ESI-MS (m/z, positive mode): $[M^+H]^+_{calc.}$: 524.2603; $[M^+H]^+_{found}$: 524.2602.

^{1}H-NMR (500 MHz, CD_3CN) δ (ppm): 8.32 (1H, *t*, J_1=7.8 Hz, J_2=7.8 Hz, aromatic), 7.65 (2H, *d*, *J*=7.7 Hz, aromatics), 4.54 (4H, *m*, -CH_2-), 4.47 (2H, *m*, -C*H*-), 4.18 (8H, *t*, J_1=6.9 Hz, J_2=6.8 Hz, -CH_2-), 3.42 (4H, *m*, -CH_2-), 3.06 (4H, *m*, -CH_2-), 1.20 (12H, *t*, *J*=7.0 Hz, -CH_3).

^{13}C-NMR (125 MHz, CD_3CN) δ (ppm): 168.4 (4 × 1C, *C*=O), 155.7 (2 × 1C, aromatics), 146.3 (1 × 1C, aromatic), 123.9 (2 × 1C, aromatics), 68.8 (2 × 1C, -*C*H_2-), 68.5 (2 × 1C, -*C*H-), 62.8; 57.2; 55.1 (8 × 1C, -*C*H_2-), 14.25 (1 × 1C + 6 × 2C, -*C*H_3).

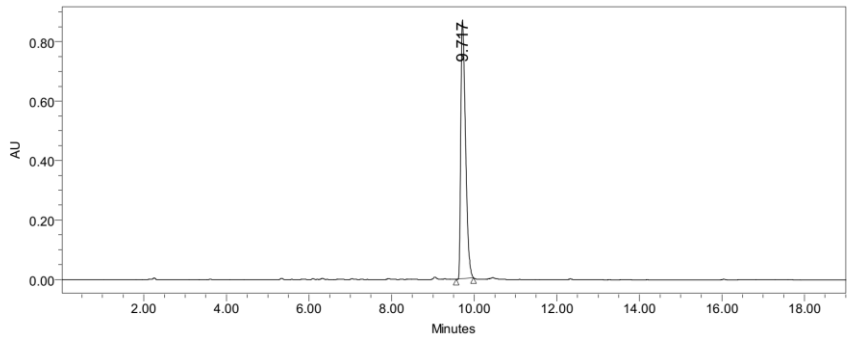

Figure 16. Analytical HPLC chromatogram of OPDMA tetraethyl ester ligand (t_R= 9.717 min).

H_4OPDMA

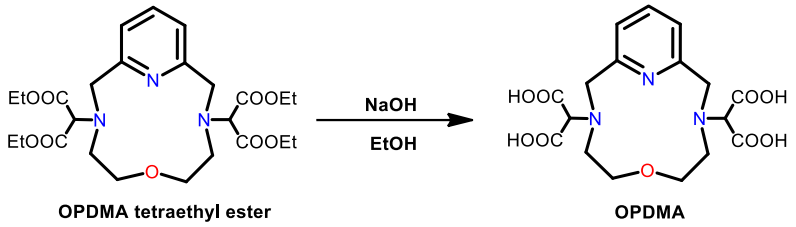

OPDMA tetraethyl ester **OPDMA**

Figure 17. Deprotection of OPDMA tetraethyl ester.

The ethyl protecting groups were removed with 5 eq. NaOH in ethanol. The reaction was monitored by analytical HPLC method. The pH of this solution was adjusted to near 4.0 and the product was purified by preparative HPLC. The product was a white powder (Figure A14-A16). Yield: 128.0 mg, 0.31 mmol, 60%.

ESI-MS (m/z, positive mode): $[M^+H]^+_{calc.}$: 412.1351; $[M^+H]^+_{found}$: 412.1350.

^{1}H-NMR (500 MHz, D_2O) δ (ppm): 7.69 (1H, *t*, J_1=7.8 Hz, J_2=7.5 Hz, aromatic), 7.20 (2H, *d*, J=7.5 Hz, aromatics), 4.17 (2H, *bs*, -C*H*$_2$-), 3.97 (2H, *bs*, -C*H*-), 3.70 (2H, *s* -C*H*$_2$-), 3.32 (2H, *bs*, -C*H*$_2$-), 2.94 (2H, *bs*, -C*H*$_2$-), 2.58 (2H, *bs*, -C*H*$_2$-), 2.29 (2H, *bs*, -C*H*$_2$-).

^{13}C-NMR (125 MHz, D_2O) δ (ppm): 177.0 (4 × 1C, *C*=O), 160.1 (2 × 1C, aromatics), 137.8 (1 × 1C, aromatic), 120.2 (2 × 1C, aromatics), 78.8 (2 × 1C, -*C*H$_2$-), 68.1 (2 × 1C, -*C*H-), 59.1 (2 × 1C, -*C*H$_2$-), 54.0 (2×1C, -*C*H$_2$-).

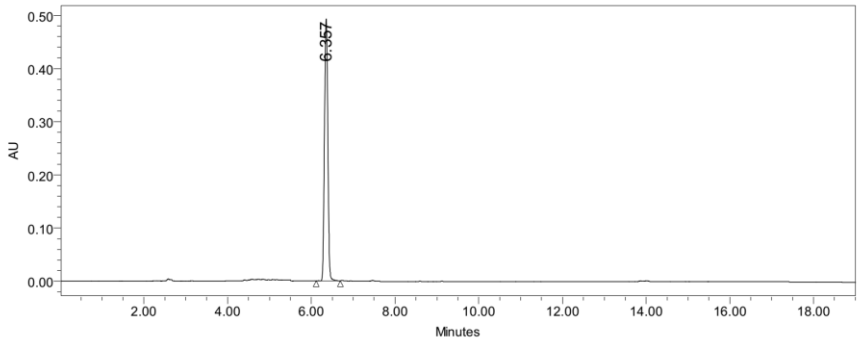

Figure 18. Analytical HPLC chromatogram of **H_4OPDMA** ligand (t_R= 6.357 min).

V.2. Physico-chemical characterization of $[Gd(OPDMA)]^-$

As it was highlighted before, the appearance of the NSF and its link to the *in vivo* decomplexation of GBCAs induced significant research efforts to improve inertness of the Gd-based complexes.[2,103,104] A possible solution to achieve this goal is to improve the rigidity of the ligands, resulted in complexes being more resistant against *in vivo* dechelation. Rigidification of the ligand backbone can be attained by incorporating rigid moieties into the structure involving the donor atoms. For example, when one or two N donor(s) in the cyclen is/are replaced by pyridine ring(s), yielding pyclen and bispyclen ligands (Figure 19), the rigidity of the macrocycle and its Gd^{3+} complex increases significantly.[105,106] However, the result of this modification is that the N donor(s) lose(s) the ability to carry a pendant arm. Less donor atoms result in a less saturated coordination sphere which is good for the relaxivity but not for the inertness.[107] On the other hand, this problem is easily remediable by introducing pendants with more than one donor atom on the substitutable nitrogens of the macrocycle. The picolinate pendant with an aromatic N and a carboxylate O is good example.[108] Another interesting option, which was barely investigated, is malonate possessing two O donors.[109–112] Another possibility to increase the inertness of the complexes is to decrease the basicity of the ligands, for example, by replacing the amine with an ether oxygen to hamper the proton-assisted dissociation.[33]

For these reasons, we combined these strategies, and designed, synthetized and investigated the coordination chemical properties of H_4OPDMA ligand and its Gd^{3+} complex. The H_4OPDMA is an

O-pyclen-based macrocyclic ligand bearing malonate pendant arms (Figure 19).

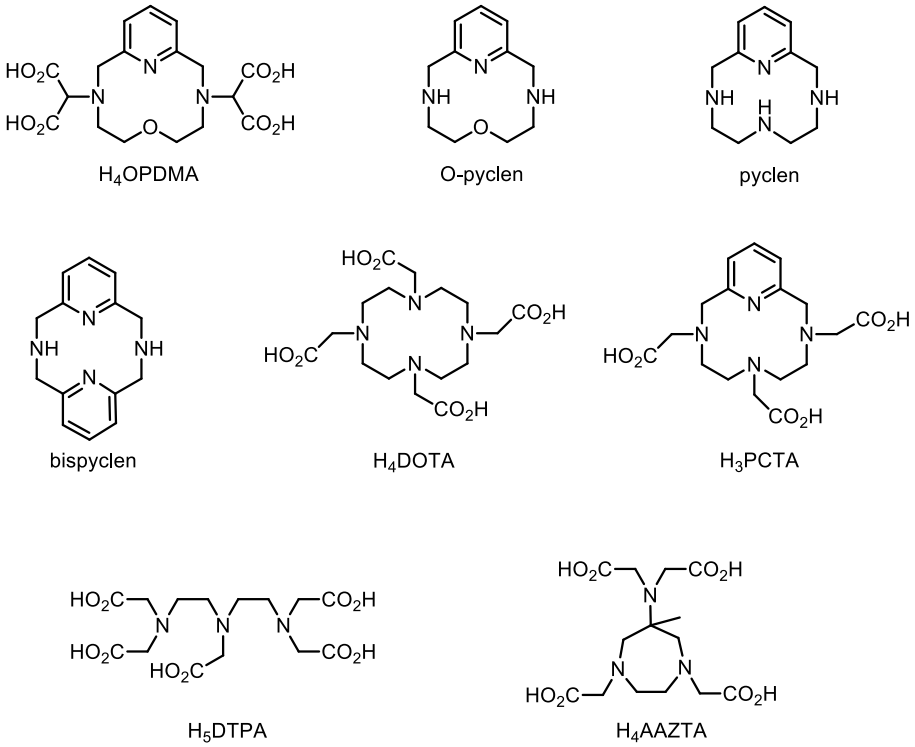

Figure 19. Structure of ligands mentioned in this chapter

V.2.1. Thermodynamic and kinetic characterization of $[Gd(OPDMA)]^-$

First, the protonation constants of the ligand and the protonation and stability constants of the Gd^{3+} complex have been determined by pH potentiometric and relaxometric methods. Five protonation constants were found for the $OPDMA^{4-}$ ligand are listed in Table 6. Since the basicity of the donor atoms located at the ligand backbone has the highest influence on the formation of the so-called “in-cage” complex, the sum of those has been calculated and compared with the

corresponding values gained for H_4DTPA,[113] H_4AAZTA,[114] H_3PCTA[115] and H_4DOTA[116] (Table 6). The results show that the basicity of H_4OPDMA is orders of magnitude lower than that of the ligands used for comparative purposes. Obviously, in OPDMA, the aromatic N donor atom has lower basicity, furthermore, another one is replaced by a less basic etheric oxygen. The decrease in the basicity has a collateral advantage, namely, the faster complex formation at acidic pH, which is typical for rigid macrocyclic ligands.[115]

Table 6. Protonation constants ($\log K_i$) of $OPDMA^{4-}$ and the comparative ligands, protonation and stability constants of their Gd^{3+} complexes (T = 25 °C).

	$OPDMA^{4-}$	**$DTPA^{5-}$ [a]**	**$AAZTA^{4-}$ [b]**	**$PCTA^{3-}$ [c]**	**$DOTA^{4-}$ [d]**
$\log K_1$	7.14(5)	9.93	11.23	11.36	11.08
$\log K_2$	6.99(2)	8.37	6.52	7.35	9.23
$\log K_3$	3.17(4)	4.18	3.78	3.83	4.24
$\log K_4$	2.23(4)	2.71	2.24	2.12	4.18
$\log K_5$	2.02(5)	2.00	1.56	1.29	1.88
$\Sigma \log K_2^H$ [e]	**14.13**	**18.30**	**17.75**	**18.71**	**20.31**
$\log K_{GdL}$	18.01(7)	22.03	20.24	20.39	24.7[f]
$\log K_{GdL}^H$	2.09(5)	1.96	1.89	–	–
pGd[g]	**14.8**	**15.5**	**13.4**	**13.1**	**16.2**

[a] Ref.[113]; [b] Ref.[114] 0.1 M KCl; [c] Ref.[115] 1 M KCl; [d] Ref.[116], $\log K_6^H$=1.71 (1.0 M NaCl); [e] $\log K_1 + \log K_2$; [f] Ref.[117] 0.1 M NaCl; [g] pH=7.4; $c_L = c_M$= 0.01 mmol/dm^3, 3σ standard deviations are indicated in parenthesis

According to literature evidence, lower ligand basicity means lower stability constants for the complexes.[2] The stability of $[Gd(OPDMA)]^-$ was studied by pH-potentiometric and relaxometric method, where the $1/T_1$ and $1/T_2$ relaxivity of the out-of-cell samples at different acid concentrations were measured. The simultaneous fitting of the experimental data obtained by the different techniques delivered the protonation and stability constants of the chelate. In order to avoid the misleading information may arise from the slow complex formation, that was tested under acidic conditions by measuring the relaxation enhancement in time. The results show that the complexation is fast at pH = 2, since there was no observable change in the relaxivity after mixing time (< 1 min). However, in order to ensure the fast equilibration at pH < 2, the out-of-cell samples were prepared by mixing the complex with an acid solution, since the complex dissociation below pH = 2 is relatively fast ($t_{1/2}$ = 9.6 min at pH = 2). The relaxivity of the samples was recorded after 2 hours of equilibration time. Previously, numerous studies[118–120] proved that the highly acidic provoke malonate decarboxylation, thus the stability of the ligand was monitored in samples containing 1.0 M HCl solution by analytical HPLC for a period of 6 hours. This measurements confirmed the ligand stability as no decarboxylation was found (Figure A17).[120,121]

The stability of the complex was found to be at least two orders of magnitude lower than those of the other complexes compared (Table 6). The conditional stabilities for the chelates were also calculated in the form of pGd for physiological pH 7.4 (c_{GdL} = 0.01 mM). The pGd of $[Gd(OPDMA)]^-$ is lower than that of $DTPA^{5-}$ and $DOTA^{4-}$ complexes, but higher than that of the $AAZTA^{4-}$ and $PCTA^{3-}$ chelates (Table 6).

The equilibrium model was validated by measuring the $1/T_1$ relaxation rates, which are presented in Figure 20 together with the species distribution curves. The r_{1p} values do not change between pH = 3 and 8 where the fully formed, deprotonated complex is present. Below pH = 3, an increase of R_{1p} can be observed by the formation of a monoprotonated complex, in which a carboxylate group is protonated results in the appearance of the q = 2 complex species.

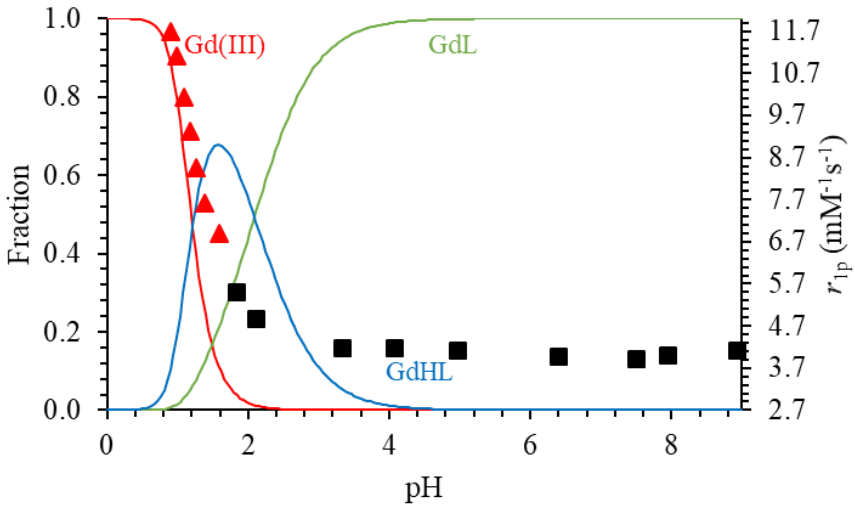

Figure 20. Species distribution curves of $[Gd(OPDMA)]^-$ system, together with the pH-dependent relaxivities (r_{1p}: ■ (direct titration) and ▲ (out-of-cell samples)) ($c_L = c_{Gd(III)}$ = 1 mM, T = 25 °C, 0.15 M NaCl, 1.41 T).

According to the DFT calculations (*see below*), one carboxylate group is not involved in the coordination. Presumably, the protonation of this carboxylate is easier at acidic pH, which leads to the decoordination of the entire malonate arm.

The kinetic inertness of Gd^{3+}-based chelates proposed for human applications as much as important than their stability to prevent the *in vivo* dechelation.[2,104] Thus, the metal exchange reactions of

[Gd(OPDMA)]$^{-}$ was studied at 37.0 °C, where Cu(II) and Eu(III) ions were applied in high excess to ensure pseudo-first order conditions (Figure 21 and 22). The exchange reactions were monitored by ^{1}H relaxometry for Eu(III) and by spectrophotometry for Cu(II) between pH = 2 and 4. The the pseudo-first order rate constant (k_{obs}) can be expressed as follows:

$$-\frac{d[Gd(OPDMA)]_t}{dt} = k_{obs}[Gd(OPDMA)]_t \quad (27)$$

, where $[Gd(OPDMA)]_t$ is the total concentration of the complex at time t.

The dissociation of macrocyclic Gd(III) complexes mainly occurs through proton-assisted pathways, since the rearrangement of the donor atoms is hampered in the heterodinuclear intermediates. As it can be seen in Figure 21, the k_{obs} values increase linearly with increasing [H^{+}], and remain independent of Cu(II) concentration, thus the process can be expressed by the following equation:

$$k_{obs} = k_0 + k_1[H^{+}] \quad (28)$$

During the fitting procedure, we found that the role of the spontaneous dissociation is negligible, so equation 28 is further simplified. The obtained rate constant and the calculated dissociation half-life ($t_{1/2}$) are given in Table 7, together with the corresponding data for the Gd^{3+} complexes of DTPA^{5-}, AAZTA^{4-}, PCTA^{3-} and DOTA^{4-}.

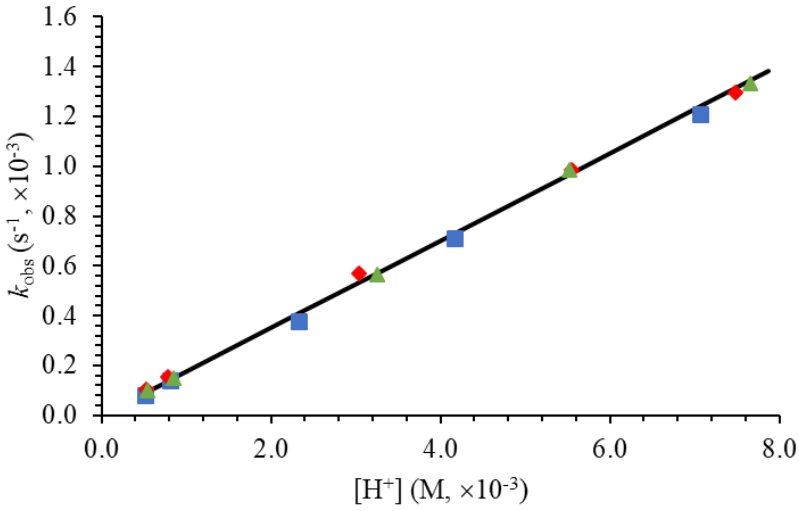

Figure 21. Dependence of the pseudo-first-order rate constants (k_{obs}) on [H$^+$] for [Gd(OPDMA)]$^-$ (Cu(II) excess: ×10■, ×20♦, ×40▲; 37 °C, 0.15 M NaCl). The line corresponds to the best fit of the k_{obs} values.

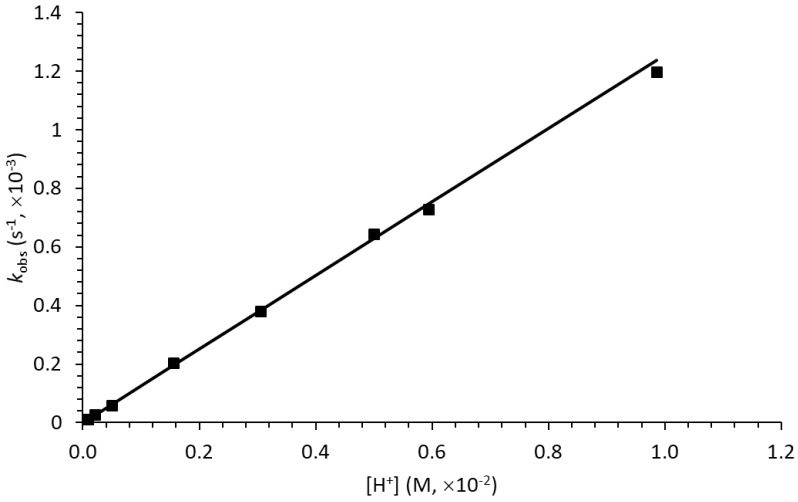

Figure 22. Dependence of the pseudo-first-order rate constants (k_{obs}) on [H$^+$] for the [Gd(OPDMA)]$^-$ complex (Eu(III) excess: ×20■, 37 °C, 0.15 M NaCl). The lines correspond to the best fit of the k_{obs} values.

Table 7. Rate constants for the dissociation reactions of $OPDMA^{4-}$, $DTPA^{5-}$, $AAZTA^{4-}$, $PCTA^{3-}$ and $DOTA^{4-}$ complexes formed with Gd(III) ion and their half-lives calculated for pH = 7.4 (25 °C / 37 °C, I =0.15 M (NaCl), charges are omitted for simplicity)

	OPDMA + Eu(III)	OPDMA + Cu(II)	DTPA[a]	AAZTA[b]	PCTA[c]	DOTA[d]
k_1 ($M^{-1}s^{-1}$)	~0.05 / 0.126(3)[e]	~0.07 / 0.175[e]	0.58	1.05	5.1×10^{-4}	8.4×10^{-6} / 2.0×10^{-5} [e]
$t_{1/2}$ (year)[f]	~11 / **4.4[e]**	~8 / **3.2[e]**	0.015	0.50	1.1×10^{3}	6.6×10^{4} / **2.7×10^{4} [e]**

[a] Ref.[48]; [b]Ref.[114]; [c] Ref.[115] refers to [Eu(PCTA)]; [d] Ref.[47]; [e] 37 °C; [f] $t_{1/2}=\ln2/k_{calc}$, pH=7.4

In order to get a better comparison of the inertness of the complexes, the k_1, characterizing the proton-assisted pathway has been estimated for 25 °C as well. Based on literature data, we assumed that the reaction rate decreases by a factor of 2.5 from 37 to 25 °C (Table 7).

Comparing the $t_{1/2}$ values, one can conclude that, the inertness of $[Gd(OPDMA)]^-$ is higher than that of the open-chain DTPA and AAZTA, but 3-4 orders of magnitude lower than that obtained for the macrocyclic PCTA and DOTA chelates. Interestingly, there is a slight (~30%) difference in the k_1 value depending on whether the exchange reactions were performed with Eu^{3+} or Cu^{2+} ions. However, we could not prove the presence of the metal-assisted pathway, the possible formation of dinuclear complexes with the exchanging metal ions may occur, which is more likely with Cu(II). The formation of the dinuclear complexes can open up the structure of the coordination cavity which can accelerate the proton-assisted dechelation.

The dissociation half-life of our complex amounts to years at 37 °C if other dissociation pathways or enzymatic processes are not operative in the body, which is sufficient for *in vivo* applications.

V.2.2. NMRD and ^{17}O NMR characterization of [Gd(OPDMA)]$^{-}$

The r_{1p} of CA candidates is a key parameter, which indicates their efficacy in relaxation enhancement. The r_{1p} values obtained for [Gd(OPDMA)]$^{-}$ at different field strengths (0.49 T and 1.41 T) and temperatures (25 and 37 °C) are compared to those of analogous chelates in Table 8.

Table 8. r_{1p} values ($mM^{-1}s^{-1}$) determined for Gd(III) complexes of $OPDMA^{4-}$ and other ligands used for comparative purposes at pH = 7.4, 25/37 °C and 20/60 MHz (charges are omitted for simplicity).

25/37 °C	OPDMA (q=1)	DTPA (q=1)	AAZTA (q=2)	PCTA (q=2)	DOTA (q=1)
0.47 T	4.5/3.7 **4.5 (HSA)**	4.7[a]/3.8[b]	7.1[d]/5.2[d]	6.9[f]/5.2[f]	4.7[a]/3.5[b]
1.4 T	4.3/3.4 **4.4 (HSA)**	4.2[c]/3.4[b]	6.7[e]/4.8[e]	6.3[g]/4.8[g]	4.3[c]/3.1[b]

[a] Ref.[122]; [b] Ref.[123]; [c] 50 MHz = 1.17 T; [d] Ref.[124], [e] Ref.[125]; [f] Ref.[126]; [g] Ref.[127]

There is no significant difference between the r_{1p} values of [Gd(OPDMA)]$^{-}$ and that of the q = 1 chelates, which indicates that one water molecule is coordinated in the inner sphere of the complex. The value of q was indeed determined by luminescence measurements on the Eu^{3+} complex (Figure A20 and A21), delivering q = 1.2±0.1 value for both pH = 7 and 3 at 25 °C.[85] The decrease of relaxivity values with increasing temperature indicates that the fast rotation of the complex limits the relaxivity, which behaviour is typical for low molecular weight Gd^{3+}-based chelates.[2] The r_{1p} values determined in the presence of human serum albumin (c_{HSA} = 0.8 mM) indicate a negligible interaction between the complex and the protein (Table 8).

The water exchange rate and the other relaxation parameters of $[Gd(OPDMA)]^-$, were studied by temperature dependent NMRD and ^{17}O NMR methods. The longitudinal relaxivities were recorded in the proton Larmor frequency range 0.04−80 MHz (9.39×10^{-4} – 1.88 T) (Figure 23). The reduced transverse ($1/T_{2r}$) relaxation rates and chemical shifts ($\Delta\omega_r$) were determined for an aqueous solution of the chelate (c_{GdL} = 21.4 mM, pH = 7) as a function of temperature (Figure 24) in the ^{17}O NMR experiments.

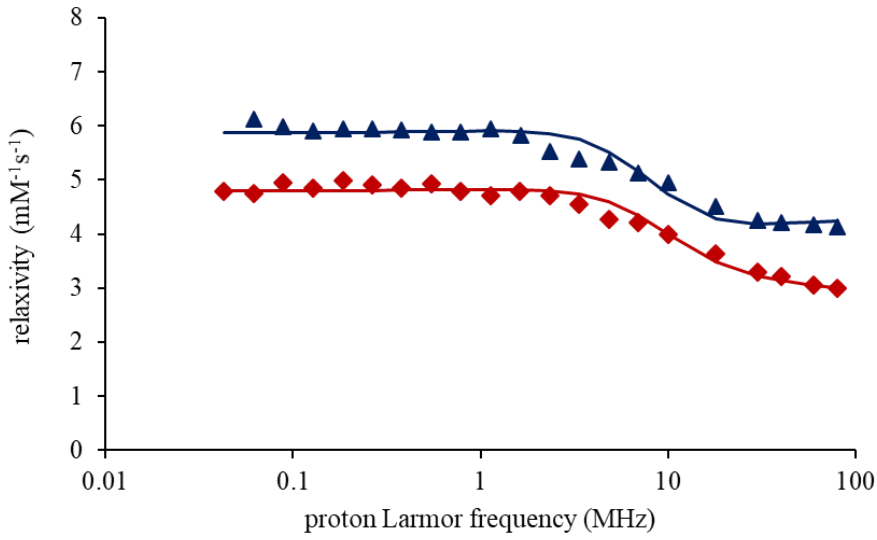

Figure 23. NMRD profiles recorded for $[Gd(OPDMA)]^-$ at 25 (▲) and 37 (♦) °C (c_{GdL} = 1.0 mM).

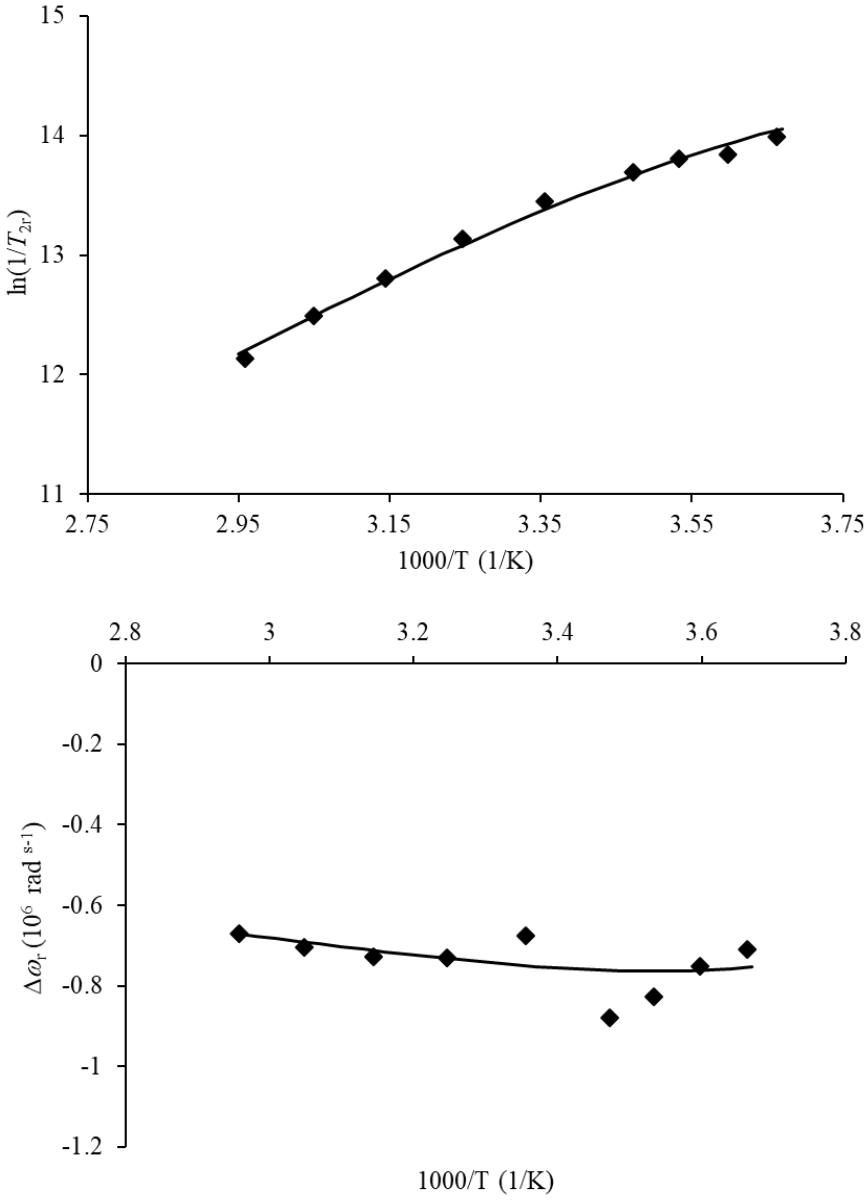

Figure 24. $1/T_{2r}$ and $\Delta\omega_r$ values determined for $[Gd(OPDMA)]^-$ (B = 9.4 T, pH = 7, c_{GdL} = 21.4 mM). The solid lines represent the best fit of the data.

The $1/T_{2r}$ values are decreasing with increasing temperature which is typical for the fast water exchange, in which $T_{2m} \gg \tau_m$. The $\Delta\omega_r$ values are also in full accordance with fast exchange, and indicate one inner sphere water molecule. The temperature dependence of $1/T_{2r}$ is determined by two factors, the transverse relaxation time of the bound H_2O (T_{2m}) and mean residence time of that in the inner sphere (τ_m) ($1/T_{2r} \sim 1/(T_{2m} + \tau_m)$).[128] The value of T_{2m} increases, while τ_m decreases with increasing temperature.

A simultaneous fitting of the ^1H NMRD and ^{17}O NMR data was carried out by using the Solomon−Bloembergen−Morgan theory of paramagnetic relaxation[79,80] for the description of the inner-sphere water ^1H and ^{17}O relaxation and the Freed model for the outer-sphere contribution to relaxivity.[81] The ^{17}O NMR data were fitted with the Swift-Connick equations.[62,63] Furthermore, some parameters were fixed during the fitting procedure, the q was fixed to 1, the distance of closest approach for the outer-sphere water molecules was set to 3.5 Å, and the distances between the Gd(III) and the H and O atoms of the coordinated H_2O were fixed to 2.5 and 3.1 Å. The diffusion coefficient, its activation energy and the activation energy for the modulation of the zero field splitting (E_v) were set to 26×10^{-10} m^2s^{-1}, 24 kJ mol^{-1} and 1 $kJmol^{-1}$, respectively. The obtained parameters are shown in Table 9.

Table 9. Best-fit parameters gained for $[Gd(OPDMA)]^-$ from the analysis of NMRD and ^{17}O NMR data along with the corresponding values found for the Gd^{3+} complexes formed with $DTPA^{5-}$, $AAZTA^{4-}$, $PCTA^{3-}$ and $DOTA^{4-}$ ligands (charges are omitted for simplicity).

Gd^{3+} chelates	OPDMA ($q = 1$)	DTPA[a] ($q = 1$)	AAZTA[b] ($q = 2$)	PCTA[c] ($q = 2$)	DOTA[a] ($q = 1$)
k_{ex}^{298} ($\times 10^6$ s^{-1})	73(12)	3.3	11.1	14	4.1
$\Delta H^{\ddagger}$ (kJ mol^{-1})	26.0(3)	52	20	45	50
$\Delta S^{\ddagger}$ (J mol^{-1} K^{-1})	-7(1)	+54	-43	+43	+47
$A/\hbar$ ($\times 10^6$ rad s^{-1})	-3.4(2)	-3.8	-3.8	-3.8	-3.7
τ_R^{298} (ps)	79(3)	58	74	70	77
E_r (kJ mol^{-1})	26(2)	17	20	–	16
τ_v^{298} (ps)	12(1)	25	30	15	11
Δ^2 ($\times 10^{20}$ s^{-2})	1.6(1)	0.46	0.26	0.59	0.16

[a] Ref.[122]; [b] Ref.[123,124]; [c] Ref.[126]

The k_{ex}^{298} of $[Gd(OPDMA)]^-$ is the highest among all complexes compared (Table 9). The negative value of $\Delta S^{\ddagger}$ (activation entropy) indicates an associative mechanism for the water exchange process, in contrast with that of $[Gd(DTPA)]^{2-}$ and $[Gd(DOTA)]^-$ chelates, where a dissociative mechanism was found. The associative mechanism is a logical consequence of the 8-coordinated metal ion, according to the

DFT calculations (see below). The lower activation enthalpy is also in accordance with this. The value of $A/\hbar$ (hyperfine coupling constant) is typical for Gd(III) complexes and in excellent agreement with that obtained by DFT calculations (-3.3×10^6 rad s^{-1}, *vide infra*). The rotational correlation time (τ_R) of our complex is close to those reported for other complexes of similar size. Interestingly, the electron spin relaxation of the $[Gd(OPDMA)]^-$ complex is relatively fast based on the higher Δ^2 (square zero field splitting energy) (Table 9). This phenomenon is likely the result of the less symmetric structure.

V.2.3. DFT calculations for $[Gd(OPDMA)]^-$

The plausible structure of the $[Gd(OPDMA)]^-$ was calculated by DFT. The structure of the $[Gd(OPDMA)]^-$ was optimized by considering an inner sphere water molecule and the presence of two second-sphere water molecules as well as the bulk solvent by using the polarized continuum model.[129,130] The optimized structure of the $[Gd(OPDMA)]^-$ is shown in Figure 25 and the Cartesian coordinates are listed in the Appendixes (Table A1).

The predicted structure shows a bicapped trigonal prismatic geometry where the ligand coordinates to the Gd^{3+} ion in a heptadentate manner. The inner sphere of the complex is completed with a H_2O molecule coordinated to the Gd^{3+} ion, yielding an overall coordination number of eight (CN=8). The Gd(III)-O_{water} distance was found to be 2.47 Å which falls into the range of first coordination shell of water. The inner sphere water molecule is stabilized by the explicit water molecules via a hydrogen bond network and the pendant malonate arms are also involved in the formation of hydrogen bonds (Table A1).

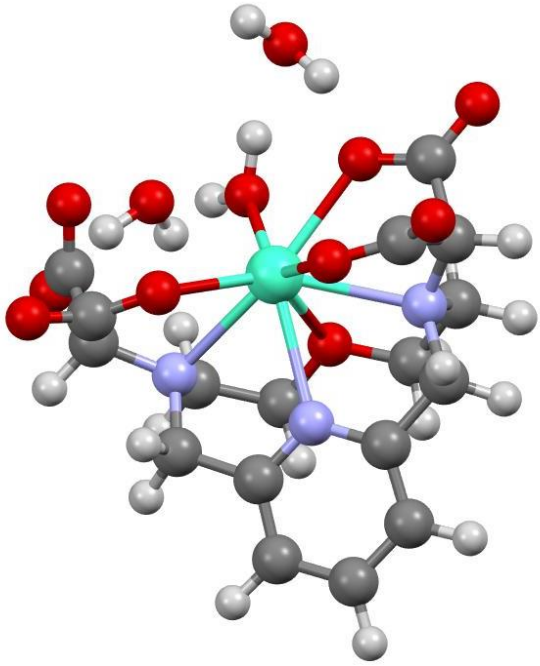

Figure 25. DFT calculated structure of $[Gd(OPDMA)]^-$ complex.

The ^{17}O hyperfine coupling constant was also calculated and estimated to be -3.33 $\times 10^6$ rad s^{-1} which is in perfect agreement with that obtained experimentally and verifies the structure in solution. Additionally, DFT also predicted a CN=9 coordination mode for the complex, where all carboxylate arms are bound to the Gd^{3+} ion completed with an inner-sphere H_2O molecule (Figure A22 and Table A2). In this case, however, the Gd(III)-O_{water} distance is calculated to be 2.61 Å which is relatively long, and the ^{17}O hyperfine coupling constant is unrealistic ($A/\hbar$ = -1.8×10^6 rad s^{-1}). Based on the results, one can conclude that the binding of the fourth carboxylate pendant is unfavorable, probably due to the electrostatic repulsion and/or steric reasons.

V.3. Physico-chemical characterization of [Mn(OPMMA)]

Beside the development of highly inert Gd-based CAs, the other possible solution to handle the question of the *in vivo* stability is the replacement of the Gd^{3+} ion with other essential paramagnetic metal ion.[131] The most promising candidate is the Mn^{2+}, since the human body has efficient routes to control it homeostasis. Indeed, the Mn^{2+} ion has also to be chelated in the form of stable complexes, since its LD_{50} value (0.1-0.3 mmol/kg) is similar to that of Gd^{3+}.[132]

The development of Mn(II)-based CAs, however, is challenging due to the different coordination chemistry of the Mn^{2+}, thus the ligands suitable for the complexation of Gd^{3+} cannot be applied for Mn^{2+} chelation. The $DTPA^{5-}$ and $DOTA^{4-}$ derivatives usually possessing 8 donor atoms, form thermodynamically stable and the macrocyclic ones highly inert chelates with Mn(II) ion, the relaxivity of those complexes is limited to the outer sphere contribution because there is no water molecule in their inner sphere of the chelates due to the lower CN of the Mn^{2+}.[30,39] Thus, to reduce the number of donor atoms of the ligands is indispensable issue, which, of course, has an overall impact on the properties of the chelates.[39]

The O-pyclen macrocycle has been developed for the same reason, in which the N donor atom located opposite to the pyridine nitrogen was replaced by an etheric O atom.[33] Based on the excellent result obtained for the $[Gd(OPDMA)]^{-}$, the mono-malonate derivative of the O-pyclen ligand has been synthetized (Figure 26) and the physico-chemical characterization of its Mn^{2+} complex has been performed.

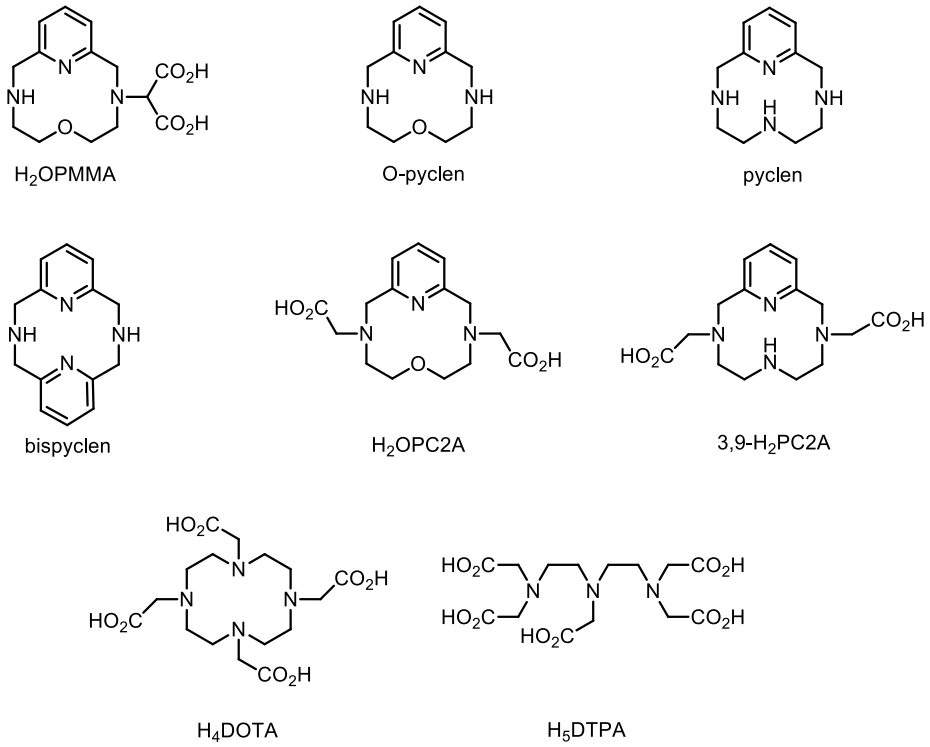

Figure 26. Structure of ligands mentioned in this chapter.

V.3.1. Thermodynamic and kinetic characterization of [Mn(OPMMA)]

pH potentiometric method was used to determine the protonation and stability constants of the ligand and Mn^{2+} complex in the presence of NaCl (I = 0.15 M) at 25 °C to mimic the physiological conditions. The raw data (V(ml)-pH data pairs) delivered by the titrations were analyzed with the PSEQUAD program.[77]

The calculations delivered four pK_as for the $OPMMA^{2-}$ which are presented in Table 10 and compared with the corresponding values obtained for H_2OPC2A and 3,9-H_2PC2A ligands.

According to the results published by Csupász and coworkers[33] for the H_2OPC2A and by Garda and coworkers[40] for the 3,9-H_2PC2A ligands (Table 10), the first two protonation of OPMMA^{2-} occur on the nitrogen donors of the macrocyclic backbone, while the remaining ones, can be linked to the protonation of the malonate.

The value of the logK_1 of H_2OPMMA is three orders of magnitudes lower than that of 3,9-H_2PC2A, which is the result of the replacement of the *trans*-N to a less basic, etheric O donor. At the same time, the ”fusion” of the acetates into malonate increases the basicity, probably because of the presence of the unsubstituted amine and the presence of stronger H-bond between N and O donors.

Table 10. The protonation constants (logK_i) of the ligands (OPMMA^{2-}, OPC2A^{2-} and 3,9-PC2A^{2-}) and the protonation and stability constants of their Mn^{2+} complexes.

	OPMMA^{2-} [a]	OPC2A^{2-} [b]	3,9-PC2A^{2-} [c]
logK_1	9.17(5)	7.73	12.25
logK_2	8.19(5)	7.66	5.97
logK_3	3.26(7)	2.13	3.47
logK_4	1.29(9)	–	1.99
ΣlogK₂	***17.36***	***15.39***	***18.22***
logK_{MnL}	10.07(5)	13.03	17.09
logK_{MnHL}	–	2.40	2.14
log$K_{Mn(OH)L}$	11.00(7)	11.49	–
pMn [d]	***6.27***	***8.69***	***8.64***

[a] 3σ standard deviations are indicated in parenthesis. I = 0.15 M NaCl, T = 25 °C, [b] Ref.[33], [c] Ref.[40], [d] Ref[133], pMn = −log[Mn(II)$_{free}$], $c_{Mn(II)} = c_L$ = 0.01 mM, pH = 7.4

For the better comparison of the ligands' basicity, the sum of the protonation constants of the macrocycles have been calculated ($\log K_1 + \log K_2 = \Sigma\log K_2$), since these processes have essential effect on the formation of in-cage complex. Comparing $\Sigma\log K_2$ values, one can conclude that the basicity of the $OPMMA^{2-}$ falls between those of the reference chelators considered here.

Since, usually higher basicity results in higher stability constants, furthermore, the size of the macrocycles, the nature and number of the donor atoms are similar for these chelators, the $\log K_{MnL}$ of [Mn(OPMMA)] was expected to be higher than that of [Mn(OPC2A)]. Contrarily, the stability of the complex is 3 and 7 orders of magnitude lower than that of [Mn(OPC2A)] and [Mn(3,9-PC2A)], respectively. The pMn values have also been calculated for physiological pH according to the method proposed by Drahos and coworkers[133] and listed in Table 10. The comparison of the pMns shows that the stability of our complex is more than two orders of magnitude lower than that of [Mn(OPC2A)] and [Mn(3,9-PC2A)]. Due to the lower stability, circa 5% of Mn^{2+} remains uncomplexed at pH = 7.4 under these conditions, so in the subsequent studies 10% of ligand excess was used to force the 100% complexation. It is also important to mention that the complexation at 1 mM complex concentration is 99% (without ligand excess, pMn = 5.2) at pH = 7.4.

In order to prove the validity of the model that was established based on the pH potentiometric results, ^{1}H-relaxometric measurements were carried out on the Mn(II)-OPMMA system. The pH - $1/T_1$ data pairs are compared and presented in Figure 27 along with the species distribution curves.

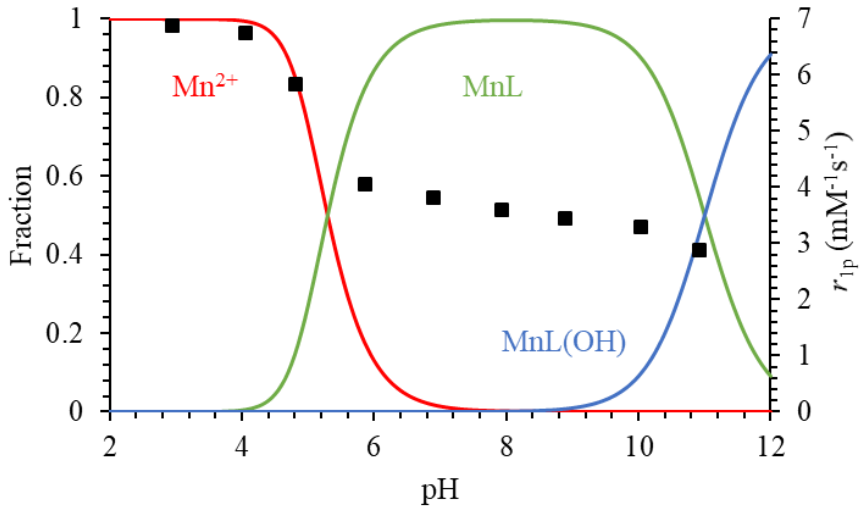

Figure 27. Species distribution curves of Mn^{2+}–$OPMMA^{4-}$ system ($c_{Mn(II)} = c_L$ = 1 mM), togheter with the pH-dependent relaxivities (T = 25 °C, I = 0.15 M NaCl, 0.49 T).

Based on the titrations, the formation of the [Mn(OPMMA)] complex and its hydroxide species ([Mn(OH)(OPMMA)] can be assumed (Table 10), which was confirmed by the comparison of the pH-$1/T_1$ profile and the distribution curves, thus we can stated that this equilibrium model sufficiently describes the system (Figure 27). The R_{1p} values are continuously decreasing from pH = 3 parallel with the formation of the ML complex, which finishes around pH ~ 7.5. At higher pH values, the process of the deprotonation of the coordinated water molecule becomes dominant, leading to the further decrease of the relaxivity.

The inertness of the [Mn(OPMMA)] complex was investigated by spectrophotometric method. The decomplexation reactions were studied by metal exchange reactions using Cu^{2+} ion as a scavenger in 10-fold excess to ensure the pseudo-first order conditions, thus the rate constants

obtained are pseudo-first order rate constants (k_{obs}) and can be described similarly to Equation 27.

The preliminary experiments showed that the dissociation of the [Mn(OPMMA)] is too fast to be investigated by conventional spectrophotometry, therefore stopped-flow method was used. The dissociation of the Mn^{2+}-based macrocyclic polyamino polycarboxylate complexes mainly occur through proton-assisted pathways but in some cases the spontaneous and/or the metal-assisted dechelation can also operate.[2] For the metal-assisted pathway, a dinuclear intermediate complex possessing sufficiently high stability must be formed. In the proton-assisted dissociation the chelate needs to be protonated, which occurs mainly on the pendant(s) followed by the migration of the proton to the most basic donor atom of the ligand inducing a structural rearrangement of the complex, which leads to the liberation of the metal ion. Since, our complex possesses very low inertness, the effect of the exchanging metal ion was not investigated.

The k_{obs} values calculated from the absorbance-time data pairs increase with increasing $[H^+]$ showing a saturation-like behavior at higher pH values (Figure 28), indicating the formation of a relatively stable monoprotonated intermediate. Taking into account all the parameters, the proton-assisted dissociation of [Mn(OPMMA)] can be given by equation 29:

$$k_{obs} = k_1[H^+]/(1+K_1^H[H^+]) \quad (29)$$

The rate constant and the protonation constant obtained are presented in Table 11, where the corresponding values determined for the Mn^{2+} complex of $OPC2A^{2-}$ and 3,9-$PC2A^{2-}$ are also shown.

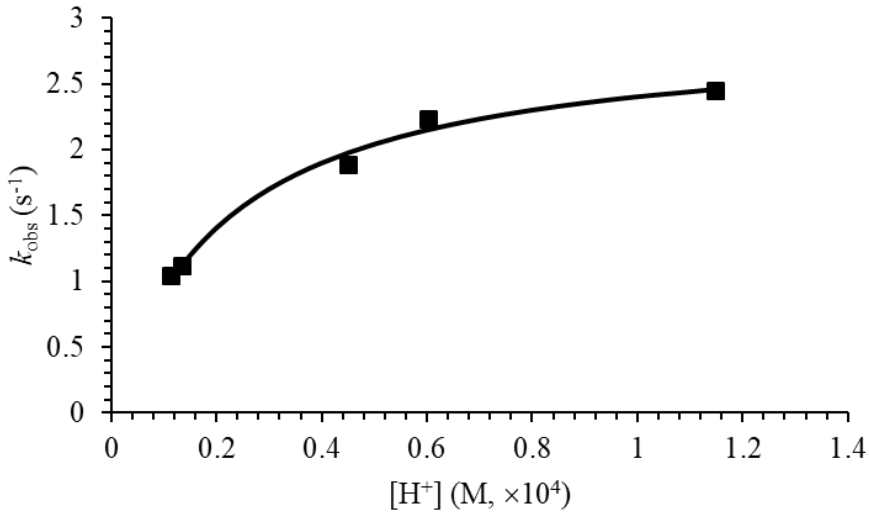

Figure 28. Dependence of the k_{obs} on [H^+] for the [Mn(OPMMA)] complex (25 °C, 0.15 M NaCl). The solid line corresponds to the best fit.

Table 11. Rate and equilibrium constants for the dissociation of Mn^{2+} complexes of $OPMMA^{2-}$, $OPC2A^{2-}$ and 3,9-$PC2A^{2-}$(I = 0.15 M NaCl, T = 25 °C, charges are omitted for simplicity)

Mn^{2+} complexes	OPMMA	OPC2A[b]	3,9-PC2A[c]
k_0 (s^{-1})	–	$(8.6\pm1.1)\times10^{-6}$	–
k_1 ($M^{-1}s^{-1}$)	$(1.4\pm0.1)\times10^{5}$	2.81±0.07	221±5
K_1^H	$(4.7\pm0.6)\times10^{4}$	–	$(3.6\pm0.5)\times10^{3}$
$t_{1/2}$(h)[c]	***3.5×10^{-2}***	***21.9***	***21.9***

[a] Ref.[33], [b] Ref.[40], [c] pH = 7.4

Interestingly, the logK_1^H value (logK_1^H = 4.67) characterizing the protonation of the [Mn(OPMMA)] complex in the dissociation process was found to be one order of magnitude higher than that was determined for the [Mn(3,9-PC2A)] complex (logK_1^H = 3.55). Furthermore, this protonation constant is higher than those were determined for the carboxylates of the $OPMMA^{2-}$ ligand (logK_3 = 3.26 and logK_4 = 1.29). This phenomenon indicates that the protonation of the complex probably occurs directly on the unsubstituted macrocycle N donor, which seems to promote the easier structural rearrangement of the complex and the faster release of the Mn(II) ion. In order to get a better comparison for the inertness of the three chelates, the half-lives ($t_{1/2}$) of the dissociation reactions have been also calculated for pH = 7.4 (Table 11). The $t_{1/2}$ values show that the inertness of [Mn(OPMMA)] is more than two orders of magnitude lower than that of the Mn^{2+} complexes of $OPC2A^{2-}$ and 3,9-$PC2A^{2-}$, probably because of the aforementioned reasons.

V.3.2. ^{1}H NMRD and ^{17}O NMR characterization of [Mn(OPMMA)]

The longitudinal (r_{1p}) and transverse (r_{2p}) relaxation rates of the Mn^{2+} complex formed with $OPMMA^{2-}$ ligand have been determined in solutions (pH = 7.4, I = 0.15 M NaCl) at different temperatures (25 and 37 °C) and field strength (20 and 60 MHz, Table 12).

The relaxivity values of [Mn(OPMMA)] are slightly higher (except the r_{2p} relaxivities recorded at 60 MHz) than those of [Mn(OPC2A)] and [Mn(3,9-PC2A)]. The slightly increased relaxivity can be the result of the assymetric structure of the ligand, which results a more open structure.

Table 12. r_{1p} values ($mM^{-1}s^{-1}$) determined for Mn^{2+} complexes of $OPMMA^{2-}$ and other ligands used for comparative purposes at pH = 7.4, 25/37 °C and 20/60 MHz (charges are omitted for simplicity).

	25/37 °C	OPMMA	OPC2A[a]	3,9-PC2A[b]
0.47 T	r_{1p}	3.48/2.84	3.13/2.54	2.91
	r_{2p}	5.85/4.70	5.15/4.17	3.96
1.41 T	r_{1p}	2.91/2.19	2.72/2.06	2.29
	r_{2p}	8.06/5.27	9.90/7.37	4.82

[a] Ref.[33], [b] Ref.[40], [c] pH = 7.4

Similarly to the $[Gd(OPDMA)]^-$ complex, ^{17}O and ^{1}H NMRD measurements were carried out to determine the parameters governing the relaxivity of the [Mn(OPMMA)] complex. The NMRD profiles have been recorded in the frequency range of 0.04–80 MHz at 25 and 37 °C (c_{MnL} = 1.0 mM). The ^{17}O NMR measurements have been performed at 9.4 T on a complex solution (c_{MnL} = 6.4 mM) and a diamagnetic reference ($HClO_4$, pH = 3.3) in aqueous solution. The $1/T_1$ values and the chemical shifts of the paramagnetic and diamagnetic samples did not differ significantly, so those were omitted from the calculations. The simultaneous analysis of the ^{17}O and NMRD data did not provide reasonable results, so those were fitted separately (Figure 29 and 30).[62,63,79–81] Thus, the water exchange rate and its activation enthalpy obtained form ^{17}O experiments were fixed in the fitting procedure of NMRD data. In this way, the k_{ex}, $\Delta H^{\ddagger}$, $1/T_{1e}$, τ_r, E_r (activation energy of τ_r), the square of the zero-field splitting energy (ZFS, Δ^2) and the correlation time for its modulation (τ_v) have been determined. The obtained parameters are presented in Table 13 together with the corresponding values gained for the comparative complexes.

Based on literature evidences, $A_0/\hbar$ was set to 33×10^6 rad/s, the distance between the metal ion, and the inner and outer sphere water protons were fixed to 2.83 Å and 3.6 Å, respectively; D_{MnH} was set to 2.6×10^{-9} m^2/s and E_{DMnH} to 22 kJ/mol, furthermore, E_v was fixed to 1.0 kJ/mol. The q was set to 1 based on the relaxivity values.

The $\ln(1/T_{2r})$ values (Figure 29) increase continuously with decreasing temperature with a small lean at low temperatures reaching the intermediate region, thus the maximum of the curve cannot be determined accurately. For this reason, the calculation of q from the transverse relaxation rates according to the method proposed by Gale,[38] delivered only a value of 0.5 ± 0.2. The contribution of the water exchange to the overall correlation time ($1/\tau_c = k_{ex} + 1/T_{1e}$, $1/T_{1e} = (8.1\pm0.6) \times 10^7$ s^{-1}) was calculated and found to be increasing from 52 to 93% in the investigated temperature range, which ensures the accurate determination of k_{ex}.

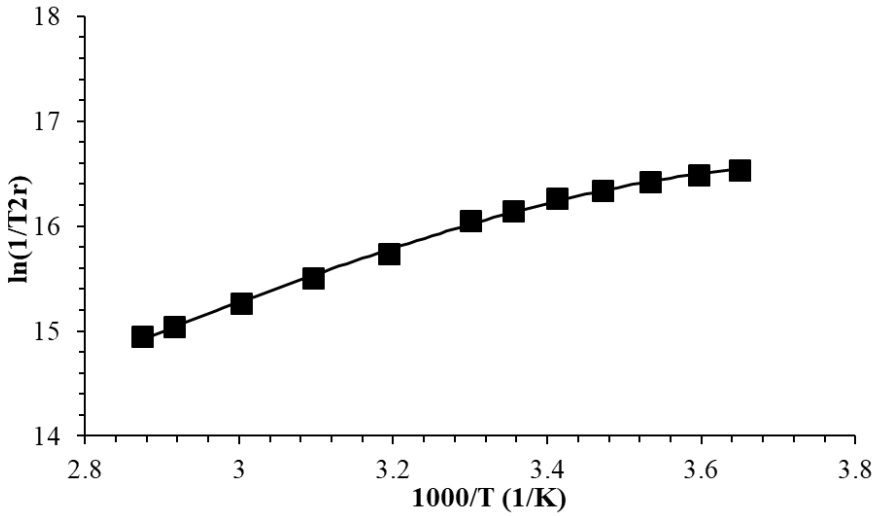

Figure 29. $1/T_{2r}$ values determined for [Mn(OPMMA)] (9.4 T). The solid line corresponds to the fit of the data.

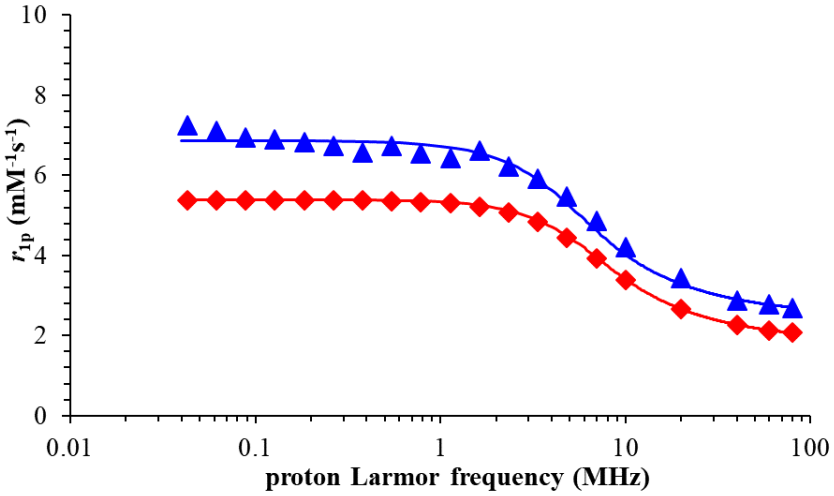

Figure 30. ^{1}H NMRD profiles recorded for [Mn(OPMMA)] at 25 (▲) and 37 (♦) °C (c_{MnL} = 1.0 mM).

Table 13. Best-fit parameters gained for [Mn(OPMMA)] from the analysis of ^{1}H NMRD and ^{17}O NMR data along with the corresponding values found for the Mn^{2+} complexes formed with $OPC2A^{2-}$ and $3,9\text{-}PC2A^{2-}$ ligands (charges are omitted for simplicity).

Parameter	OPMMA	OPC2A[c]	3,9-PC2A[d]
k_{ex}^{298} ($\times 10^{7}$ s^{-1})[a]	22.1 ± 0.01	5.3	12.6
$\Delta H^{\ddagger}$ (kJ mol^{-1})[a]	23.1 ± 0.1	28.5	37.5
$\Delta S^{\ddagger}$ (JK^{-1}mol^{-1})[a]	-8 ± 1	-1.9	–
E_{rH} / (kJ mol^{-1})[b]	17.2 ± 1.6	14.8	–
τ_{rH}^{298} (ps)[b]	55 ± 3	40.0	–
τ_{v}^{298} (ps)[b]	33 ± 11	19.3	–
Δ^2 ($\times 10^{19}$ s^{-2})[b]	2.1 ± 0.9	1.8	–

[a] from ^{17}O NMR; [b] from NMRD; [c] Ref.[33], [d] Ref.[40]

The water exchange rate of the [Mn(OPMMA)] is circa two-times higher than that was obtained for the [Mn(3,9-PC2A)] complex, and more than fourfold higher the that of [Mn(OPC2A)]. This behaviour surely the effect of the structural differences. The incorporation of the O atom into the macrocyclic structure can increase the rigidity of the coordination cage, in contrast, the asymmetric structure of the ligand decreases that. The small negative value of $\Delta S^{\ddagger}$ (-8 ± 1 $JK^{-1}mol^{-1}$) gained for the complex indicating associatively activated interchange mechanism for water exchange. The ^{1}H NMRD profiles have the typical shape of low molecular-weight complexes with a single dispersion (Figure 30). Since, the r_{1p} values of [Mn(OPMMA)] decrease with increasing temperature its relaxivity is controlled by fast rotation, as it was earlier found for numerous Mn(II) complexes.[33,34,134] The τ_{rH}^{298} is somewhat higher than that was obtained for [Mn(OPC2A)], which can be the result of the less compact structure of [Mn(OPMMA)].

V.3.3. DFT calculations for [Mn(OPMMA)]

A model for the coordination mode of the [Mn(OPMMA)] complex was computed using DFT. The geometry of the complex was optimized by including one inner-sphere water molecule and two explicit second-sphere water molecules, while the bulk solvent was accounted for using the polarized continuum model. The DFT-optimized structure of the complex is presented in Figure 31 and the corresponding Cartesian coordinates with the energy values are reported in Appendix (Table A3).

DFT delivered a capped trigonal prismatic coordination geometry, in which all the donor atoms of the macrocyclic ring (3N,O) coordinates to the Mn(II) ion together with the two carboxylate groups of the

pendant The strong interaction between the metal ion and the carboxylates yield somewhat shorter Mn(II)-O bonds (2.18 and 2.20 Å). The remaining coordination site is occupied by a water molecule which forms a strong hydrogen bond network with the two second-sphere water molecules and one of the carboxylate pendant arms. The Mn(II)-O_{water} distance was calculated to be 2.35 Å which falls into the range of the first coordination shell of water.

DFT offers the possibility to calculate the ^{17}O hyperfine coupling constant. The $A_0/\hbar$ was estimated to be -39.8 $\times 10^6$ rad s^{-1} (A = –6.34 MHz) which is in the typical range for Mn(II) chelates and confirms the proposed structure in solution.

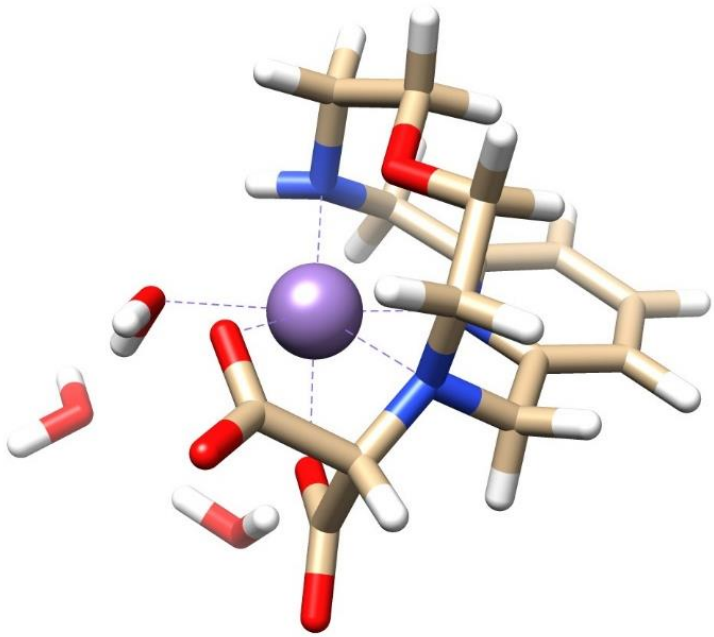

Figure 31. DFT optimized structure of the [Mn(OPMMA)] complex.

VI. Summary

We have studied in detail the physicochemical characteristics of $[Gd(OPDMA)]^-$ and [Mn(OPMMA)] complexes. This includes the thermodynamic stability, kinetic inertness and relaxation properties. Additionally, in order to get a better insight the solution structure of the complexes studied, DFT calculations were also performed. The summary of our results is as follows:

1. The basicity of H_4OPDMA is orders of magnitude lower than that of the comparative ligands presented in this paper due to the decrease in basicity caused by the presence of the pyridine nitrogen and etheric oxygen in the macrocylic ring.

2. The stability constant of $[Gd(OPDMA)]^-$ is at least two orders of magnitude lower than that of the comparative complexes. The pGd of $[Gd(OPDMA)]^-$ is lower than that of $DTPA^{5-}$ and $DOTA^{4-}$ complexes, but higher than that of the $AAZTA^{4-}$ and $PCTA^{3-}$ chelates. Based on the DFT calculation, one carboxylate group is not coordinated to the metal center which can be easily protonated at lower pH ($\log K_{GdL}^{H} = 2.09(5)$).

3. Based on the $t_{1/2}$ values, the inertness of $[Gd(OPDMA)]^-$ higher than that of the open-chain DTPA and AAZTA complexes, but orders of magnitudes lower than that was obtained for the macrocyclic PCTA and DOTA chelates. The $t_{1/2}$ values calculated for 37 °C and pH = 7.4, were found to be years (3.2 y (Cu^{2+}) and 4.4 y (Eu^{3+}) depending on the nature of the exchanging metal ion), which is sufficient for *in vivo* applications, if other dissociation pathways or enzymatic processes are not operative in the body.

4. The r_{1p} values obtained for $[Gd(OPDMA)]^-$ at different field strengths (0.49 T and 1.41 T) and temperatures (25 and 37 °C) are

comparable to those of the analogous chelates. There is no significant difference between the r_{1p} values of $[Gd(OPDMA)]^-$ and that of the q = 1 chelates, which indicates that one water molecule is coordinated in the inner sphere of the complex. This observation was supported by luminescence measurements on Eu^{3+} complex, delivering q = 1.2±0.1 value for both pH = 7 and 3. The r_{1p} values determined in the presence of human serum albumin (c_{HSA} = 0.8 mM) indicate a negligible interaction between the complex and the protein.

5. The water exchange rate and other relaxation parameters were gained by temperature dependent NMRD and ^{17}O NMR. The k_{ex}^{298} of $[Gd(OPDMA)]^-$ is the highest among all complexes compared. The negative value of $\Delta S^{\ddagger}$ indicates an associative mechanism for the water exchange process in contrast with that of $[Gd(DTPA)]^{2-}$ and $[Gd(DOTA)]^-$ chelates, where dissociative mechanism was found. The value of $A/\hbar$ is typical for Gd(III) complexes and. The rotational correlation time (τ_R) of our complex is close to those reported for other complexes of similar size. Interestingly, the electron spin relaxation of the $[Gd(OPDMA)]^-$ complex is relatively fast based on the higher Δ^2. This phenomenon is likely the result of the less symmetric structure.

6. DFT calculations were performed to characterize the structure of $[Gd(OPDMA)]^-$. The predicted structure shows a bicapped trigonal prismatic geometry where the ligand coordinates to the Gd^{3+} ion in a heptadentate manner. The inner sphere of the complex is completed with a H_2O molecule coordination, yielding an overall coordination number of eight (CN=8). The Gd(III)-O_{water} distance was found to be 2.47 Å which falls into the range of first coordination shell of water. Additionally, DFT also predicted a CN=9 coordination mode for the

complex, where all carboxylate arms are bound to the Gd^{3+} ion completed with an inner-sphere H_2O molecule. In this calculation the distance between the Gd(III) and O of the water molecule is relatively long and the ^{17}O hyperfine coupling constant is unrealistic.

7. The value of the $\log K_1$ of H_2OPMMA is three orders of magnitudes lower than that of H_2OPC2A, which is the result of the replacement of the *trans*-N to a less basic, etheric O donor. At the same time, the ”fusion” of the acetates into malonate increases the basicity, probably because of the presence of the unsubstituted amine and the presence of stronger H-bond between N and O donors. The $\Sigma \log K_2$ value, characterizing the basicity of the macrocycle, falls between those of the reference chelators.

8. The $\log K_{MnL}$ of the complex [Mn(OPMMA)] is 3 and 7 orders of magnitude lower than that of [Mn(OPC2A)] and [Mn(3,9-PC2A)], respectively. In addition to this pMn value of the complex is more than two orders of magnitude lower than that of [Mn(OPC2A)] and [Mn(3,9-PC2A)], which results a pMn value being 6.27 calculated for physiological pH ($c_{Mn(II)} = c_L = 0.01$ mM).

9. The inertness of the [Mn(OPMMA)] complex was studied by exchange reactions with 10-fold excess Cu^{2+} ion as a scavenger . Since the dissociation of [Mn(OPMMA)] was too fast for conventional spectrophotometry, stopped-flow method was used. The $t_{1/2}$ value (2.1 min) calculated for pH = 7.4 shows that the inertness of [Mn(OPMMA)] is more than two orders of magnitude lower than that of [Mn(OPC2A)] and [Mn(3,9-PC2A)] complexes.

10. The relaxivitiy values of [Mn(OPMMA)] is slightly higher than those of the [Mn(OPC2A)] and [Mn(3,9-PC2A)] used for comparative

purposes, which obviously the result of the assymetric structure of the [Mn(OPMMA)]

11. As in the case of $[Gd(OPDMA)]^{-}$ complex, ^{17}O and ^{1}H NMRD measurements were also performed to determine the relaxation parameters of [Mn(OPMMA)]. The water exchange rate of the [Mn(OPMMA)] is circa two-times higher than that was obtained for the [Mn(3,9-PC2A)] complex, and more than fourfold higher the that of [Mn(OPC2A)]. This behaviour surely the result of the structural differences. The small negative value of $\Delta S^{\ddagger}$ (-8(1) $JK^{-1}mol^{-1}$) obtained for the complex indicating interchange mechanism. The τ_{rH}^{298} is somewhat higher than that was obtained for [Mn(OPC2A)], which can be the result of the less compact structure of [Mn(OPMMA)].

12. The DFT calculations delivered a capped trigonal prismatic coordination geometry for [Mn(OPMMA)], in which all the donor atoms of the ligand are coordinated to the Mn(II) ion. The remaining coordination site is occupied by a water molecule which forms a strong hydrogen bond network with the two second-sphere water molecules and one of the carboxylate pendant arms. The Mn(II)-O_{water} distance was calculated to be 2.35 Å which falls into the range of the first coordination shell of water.

VII. References

(1) Cheong, B. Y. C.; Wilson, J. M.; Preventza, O. A.; Muthupillai, R. Gadolinium-Based Contrast Agents: Updates and Answers to Typical Questions Regarding Gadolinium Use. *Texas Heart Institute Journal* **2022**, *49* (3), e217680. https://doi.org/10.14503/THIJ-21-7680.

(2) *The Chemistry of Contrast Agents in Medical Magnetic Resonance Imaging*, Second edition.; Helm, L., Merbach, A. E., Tóth, É., Eds.; John Wiley & Sons Inc: Hoboken, NJ, 2013.

(3) Mitchell, D. G. LIVER I: CURRENTLY AVAILABLE GADOLINIUM CHELATES. *Magnetic Resonance Imaging Clinics of North America* **1996**, *4* (1), 37–51. https://doi.org/10.1016/S1064-9689(21)00552-3.

(4) Xiao, Y.-D.; Paudel, R.; Liu, J.; Ma, C.; Zhang, Z.-S.; Zhou, S.-K. MRI Contrast Agents: Classification and Application (Review). *International Journal of Molecular Medicine* **2016**, *38* (5), 1319–1326. https://doi.org/10.3892/ijmm.2016.2744.

(5) Kanal, E. Gadolinium Based Contrast Agents (GBCA): Safety Overview after 3 Decades of Clinical Experience. *Magnetic Resonance Imaging* **2016**, *34* (10), 1341–1345. https://doi.org/10.1016/j.mri.2016.08.017.

(6) Wahsner, J.; Gale, E. M.; Rodríguez-Rodríguez, A.; Caravan, P. Chemistry of MRI Contrast Agents: Current Challenges and New Frontiers. *Chem. Rev.* **2019**, *119* (2), 957–1057. https://doi.org/10.1021/acs.chemrev.8b00363.

(7) Do, Q. N.; Lenkinski, R. E.; Tircso, G.; Kovacs, Z. How the Chemical Properties of GBCAs Influence Their Safety Profiles In Vivo. *Molecules* **2021**, *27* (1), 58. https://doi.org/10.3390/molecules27010058.

(8) Mathur, M.; Jones, J. R.; Weinreb, J. C. Gadolinium Deposition and Nephrogenic Systemic Fibrosis: A Radiologist's Primer. *RadioGraphics* **2020**, *40* (1), 153–162. https://doi.org/10.1148/rg.2020190110.

(9) Lancelot, E.; Raynaud, J.-S.; Desché, P. Current and Future MR Contrast Agents: Seeking a Better Chemical Stability and Relaxivity for Optimal Safety and Efficacy. *Invest Radiol* **2020**, *55* (9), 578–588. https://doi.org/10.1097/RLI.0000000000000684.

(10) Tircsó, G.; Regueiro-Figueroa, M.; Nagy, V.; Garda, Z.; Garai, T.; Kálmán, F. K.; Esteban-Gómez, D.; Tóth, É.; Platas-Iglesias, C. Approaching the Kinetic Inertness of Macrocyclic Gadolinium(III)-Based MRI Contrast Agents with Highly Rigid Open-Chain Derivatives. *Chem. Eur. J.* **2016**, *22* (3), 896–901. https://doi.org/10.1002/chem.201503836.

(11) Rodríguez-Rodríguez, A.; Regueiro-Figueroa, M.; Esteban-Gómez, D.; Tripier, R.; Tircsó, G.; Kálmán, F. K.; Bényei, A. C.; Tóth, I.; Blas, A. de; Rodríguez-Blas, T.; Platas-Iglesias, C. Complexation of Ln^{3+} Ions with Cyclam Dipicolinates: A Small Bridge That Makes Huge Differences in Structure, Equilibrium, and Kinetic Properties. *Inorg. Chem.* **2016**, *55* (5), 2227–2239. https://doi.org/10.1021/acs.inorgchem.5b02627.

(12) Platas-Iglesias, C.; Mato-Iglesias, M.; Djanashvili, K.; Muller, R. N.; Elst, L. V.; Peters, J. A.; de Blas, A.; Rodríguez-Blas, T. Lanthanide Chelates Containing Pyridine Units with Potential Application as Contrast Agents in Magnetic Resonance Imaging. *Chem. Eur. J.* **2004**, *10* (14), 3579–3590. https://doi.org/10.1002/chem.200306031.

(13) Garda, Z.; Forgács, A.; Do, Q. N.; Kálmán, F. K.; Timári, S.; Baranyai, Z.; Tei, L.; Tóth, I.; Kovács, Z.; Tircsó, G. Physico-Chemical Properties of MnII Complexes Formed with Cis- and Trans-DO2A: Thermodynamic, Electrochemical and Kinetic Studies. *Journal of Inorganic Biochemistry* **2016**, *163*, 206–213. https://doi.org/10.1016/j.jinorgbio.2016.07.018.

(14) Baranyai, Z.; Carniato, F.; Nucera, A.; Horváth, D.; Tei, L.; Platas-Iglesias, C.; Botta, M. Defining the Conditions for the Development of the Emerging Class of Fe^{III} -Based MRI Contrast Agents. *Chem. Sci.* **2021**, *12* (33), 11138–11145. https://doi.org/10.1039/D1SC02200H.

(15) *Advanced Fluorescence Reporters in Chemistry and Biology II*; Demchenko, A. P., Ed.; Springer Series on Fluorescence; Springer Berlin Heidelberg: Berlin, Heidelberg, 2010; Vol. 9. https://doi.org/10.1007/978-3-642-04701-5.

(16) Weissman, S. I. Intramolecular Energy Transfer The Fluorescence of Complexes of Europium. *The Journal of Chemical Physics* **1942**, *10* (4), 214–217. https://doi.org/10.1063/1.1723709.

(17) Blomqvist, L.; Nordberg, G. F.; Nurchi, V. M.; Aaseth, J. O. Gadolinium in Medical Imaging—Usefulness, Toxic Reactions and Possible Countermeasures—A Review. *Biomolecules* **2022**, *12* (6), 742. https://doi.org/10.3390/biom12060742.

(18) Carr, D.; Brown, J.; Bydder, G.; Steiner, R.; Weinmann, H.; Speck, U.; Hall, A.; Young, I. Gadolinium-DTPA as a Contrast Agent in MRI: Initial Clinical Experience in 20 Patients. *American Journal of Roentgenology* **1984**, *143* (2), 215–224. https://doi.org/10.2214/ajr.143.2.215.

(19) Peshock, R. M.; Malloy, C. R.; Buja, L. M.; Nunnally, R. L.; Parkey, R. W.; Willerson, J. T. Magnetic Resonance Imaging of Acute Myocardial Infarction: Gadolinium Diethylenetriamine Pentaacetic Acid as a Marker of Reperfusion. *Circulation* **1986**, *74* (6), 1434–1440. https://doi.org/10.1161/01.CIR.74.6.1434.

(20) Allard, M.; Doucet, D.; Kien, P.; Bonnemain, B.; Caillé, J. M. Experimental Study of DOTA-Gadolinium Pharmacokinetics and Pharmacologic Properties: *Investigative Radiology* **1988**, *23*, S271–S274. https://doi.org/10.1097/00004424-198809001-00059.

(21) Normann, P. T.; Hals, P. A. In Vivo Stability and Excretion of Gadodiamide (GdDTPA-BMA), a Hydrophilic Gadolinium Complex Used as a Contrast Enhancing Agent for Magnetic Resonance Imaging. *European Journal of Drug Metabolism and Pharmacokinetics* **1995**, *20* (4), 307–313. https://doi.org/10.1007/BF03190250.

(22) Lauffer, R. B.; Parmelee, D. J.; Dunham, S. U.; Ouellet, H. S.; Dolan, R. P.; Witte, S.; McMurry, T. J.; Walovitch, R. C. MS-325: Albumin-Targeted Contrast Agent for MR Angiography. *Radiology* **1998**, *207* (2), 529–538. https://doi.org/10.1148/radiology.207.2.9577506.

(23) Wan, F.; Wu, L.; Chen, X.; Zhang, Y.; Jiang, L. Research Progress on Manganese Complexes as Contrast Agents for Magnetic Resonance Imaging. *Polyhedron* **2023**, *242*, 116489. https://doi.org/10.1016/j.poly.2023.116489.

(24) Holley, A. K.; Dhar, S. K.; Xu, Y.; St. Clair, D. K. Manganese Superoxide Dismutase: Beyond Life and Death. *Amino Acids* **2012**, *42* (1), 139–158. https://doi.org/10.1007/s00726-010-0600-9.

(25) Crossgrove, J.; Zheng, W. Manganese Toxicity upon Overexposure. *NMR in Biomedicine* **2004**, *17* (8), 544–553. https://doi.org/10.1002/nbm.931.

(26) Eisinger, J.; Fawaz-Estrup, F.; Shulman, R. G. Binding of Mn2+ to Nucleic Acids. *The Journal of Chemical Physics* **1965**, *42* (1), 43–53. https://doi.org/10.1063/1.1695717.

(27) Aschner, M.; Erikson, K. M.; Dorman, D. C. Manganese Dosimetry: Species Differences and Implications for Neurotoxicity. *Critical Reviews in Toxicology* **2005**, *35* (1), 1–32. https://doi.org/10.1080/10408440590905920.

(28) Gunter, T. E.; Puskin, J. S. Manganous Ion as a Spin Label in Studies of Mitochondrial Uptake of Manganese. *Biophysical Journal* **1972**, *12* (6), 625–635. https://doi.org/10.1016/S0006-3495(72)86108-3.

(29) Barandov, A.; Bartelle, B. B.; Gonzalez, B. A.; White, W. L.; Lippard, S. J.; Jasanoff, A. Membrane-Permeable Mn(III) Complexes for Molecular Magnetic Resonance Imaging of Intracellular Targets. *J. Am. Chem. Soc.* **2016**, *138* (17), 5483–5486. https://doi.org/10.1021/jacs.5b13337.

(30) Kálmán, F. K.; Tircsó, G. Kinetic Inertness of the Mn^{2+} Complexes Formed with AAZTA and Some Open-Chain EDTA Derivatives. *Inorg. Chem.* **2012**, *51* (19), 10065–10067. https://doi.org/10.1021/ic300832e.

(31) Nizou, G.; Molnár, E.; Hamon, N.; Kálmán, F. K.; Fougère, O.; Rousseaux, O.; Esteban-Gòmez, D.; Platas-Iglesias, C.; Beyler, M.;

Tircsó, G.; Tripier, R. Pyclen-Based Ligands Bearing Pendant Picolinate Arms for Gadolinium Complexation. *Inorg. Chem.* **2021**, *60* (4), 2390–2405. https://doi.org/10.1021/acs.inorgchem.0c03277.

(32) Toàn, N. M.; Vágner, A.; Nagy, G.; Ország, G.; Nagy, T.; Csikos, C.; Váradi, B.; Sajtos, G. Z.; Kapus, I.; Szoboszlai, Z.; Szikra, D.; Trencsényi, G.; Tircsó, G.; Garai, I. [^{52} Mn]Mn-BPPA-Trastuzumab: A Promising HER2-Specific PET Radiotracer. *J. Med. Chem.* **2024**, *67* (10), 8261–8270. https://doi.org/10.1021/acs.jmedchem.4c00344.

(33) Csupász, T.; Szücs, D.; Kálmán, F. K.; Hollóczki, O.; Fekete, A.; Szikra, D.; Tóth, É.; Tóth, I.; Tircsó, G. A New Oxygen Containing Pyclen-Type Ligand as a Manganese(II) Binder for MRI and 52Mn PET Applications: Equilibrium, Kinetic, Relaxometric, Structural and Radiochemical Studies. *Molecules* **2022**, *27* (2), 371. https://doi.org/10.3390/molecules27020371.

(34) Ndiaye, D.; Sy, M.; Pallier, A.; Même, S.; De Silva, I.; Lacerda, S.; Nonat, A. M.; Charbonnière, L. J.; Tóth, É. Unprecedented Kinetic Inertness for a Mn^{2+} -Bispidine Chelate: A Novel Structural Entry for Mn^{2+} -Based Imaging Agents. *Angew Chem Int Ed* **2020**, *59* (29), 11958–11963. https://doi.org/10.1002/anie.202003685.

(35) Forgács, A.; Tei, L.; Baranyai, Z.; Tóth, I.; Zékány, L.; Botta, M. A Bisamide Derivative of [Mn(1,4-DO2A)] – Solution Thermodynamic, Kinetic, and NMR Relaxometric Studies. *Eur. J. Inorg. Chem.* **2016**, *2016* (8), 1165–1174. https://doi.org/10.1002/ejic.201501415.

(36) Rocklage, S. M.; Cacheris, W. P.; Quay, S. C.; Hahn, F. E.; Raymond, K. N. Manganese(II) N,N'-Dipyridoxylethylenediamine-N,N'-Diacetate 5,5'-Bis(Phosphate). Synthesis and Characterization of a Paramagnetic Chelate for Magnetic Resonance Imaging Enhancement. *Inorg. Chem.* **1989**, *28* (3), 477–485. https://doi.org/10.1021/ic00302a019.

(37) Elizondo, G.; Fretz, C. J.; Stark, D. D.; Rocklage, S. M.; Quay, S. C.; Worah, D.; Tsang, Y. M.; Chen, M. C.; Ferrucci, J. T. Preclinical Evaluation of MnDPDP: New Paramagnetic Hepatobiliary Contrast Agent for MR Imaging. *Radiology* **1991**, *178* (1), 73–78. https://doi.org/10.1148/radiology.178.1.1898538.

(38) Gale, E. M.; Atanasova, I. P.; Blasi, F.; Ay, I.; Caravan, P. A Manganese Alternative to Gadolinium for MRI Contrast. *J. Am. Chem. Soc.* **2015**, *137* (49), 15548–15557. https://doi.org/10.1021/jacs.5b10748.

(39) Garda, Z.; Molnár, E.; Kálmán, F. K.; Botár, R.; Nagy, V.; Baranyai, Z.; Brücher, E.; Kovács, Z.; Tóth, I.; Tircsó, G. Effect of the Nature of Donor Atoms on the Thermodynamic, Kinetic and Relaxation Properties of Mn(II) Complexes Formed With Some Trisubstituted 12-Membered Macrocyclic Ligands. *Front. Chem.* **2018**, *6*, 232. https://doi.org/10.3389/fchem.2018.00232.

(40) Garda, Z.; Molnár, E.; Hamon, N.; Barriada, J. L.; Esteban-Gómez, D.; Váradi, B.; Nagy, V.; Pota, K.; Kálmán, F. K.; Tóth, I.; Lihi, N.; Platas-Iglesias, C.; Tóth, É.; Tripier, R.; Tircsó, G. Complexation of Mn(II) by Rigid Pyclen Diacetates: Equilibrium, Kinetic, Relaxometric, Density Functional Theory, and Superoxide Dismutase Activity Studies. *Inorg. Chem.* **2021**, *60* (2), 1133–1148. https://doi.org/10.1021/acs.inorgchem.0c03276.

(41) Brücher, E.; Tircsó, G.; Baranyai, Z.; Kovács, Z.; Sherry, A. D. Stability and Toxicity of Contrast Agents. In *The Chemistry of Contrast Agents in Medical Magnetic Resonance Imaging*; Merbach, A., Helm, L., Tóth, É., Eds.; Wiley, 2013; pp 157–208. https://doi.org/10.1002/9781118503652.ch4.

(42) Kumar, K.; Jin, T.; Wang, X.; Desreux, J. F.; Tweedle, M. F. Effect of Ligand Basicity on the Formation and Dissociation Equilibria and Kinetics of Gd3+ Complexes of Macrocyclic Polyamino Carboxylates. *Inorg. Chem.* **1994**, *33* (17), 3823–3829. https://doi.org/10.1021/ic00095a028.

(43) Tóth, É.; Király, R.; Platzek, J.; Radüchel, B.; Brücher, E. Equilibrium and Kinetic Studies on Complexes of 10-[2,3-Dihydroxy-(1-Hydroxymethyl)-Propyl]-1,4,7,10-Tetraazacyclododecane-1,4,7-Triacetate. *Inorganica Chimica Acta* **1996**, *249* (2), 191–199. https://doi.org/10.1016/0020-1693(96)05094-3.

(44) Port, M.; Idée, J.-M.; Medina, C.; Robic, C.; Sabatou, M.; Corot, C. Efficiency, Thermodynamic and Kinetic Stability of Marketed Gadolinium Chelates and Their Possible Clinical Consequences: A Critical Review. *Biometals* **2008**, *21* (4), 469–490. https://doi.org/10.1007/s10534-008-9135-x.

(45) Tweedle, M. F.; Hagan, J. J.; Kumar, K.; Mantha, S.; Chang, C. A. Reaction of Gadolinium Chelates with Endogenously Available Ions. *Magnetic Resonance Imaging* **1991**, *9* (3), 409–415. https://doi.org/10.1016/0730-725X(91)90429-P.

(46) Vitti, R. A. Gadolinium-Based Contrast Agents and Nephrogenic Systemic Fibrosis. *Radiology* **2009**, *250* (3), 959–960. https://doi.org/10.1148/radiol.2503081497.

(47) Toth, E.; Brucher, E.; Lazar, I.; Toth, I. Kinetics of Formation and Dissociation of Lanthanide(III)-DOTA Complexes. *Inorg. Chem.* **1994**, *33* (18), 4070–4076. https://doi.org/10.1021/ic00096a036.

(48) Sarka, L.; Burai, L.; Brücher, E. The Rates of the Exchange Reactions between [Gd(DTPA)]2− and the Endogenous Ions Cu2+ and Zn2+: A Kinetic Model for the Prediction of the In Vivo Stability of [Gd(DTPA)]2−, Used as a Contrast Agent in Magnetic Resonance Imaging. *Chem. Eur. J.* **2000**, *6* (4), 719–724. https://doi.org/10.1002/(SICI)1521-3765(20000218)6:4<719::AID-CHEM719>3.0.CO;2-2.

(49) Burai, L.; Hietapelto, V.; Király, R.; Tóth, É.; Brücher, E. Stability Constants and^{1} H Relaxation Effects of Ternary Complexes Formed between Gd-dtpa, Gd-dtpa-bma, Gd-dota, and Gd-edta and Citrate, Phosphate, and Carbonate Ions. *Magnetic Resonance in Med* **1997**, *38* (1), 146–150. https://doi.org/10.1002/mrm.1910380120.

(50) Baranyai, Z.; Pálinkás, Z.; Uggeri, F.; Maiocchi, A.; Aime, S.; Brücher, E. Dissociation Kinetics of Open-Chain and Macrocyclic Gadolinium(III)-Aminopolycarboxylate Complexes Related to Magnetic Resonance Imaging: Catalytic Effect of Endogenous Ligands. *Chemistry A European J* **2012**, *18* (51), 16426–16435. https://doi.org/10.1002/chem.201202930.

(51) Polasek, M.; Caravan, P. Is Macrocycle a Synonym for Kinetic Inertness in Gd(III) Complexes? Effect of Coordinating and Noncoordinating Substituents on Inertness and Relaxivity of Gd(III) Chelates with DO3A-like Ligands. *Inorg. Chem.* **2013**, *52* (7), 4084–4096. https://doi.org/10.1021/ic400227k.

(52) Pasha, A.; Tircsó, G.; Benyó, E. T.; Brücher, E.; Sherry, A. D. Synthesis and Characterization of DOTA-(Amide)$_4$ Derivatives: Equilibrium and Kinetic Behavior of Their Lanthanide(III) Complexes. *Eur J Inorg Chem* **2007**, *2007* (27), 4340–4349. https://doi.org/10.1002/ejic.200700354.

(53) Brücher, E.; Szarvas, P. Kinetic Study of the Isotope-Exchange Reactions of the Central Ions of the Lanthanide Ethylenediaminetetraacetate and Trans-1,2-Diaminocyclohexanetetraacetate Complexes. *Inorganica Chimica Acta* **1970**, *4*, 632–636. https://doi.org/10.1016/S0020-1693(00)93367-X.

(54) Gale, E. M.; Kenton, N.; Caravan, P. [Gd(CyPic3A)(H2O)2]−: A Stable, Bis(Aquated) and High-Relaxivity Gd(Iii) Complex. *Chem. Commun.* **2013**, *49* (73), 8060. https://doi.org/10.1039/c3cc44116d.

(55) Bonnet, C. S.; Laine, S.; Buron, F.; Tircsó, G.; Pallier, A.; Helm, L.; Suzenet, F.; Tóth, É. A Pyridine-Based Ligand with Two Hydrazine Functions for Lanthanide Chelation: Remarkable Kinetic Inertness for a Linear, Bishydrated Complex. *Inorg. Chem.* **2015**, *54* (12), 5991–6003. https://doi.org/10.1021/acs.inorgchem.5b00804.

(56) Rodríguez-Rodríguez, A.; Esteban-Gómez, D.; Tripier, R.; Tircsó, G.; Garda, Z.; Tóth, I.; de Blas, A.; Rodríguez-Blas, T.; Platas-Iglesias, C. Lanthanide(III) Complexes with a Reinforced Cyclam Ligand Show Unprecedented Kinetic Inertness. *J. Am. Chem. Soc.* **2014**, *136* (52), 17954–17957. https://doi.org/10.1021/ja511331n.

(57) Ndiaye, D.; Cieslik, P.; Wadepohl, H.; Pallier, A.; Même, S.; Comba, P.; Tóth, É. Mn^{2+} Bispidine Complex Combining Exceptional Stability, Inertness, and MRI Efficiency. *J. Am. Chem. Soc.* **2022**, *144* (48), 22212–22220. https://doi.org/10.1021/jacs.2c10108.

(58) Pota, K.; Molnár, E.; Kálmán, F. K.; Freire, D. M.; Tircsó, G.; Green, K. N. Manganese Complex of a Rigidified 15-Membered Macrocycle: A Comprehensive Study. *Inorg. Chem.* **2020**, *59* (16), 11366–11376. https://doi.org/10.1021/acs.inorgchem.0c01053.

(59) Lauterbur, P. C.; Dias, M. H. M.; Rudin, A. M. AUGMENTATION OF TISSUE WATER PROTON SPIN-LATTICE RELAXATION RATES BY IN VIVO ADDITION OF PARAMAGNETIC IONS. In *Electrons to Tissues*; Elsevier, 1978; pp 752–759. https://doi.org/10.1016/B978-0-12-225401-7.50093-X.

(60) Rahman, M. Magnetic Resonance Imaging and Iron-Oxide Nanoparticles in the Era of Personalized Medicine. *Nanotheranostics* **2023**, *7* (4), 424–449. https://doi.org/10.7150/ntno.86467.

(61) Tóth, É.; Helm, L.; Merbach, A. E. Relaxivity of MRI Contrast Agents. In *Contrast Agents I*; Krause, W., Ed.; De Meijere, A., Kessler, H., Ley, S. V., Thiem, J., Vögtle, F., Houk, K. N., Lehn, J.-M., Schreiber, S. L., Trost, B. M., Yamamoto, H., Series Eds.; Topics in Current Chemistry; Springer Berlin Heidelberg: Berlin, Heidelberg, 2002; Vol. 221, pp 61–101. https://doi.org/10.1007/3-540-45733-X_3.

(62) Swift, T. J.; Connick, R. E. NMR-Relaxation Mechanisms of O ^{17} in Aqueous Solutions of Paramagnetic Cations and the Lifetime of Water Molecules in the First Coordination Sphere. *The Journal of Chemical Physics* **1962**, *37* (2), 307–320. https://doi.org/10.1063/1.1701321.

(63) Swift, T. J.; Connick, R. E. Erratum: NMR-Relaxation Mechanisms of ^{17} O in Aqueous Solutions of Paramagnetic Cations and the Lifetime of Water Molecules in the First Coordination Sphere. *The Journal of Chemical Physics* **1964**, *41* (8), 2553–2554. https://doi.org/10.1063/1.1726303.

(64) Datta, A.; Raymond, K. N. Gd−Hydroxypyridinone (HOPO)-Based High-Relaxivity Magnetic Resonance Imaging (MRI) Contrast Agents. *Acc. Chem. Res.* **2009**, *42* (7), 938–947. https://doi.org/10.1021/ar800250h.

(65) Floyd, W. C.; Klemm, P. J.; Smiles, D. E.; Kohlgruber, A. C.; Pierre, V. C.; Mynar, J. L.; Fréchet, J. M. J.; Raymond, K. N. Conjugation Effects of Various Linkers on Gd(III) MRI Contrast Agents with Dendrimers: Optimizing the Hydroxypyridinonate (HOPO) Ligands with Nontoxic, Degradable Esteramide (EA) Dendrimers for High Relaxivity. *J. Am. Chem. Soc.* **2011**, *133* (8), 2390–2393. https://doi.org/10.1021/ja110582e.

(66) Heffern, M. C.; Matosziuk, L. M.; Meade, T. J. Lanthanide Probes for Bioresponsive Imaging. *Chem. Rev.* **2014**, *114* (8), 4496–4539. https://doi.org/10.1021/cr400477t.

(67) Aime, S.; Barge, A.; Bruce, J. I.; Botta, M.; Howard, J. A. K.; Moloney, J. M.; Parker, D.; De Sousa, A. S.; Woods, M. NMR, Relaxometric, and Structural Studies of the Hydration and Exchange Dynamics of

Cationic Lanthanide Complexes of Macrocyclic Tetraamide Ligands. *J. Am. Chem. Soc.* **1999**, *121* (24), 5762–5771. https://doi.org/10.1021/ja990225d.

(68) Jászberényi, Z.; Sour, A.; Tóth, É.; Benmelouka, M.; Merbach, A. E. Fine-Tuning Water Exchange on GdIII Poly(Amino Carboxylates) by Modulation of Steric Crowding. *Dalton Trans.* **2005**, No. 16, 2713. https://doi.org/10.1039/b506702b.

(69) Laus, S.; Ruloff, R.; Tóth, É.; Merbach, A. E. Gd^{III} Complexes with Fast Water Exchange and High Thermodynamic Stability: Potential Building Blocks for High-Relaxivity MRI Contrast Agents. *Chemistry A European J* **2003**, *9* (15), 3555–3566. https://doi.org/10.1002/chem.200204612.

(70) Ruloff, R.; Tóth, É.; Scopelliti, R.; Tripier, R.; Handel, H.; Merbach, A. E. Accelerating Water Exchange for Gd^{III} Chelates by Steric Compression around the Water Binding Site. *Chem. Commun.* **2002**, No. 22, 2630–2631. https://doi.org/10.1039/B207713B.

(71) Woods, M.; Aime, S.; Botta, M.; Howard, J. A. K.; Moloney, J. M.; Navet, M.; Parker, D.; Port, M.; Rousseaux, O. Correlation of Water Exchange Rate with Isomeric Composition in Diastereoisomeric Gadolinium Complexes of Tetra(Carboxyethyl)Dota and Related Macrocyclic Ligands. *J. Am. Chem. Soc.* **2000**, *122* (40), 9781–9792. https://doi.org/10.1021/ja994492v.

(72) Shen, C.; New, E. J. Promising Strategies for Gd-Based Responsive Magnetic Resonance Imaging Contrast Agents. *Current Opinion in Chemical Biology* **2013**, *17* (2), 158–166. https://doi.org/10.1016/j.cbpa.2012.10.031.

(73) Aime, S.; Botta, M.; Esteban-Gómez, D.; Platas-Iglesias, C. Characterisation of Magnetic Resonance Imaging (MRI) Contrast Agents Using NMR Relaxometry. *Molecular Physics* **2019**, *117* (7–8), 898–909. https://doi.org/10.1080/00268976.2018.1516898.

(74) Campbell-Washburn, A. E.; Ramasawmy, R.; Restivo, M. C.; Bhattacharya, I.; Basar, B.; Herzka, D. A.; Hansen, M. S.; Rogers, T.; Bandettini, W. P.; McGuirt, D. R.; Mancini, C.; Grodzki, D.; Schneider, R.; Majeed, W.; Bhat, H.; Xue, H.; Moss, J.; Malayeri, A. A.; Jones, E. C.; Koretsky, A. P.; Kellman, P.; Chen, M. Y.; Lederman, R. J.; Balaban, R. S. Opportunities in Interventional and Diagnostic Imaging by Using High-Performance Low-Field-Strength MRI. *Radiology* **2019**, *293* (2), 384–393. https://doi.org/10.1148/radiol.2019190452.

(75) Lurie, D. J.; Aime, S.; Baroni, S.; Booth, N. A.; Broche, L. M.; Choi, C.-H.; Davies, G. R.; Ismail, S.; Ó hÓgáin, D.; Pine, K. J. Fast Field-Cycling Magnetic Resonance Imaging. *Comptes Rendus. Physique* **2010**, *11* (2), 136–148. https://doi.org/10.1016/j.crhy.2010.06.012.

(76) Irving, H. M.; Miles, M. G.; Pettit, L. D. A Study of Some Problems in Determining the Stoicheiometric Proton Dissociation Constants of

Complexes by Potentiometric Titrations Using a Glass Electrode. *Analytica Chimica Acta* **1967**, *38*, 475–488. https://doi.org/10.1016/S0003-2670(01)80616-4.

(77) Zekany, L.; Nagypal, I. PSEQUAD: A Comprehensive Program for the Evaluation of Potentiometric and/or Spectrophotometric Equilibrium Data Using Analytical Derivatives. In *Computational Methods for the Determination of Formation Constants*; Leggett, D. J., Ed.; Springer US: Boston, MA, 1985; pp 291–353. https://doi.org/10.1007/978-1-4684-4934-1_8.

(78) Meiboom, S.; Gill, D. Modified Spin-Echo Method for Measuring Nuclear Relaxation Times. *Review of Scientific Instruments* **1958**, *29* (8), 688–691. https://doi.org/10.1063/1.1716296.

(79) Solomon, I. Relaxation Processes in a System of Two Spins. *Phys. Rev.* **1955**, *99* (2), 559–565. https://doi.org/10.1103/PhysRev.99.559.

(80) Bloembergen, N.; Morgan, L. O. Proton Relaxation Times in Paramagnetic Solutions. Effects of Electron Spin Relaxation. *The Journal of Chemical Physics* **1961**, *34* (3), 842–850. https://doi.org/10.1063/1.1731684.

(81) Freed, J. H. Dynamic Effects of Pair Correlation Functions on Spin Relaxation by Translational Diffusion in Liquids. II. Finite Jumps and Independent *T* 1 Processes. *The Journal of Chemical Physics* **1978**, *68* (9), 4034–4037. https://doi.org/10.1063/1.436302.

(82) McLachlan, A. D. Line Widths of Electron Resonance Spectra in Solution. *Proc. R. Soc. Lond. A* **1964**, *280* (1381), 271–288. https://doi.org/10.1098/rspa.1964.0145.

(83) Raiford, D. S.; Fisk, C. L.; Becker, E. D. Calibration of Methanol and Ethylene Glycol Nuclear Magnetic Resonance Thermometers. *Anal. Chem.* **1979**, *51* (12), 2050–2051. https://doi.org/10.1021/ac50048a040.

(84) Yerly, F. VISUALISEUR/OPTIMISEUR 3.3.7., 2006.

(85) Supkowski, R. M.; Horrocks, W. DeW. On the Determination of the Number of Water Molecules, q, Coordinated to Europium(III) Ions in Solution from Luminescence Decay Lifetimes. *Inorganica Chimica Acta* **2002**, *340*, 44–48. https://doi.org/10.1016/S0020-1693(02)01022-8.

(86) Beeby, A.; Clarkson, I. M.; Dickins, R. S.; Faulkner, S.; Parker, D.; Royle, L.; De Sousa, A. S.; Williams, J. A. G.; Woods, M. Non-Radiative Deactivation of the Excited States of Europium, Terbium and Ytterbium Complexes by Proximate Energy-Matched OH, NH and CH Oscillators: An Improved Luminescence Method for Establishing Solution Hydration States. *J. Chem. Soc., Perkin Trans. 2* **1999**, No. 3, 493–504. https://doi.org/10.1039/a808692c.

(87) Frisch, M. J.; Trucks, G. W.; Schlegel, H. B.; Scuseria, G. E.; Robb, M. A.; Cheeseman, J. R.; Scalmani, G.; Barone, V.; Mennucci, B.;

Petersson, G. A.; Nakatsuji, H.; Caricato, M.; Li, X.; Hratchian, H. P.; Izmaylov, A. F.; Bloino, J.; Zheng, G.; Sonnenberg, J. L.; Hada, M.; Ehara, M.; Toyota, K.; Fukuda, R.; Hasegawa, J.; Ishida, M.; Nakajima, T.; Honda, Y.; Kitao, O.; Nakai, H.; Vreven, T.; Montgomery Jr., J. A.; Peralta, J. E.; Ogliaro, F.; Bearpark, M. J.; Heyd, J.; Brothers, E. N.; Kudin, K. N.; Staroverov, V. N.; Kobayashi, R.; Normand, J.; Raghavachari, K.; Rendell, A. P.; Burant, J. C.; Iyengar, S. S.; Tomasi, J.; Cossi, M.; Rega, N.; Millam, N. J.; Klene, M.; Knox, J. E.; Cross, J. B.; Bakken, V.; Adamo, C.; Jaramillo, J.; Gomperts, R.; Stratmann, R. E.; Yazyev, O.; Austin, A. J.; Cammi, R.; Pomelli, C.; Ochterski, J. W.; Martin, R. L.; Morokuma, K.; Zakrzewski, V. G.; Voth, G. A.; Salvador, P.; Dannenberg, J. J.; Dapprich, S.; Daniels, A. D.; Farkas, Ö.; Foresman, J. B.; Ortiz, J. V.; Cioslowski, J.; Fox, D. J. Gaussian 09, Gaussian, Inc.: Wallingford, CT, USA, 2009. .

(88) Tao, J.; Perdew, J. P.; Staroverov, V. N.; Scuseria, G. E. Climbing the Density Functional Ladder: Nonempirical Meta–Generalized Gradient Approximation Designed for Molecules and Solids. *Phys. Rev. Lett.* **2003**, *91* (14), 146401. https://doi.org/10.1103/PhysRevLett.91.146401.

(89) Staroverov, V. N.; Scuseria, G. E.; Tao, J.; Perdew, J. P. Comparative Assessment of a New Nonempirical Density Functional: Molecules and Hydrogen-Bonded Complexes. *The Journal of Chemical Physics* **2003**, *119* (23), 12129–12137. https://doi.org/10.1063/1.1626543.

(90) Grimme, S.; Ehrlich, S.; Goerigk, L. Effect of the Damping Function in Dispersion Corrected Density Functional Theory. *J Comput Chem* **2011**, *32* (7), 1456–1465. https://doi.org/10.1002/jcc.21759.

(91) Dolg, M.; Stoll, H.; Savin, A.; Preuss, H. Energy-Adjusted Pseudopotentials for the Rare Earth Elements. *Theoret. Chim. Acta* **1989**, *75* (3), 173–194. https://doi.org/10.1007/BF00528565.

(92) Andrae, D.; H�u�ermann, U.; Dolg, M.; Stoll, H.; Preu�, H. Energy-Adjustedab Initio Pseudopotentials for the Second and Third Row Transition Elements. *Theoret. Chim. Acta* **1990**, *77* (2), 123–141. https://doi.org/10.1007/BF01114537.

(93) Tomasi, J.; Mennucci, B.; Cammi, R. Quantum Mechanical Continuum Solvation Models. *Chem. Rev.* **2005**, *105* (8), 2999–3094. https://doi.org/10.1021/cr9904009.

(94) Hedegård, E. D.; Kongsted, J.; Sauer, S. P. A. Optimized Basis Sets for Calculation of Electron Paramagnetic Resonance Hyperfine Coupling Constants: Aug-Cc-pVTZ-J for the 3d Atoms Sc–Zn. *J. Chem. Theory Comput.* **2011**, *7* (12), 4077–4087. https://doi.org/10.1021/ct200587k.

(95) Marenich, A. V.; Cramer, C. J.; Truhlar, D. G. Universal Solvation Model Based on Solute Electron Density and on a Continuum Model of the Solvent Defined by the Bulk Dielectric Constant and Atomic

Surface Tensions. *J. Phys. Chem. B* **2009**, *113* (18), 6378–6396. https://doi.org/10.1021/jp810292n.
(96) Neese, F. The ORCA Program System. *WIREs Comput Mol Sci* **2012**, *2* (1), 73–78. https://doi.org/10.1002/wcms.81.
(97) Rega, N.; Cossi, M.; Barone, V. Development and Validation of Reliable Quantum Mechanical Approaches for the Study of Free Radicals in Solution. *The Journal of Chemical Physics* **1996**, *105* (24), 11060–11067. https://doi.org/10.1063/1.472906.
(98) Neese, F.; Wennmohs, F.; Hansen, A.; Becker, U. Efficient, Approximate and Parallel Hartree–Fock and Hybrid DFT Calculations. A 'Chain-of-Spheres' Algorithm for the Hartree–Fock Exchange. *Chemical Physics* **2009**, *356* (1–3), 98–109. https://doi.org/10.1016/j.chemphys.2008.10.036.
(99) Izsák, R.; Neese, F. An Overlap Fitted Chain of Spheres Exchange Method. *The Journal of Chemical Physics* **2011**, *135* (14), 144105. https://doi.org/10.1063/1.3646921.
(100) Vögtle, F.; Weber, E. Krakenmoleküle. *Angewandte Chemie* **1974**, *86* (24), 896–898. https://doi.org/10.1002/ange.19740862407.
(101) Gibson, M. S.; Bradshaw, R. W. The Gabriel Synthesis of Primary Amines. *Angew. Chem. Int. Ed. Engl.* **1968**, *7* (12), 919–930. https://doi.org/10.1002/anie.196809191.
(102) Su, H.; Wu, C.; Zhu, J.; Miao, T.; Wang, D.; Xia, C.; Zhao, X.; Gong, Q.; Song, B.; Ai, H. Rigid Mn(Ii) Chelate as Efficient MRI Contrast Agent for Vascular Imaging. *Dalton Trans.* **2012**, *41* (48), 14480. https://doi.org/10.1039/c2dt31696j.
(103) Clough, T. J.; Jiang, L.; Wong, K.-L.; Long, N. J. Ligand Design Strategies to Increase Stability of Gadolinium-Based Magnetic Resonance Imaging Contrast Agents. *Nat Commun* **2019**, *10* (1), 1420. https://doi.org/10.1038/s41467-019-09342-3.
(104) Tircsó, G.; Molnár, E.; Csupász, T.; Garda, Z.; Botár, R.; Kálmán, F. K.; Kovács, Z.; Brücher, E.; Tóth, I. 2 Gadolinium(III)-Based Contrast Agents for Magnetic Resonance Imaging. A Re-Appraisal. In *Metal Ions in Bio-Imaging Techniques*; Sigel, A., Freisinger, E., Sigel, R. K. O., Eds.; De Gruyter, 2021; pp 39–70. https://doi.org/10.1515/9783110685701-008.
(105) Stetter, H.; Frank, W.; Mertens, R. Darstellung und komplexbildung von polyazacycloalkan-N-essigsäuren. *Tetrahedron* **1981**, *37* (4), 767–772. https://doi.org/10.1016/S0040-4020(01)97695-1.
(106) Bottino, F.; Di Grazia, M.; Finocchiaro, P.; Fronczek, F. R.; Mamo, A.; Pappalardo, S. Reaction of Tosylamide Monosodium Salt with Bis(Halomethyl) Compounds: An Easy Entry to Symmetrical N-Tosyl Aza Macrocycles. *J. Org. Chem.* **1988**, *53* (15), 3521–3529. https://doi.org/10.1021/jo00250a020.

(107) Kumar, K.; Chang, C. A.; Tweedle, M. F. Equilibrium and Kinetic Studies of Lanthanide Complexes of Macrocyclic Polyamino Carboxylates. *Inorg. Chem.* **1993**, *32* (5), 587–593. https://doi.org/10.1021/ic00057a017.

(108) Mato-Iglesias, M.; Roca-Sabio, A.; Pálinkás, Z.; Esteban-Gómez, D.; Platas-Iglesias, C.; Tóth, É.; De Blas, A.; Rodríguez-Blas, T. Lanthanide Complexes Based on a 1,7-Diaza-12-Crown-4 Platform Containing Picolinate Pendants: A New Structural Entry for the Design of Magnetic Resonance Imaging Contrast Agents. *Inorg. Chem.* **2008**, *47* (17), 7840–7851. https://doi.org/10.1021/ic800878x.

(109) Dumas, S.; Jacques, V.; Sun, W.-C.; Troughton, J. S.; Welch, J. T.; Chasse, J. M.; Schmitt-Willich, H.; Caravan, P. High Relaxivity Magnetic Resonance Imaging Contrast Agents Part 1: Impact of Single Donor Atom Substitution on Relaxivity of Serum Albumin-Bound Gadolinium Complexes. *Investigative Radiology* **2010**, *45* (10), 600–612. https://doi.org/10.1097/RLI.0b013e3181ee5a9e.

(110) Jacques, V.; Dumas, S.; Sun, W.-C.; Troughton, J. S.; Greenfield, M. T.; Caravan, P. High-Relaxivity Magnetic Resonance Imaging Contrast Agents Part 2: Optimization of Inner- and Second-Sphere Relaxivity. *Investigative Radiology* **2010**, *45* (10), 613–624. https://doi.org/10.1097/RLI.0b013e3181ee6a49.

(111) CHANG, Y. M.; BAEK, A. R. NOVEL COMPOUND AND MRI CONTRAST AGENT CONTAINING SAME. WO 2022/092602, August 2, 2023.

(112) Caravan, P. D.; Jacques, V.; Dumas, S.; Sun, W.-C.; Zhou, K. L.; Schmitt-Willich, H. High Relaxivity Chelates. WO 2008/098056 A2, August 14, 2008.

(113) Baranyai, Z.; Pálinkás, Z.; Uggeri, F.; Brücher, E. Equilibrium Studies on the Gd^{3+}, Cu^{2+} and Zn^{2+} Complexes of BOPTA, DTPA and DTPA-BMA Ligands: Kinetics of Metal-Exchange Reactions of $[Gd(BOPTA)]^{2-}$. *Eur. J. Inorg. Chem.* **2010**, *2010* (13), 1948–1956. https://doi.org/10.1002/ejic.200901261.

(114) Baranyai, Z.; Uggeri, F.; Giovenzana, G. B.; Bényei, A.; Brücher, E.; Aime, S. Equilibrium and Kinetic Properties of the Lanthanoids(III) and Various Divalent Metal Complexes of the Heptadentate Ligand AAZTA. *Chemistry A European J* **2009**, *15* (7), 1696–1705. https://doi.org/10.1002/chem.200801803.

(115) Tircsó, G.; Kovács, Z.; Sherry, A. D. Equilibrium and Formation/Dissociation Kinetics of Some Ln^{III} PCTA Complexes. *Inorg. Chem.* **2006**, *45* (23), 9269–9280. https://doi.org/10.1021/ic0608750.

(116) Desreux, J. F.; Merciny, E.; Loncin, M. F. Nuclear Magnetic Resonance and Potentiometric Studies of the Protonation Scheme of Two Tetraaza

Tetraacetic Macrocycles. *Inorg. Chem.* **1981**, *20* (4), 987–991. https://doi.org/10.1021/ic50218a008.

(117) Cacheris, W. P.; Nickle, S. K.; Sherry, A. D. Thermodynamic Study of Lanthanide Complexes of 1,4,7-Triazacyclononane-N,N',N"-Triacetic Acid and 1,4,7,10-Tetraazacyclododecane-N,N',N",N'''-Tetraacetic Acid. *Inorg. Chem.* **1987**, *26* (6), 958–960. https://doi.org/10.1021/ic00253a038.

(118) Clark, L. W. THE DECARBOXYLATION OF MALONIC ACID IN ACID MEDIA. *J. Phys. Chem.* **1960**, *64* (1), 41–43. https://doi.org/10.1021/j100830a010.

(119) Zara, C. L.; Jin, T.; Giguere, R. J. Microwave Heating in Organic Synthesis: Decarboxylation of Malonic Acid Derivatives in Water. *Synthetic Communications* **2000**, *30* (12), 2099–2104. https://doi.org/10.1080/00397910008087388.

(120) Kenyon, J.; Ross, W. A. 749. The Mechanism of the Decarboxylation of Substituted Malonic Acid Derivatives. *J. Chem. Soc.* **1951**, 3407. https://doi.org/10.1039/jr9510003407.

(121) Trost, B. M.; Fleming, I. *Comprehensive Organic Synthesis: Selectivity, Strategy, and Efficiency in Modern Organic Chemistry*, 1st ed.; Pergamon Press: Oxford, England New York, 1991.

(122) Powell, D. H.; Dhubhghaill, O. M. N.; Pubanz, D.; Helm, L.; Lebedev, Y. S.; Schlaepfer, W.; Merbach, A. E. Structural and Dynamic Parameters Obtained from ^{17}O NMR, EPR, and NMRD Studies of Monomeric and Dimeric Gd^{3+} Complexes of Interest in Magnetic Resonance Imaging: An Integrated and Theoretically Self-Consistent Approach ^{1}. *J. Am. Chem. Soc.* **1996**, *118* (39), 9333–9346. https://doi.org/10.1021/ja961743g.

(123) Laurent, S.; Elst, L. V.; Muller, R. N. Comparative Study of the Physicochemical Properties of Six Clinical Low Molecular Weight Gadolinium Contrast Agents. *Contrast Media Mol Imaging* **2006**, *1* (3), 128–137. https://doi.org/10.1002/cmmi.100.

(124) Aime, S.; Calabi, L.; Cavallotti, C.; Gianolio, E.; Giovenzana, G. B.; Losi, P.; Maiocchi, A.; Palmisano, G.; Sisti, M. $[Gd\text{-}AAZTA]^{-}$: A New Structural Entry for an Improved Generation of MRI Contrast Agents. *Inorg. Chem.* **2004**, *43* (24), 7588–7590. https://doi.org/10.1021/ic0489692.

(125) Lalli, D.; Carniato, F.; Tei, L.; Platas-Iglesias, C.; Botta, M. Surprising Complexity of the $[Gd(AAZTA)(H_2O)_2]^{-}$ Chelate Revealed by NMR in the Frequency and Time Domains. *Inorg. Chem.* **2022**, *61* (1), 496–506. https://doi.org/10.1021/acs.inorgchem.1c03194.

(126) Aime, S.; Botta, M.; Crich, S. G.; Giovenzana, G.; Pagliarin, R.; Sisti, M.; Terreno, E. NMR Relaxometric Studies of Gd(III) Complexes with Heptadentate Macrocyclic Ligands. *Magn. Reson. Chem.* **1998**, *36*

(S1), S200–S208. https://doi.org/10.1002/(SICI)1097-458X(199806)36:13<S200::AID-OMR324>3.0.CO;2-H.

(127) Leone, L.; Guarnieri, L.; Martinelli, J.; Sisti, M.; Penoni, A.; Botta, M.; Tei, L. Rigid and Compact Binuclear Bis-hydrated Gd-complexes as High Relaxivity MRI Agents. *Chemistry A European J* **2021**, *27* (46), 11811–11817. https://doi.org/10.1002/chem.202101701.

(128) Lammers, H.; Maton, F.; Pubanz, D.; van Laren, M. W.; van Bekkum, H.; Merbach, A. E.; Muller, R. N.; Peters, J. A. Structures and Dynamics of Lanthanide(III) Complexes of Sugar-Based DTPA-Bis(Amides) in Aqueous Solution: A Multinuclear NMR Study. *Inorg. Chem.* **1997**, *36* (12), 2527–2538. https://doi.org/10.1021/ic961359k.

(129) Váradi, B.; Lihi, N.; Bunda, S.; Nagy, A.; Simon, G.; Kéri, M.; Papp, G.; Tircsó, G.; Esteban-Gómez, D.; Platas-Iglesias, C.; Kálmán, F. K. Physico-Chemical Characterization of a Highly Rigid Gd(III) Complex Formed with a Phenanthroline Derivative Ligand. *Inorg. Chem.* **2022**, *61* (34), 13497–13509. https://doi.org/10.1021/acs.inorgchem.2c02050.

(130) Esteban-Gómez, D.; de Blas, A.; Rodríguez-Blas, T.; Helm, L.; Platas-Iglesias, C. Hyperfine Coupling Constants on Inner-Sphere Water Molecules of Gd ^{III} -Based MRI Contrast Agents. *ChemPhysChem* **2012**, *13* (16), 3640–3650. https://doi.org/10.1002/cphc.201200417.

(131) Gupta, A.; Caravan, P.; Price, W. S.; Platas-Iglesias, C.; Gale, E. M. Applications for Transition-Metal Chemistry in Contrast-Enhanced Magnetic Resonance Imaging. *Inorg. Chem.* **2020**, *59* (10), 6648–6678. https://doi.org/10.1021/acs.inorgchem.0c00510.

(132) Rivera-Mancía, S.; Ríos, C.; Montes, S. Manganese Accumulation in the CNS and Associated Pathologies. *Biometals* **2011**, *24* (5), 811–825. https://doi.org/10.1007/s10534-011-9454-1.

(133) Drahoš, B.; Kotek, J.; Hermann, P.; Lukeš, I.; Tóth, É. Mn $^{2+}$ Complexes with Pyridine-Containing 15-Membered Macrocycles: Thermodynamic, Kinetic, Crystallographic, and ^{1} H/ ^{17} O Relaxation Studies. *Inorg. Chem.* **2010**, *49* (7), 3224–3238. https://doi.org/10.1021/ic9020756.

(134) Rolla, G. A.; Platas-Iglesias, C.; Botta, M.; Tei, L.; Helm, L. ^{1} H and ^{17} O NMR Relaxometric and Computational Study on Macrocyclic Mn(II) Complexes. *Inorg. Chem.* **2013**, *52* (6), 3268–3279. https://doi.org/10.1021/ic302785m.

VIII. Appendix

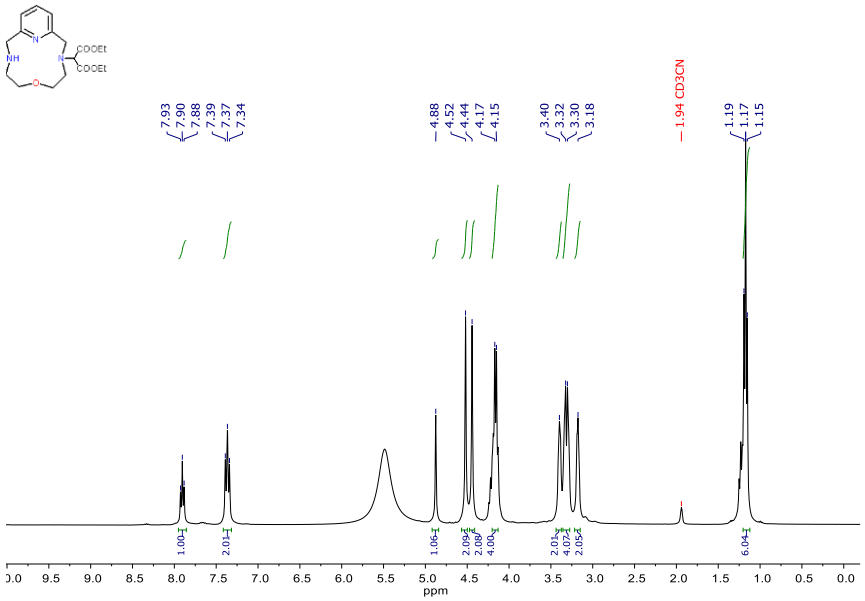

Figure A1. ^{1}H-NMR spectrum of OPMMA diethyl ester (CD_3CN).

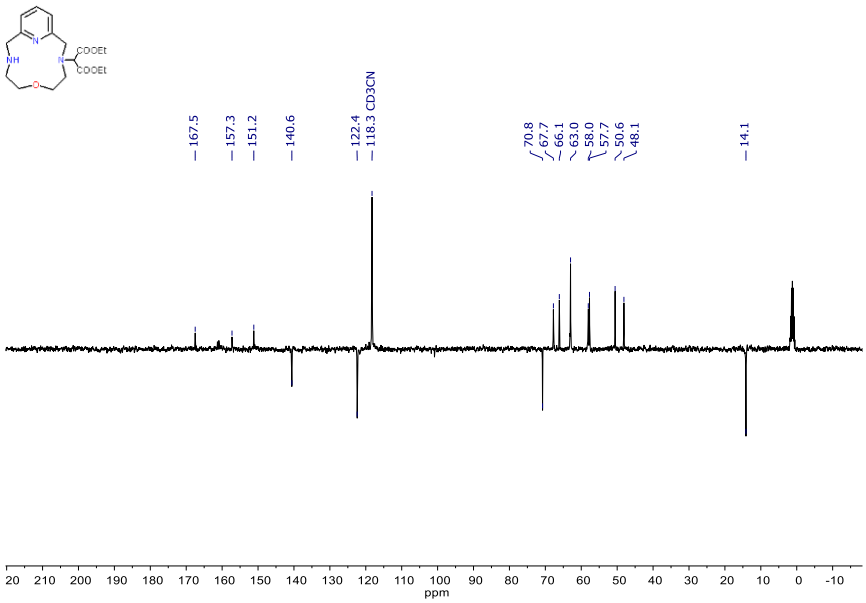

Figure A2. ^{13}C-NMR spectrum of OPMMA diethyl ester (CD_3CN, reference: TMS).

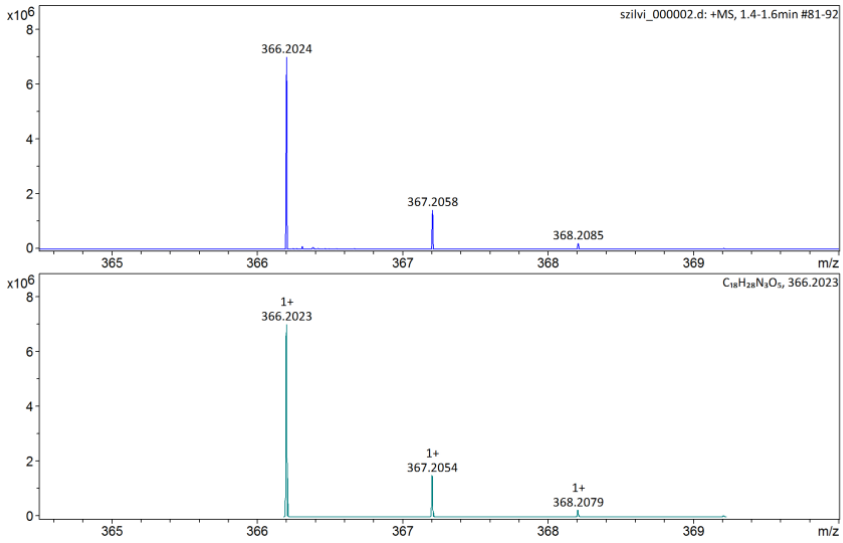

Figure A3. MS spectra of OPMMA diethyl ester.

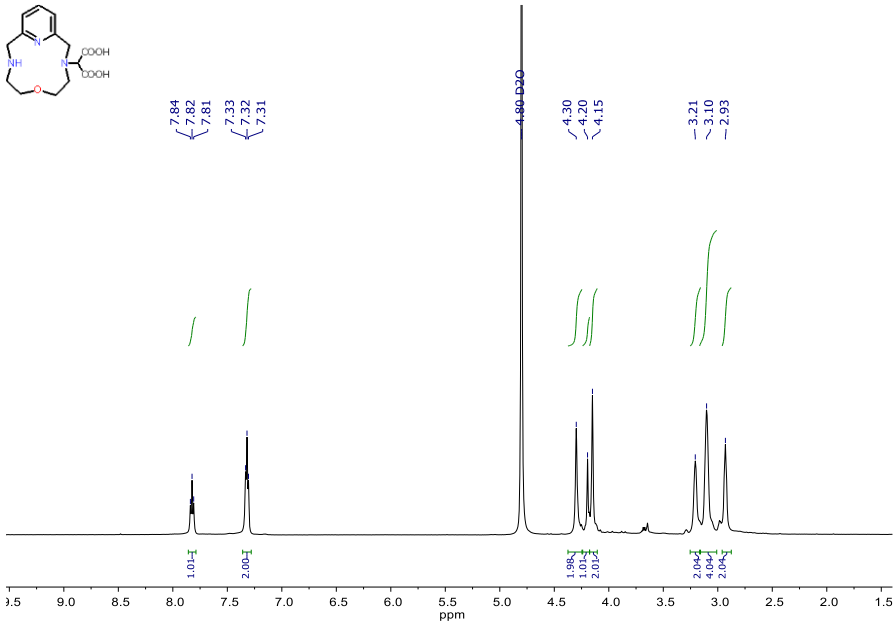

Figure A4. ^{1}H-NMR spectrum of H_2OPMMA (D_2O).

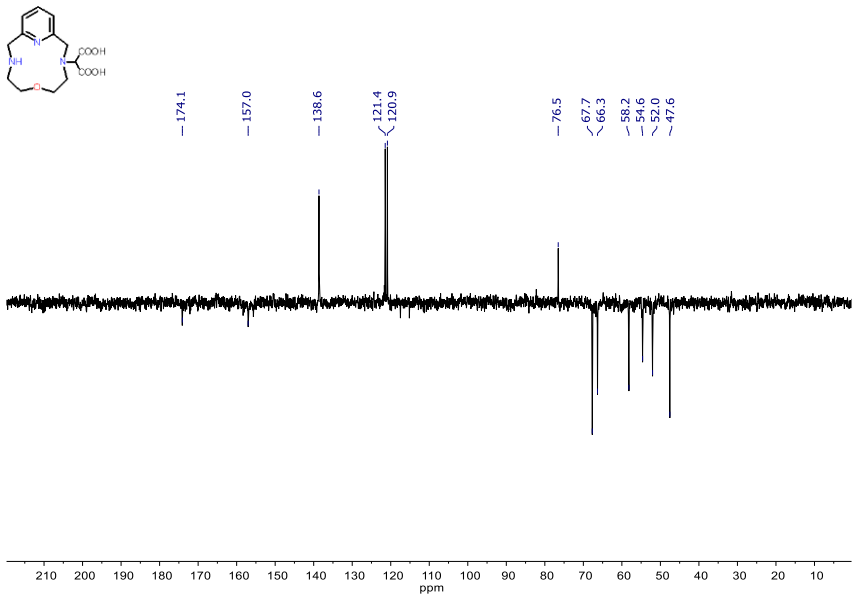

Figure A5. ^{13}C-NMR spectrum of H_2OPMMA (D_2O).

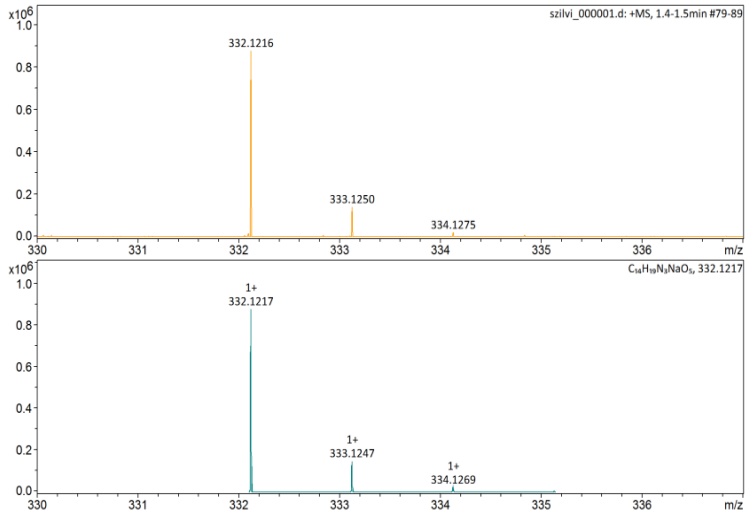

Figure A6. MS spectra of H_2OPMMA.

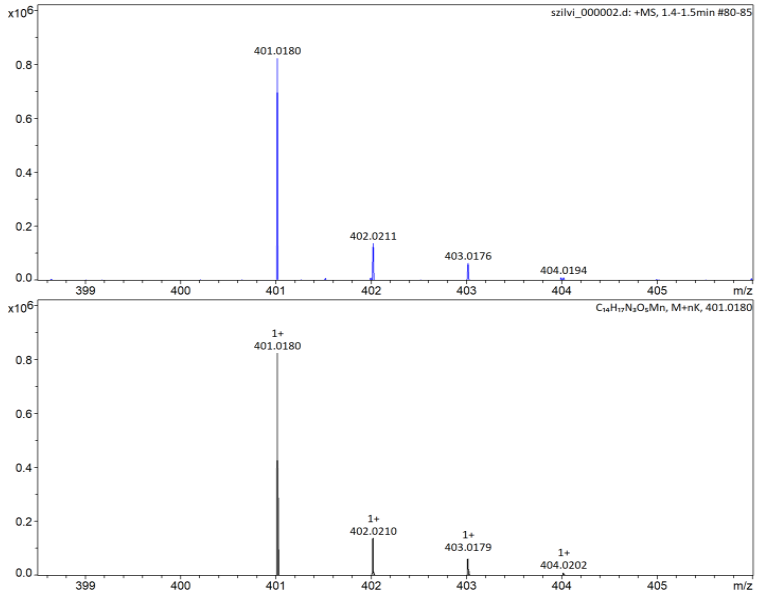

Figure A7. MS spectra of $[Mn(OPMMA)]^{-}$ complex. ESI-MS (positive mode): $[M+Mn+K]^{+}_{calc.}$: 401.0180; $[M+Mn+K]^{+}_{found}$:. 401.0180.

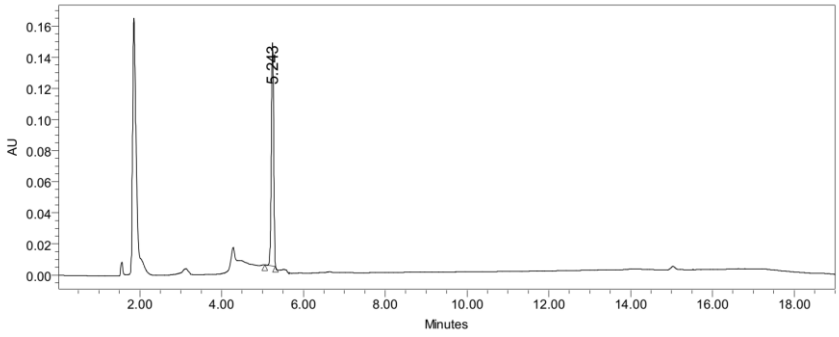

Figure A8. Analytical HPLC chromatogram of [Mn(OPMMA)] complex (t_R= 5.243 min).

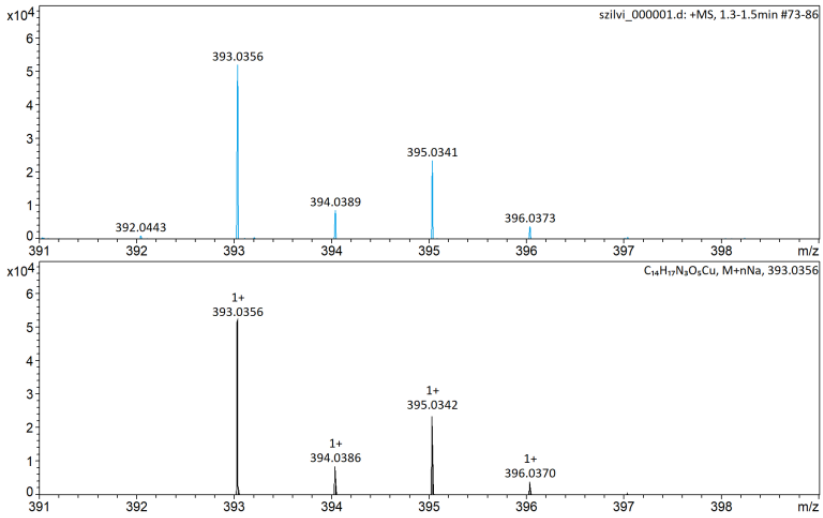

Figure A9. MS spectra of $[Cu(OPMMA)]^-$ complex. ESI-MS (positive mode): $[M+Cu+Na]^+_{calc.}$: 393.0356; $[M+Cu+Na]^+_{found}$:. 393.0356.

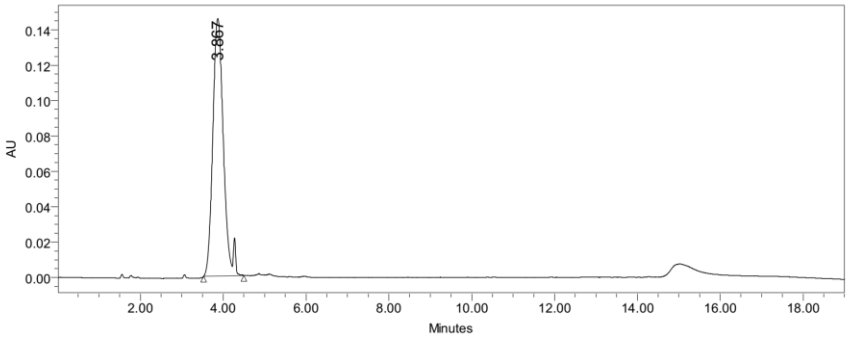

Figure A10. Analytical HPLC chromatogram of [Cu(OPMMA)] complex (t_R= 3.867 min).

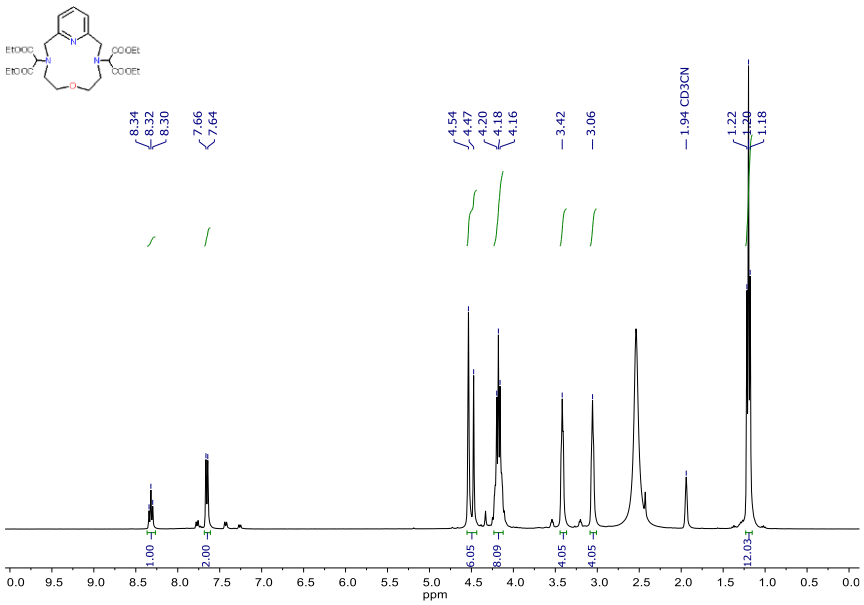

Figure A11. ^{1}H-NMR spectrum of OPDMA tetraethyl ester ligand **(**CD_3CN).

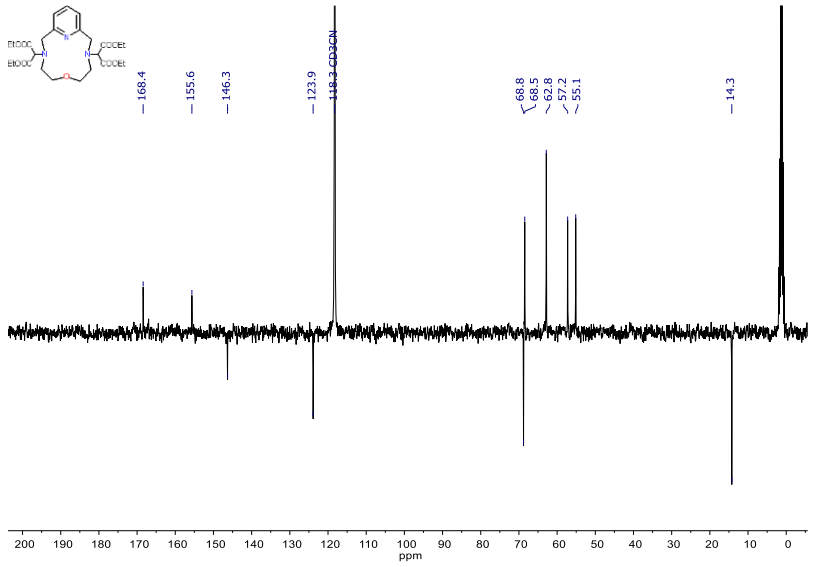

Figure A12.^{13}C-NMR spectrum of OPDMA tetraethyl ester ligand **(**CD_3CN, reference: TMS).

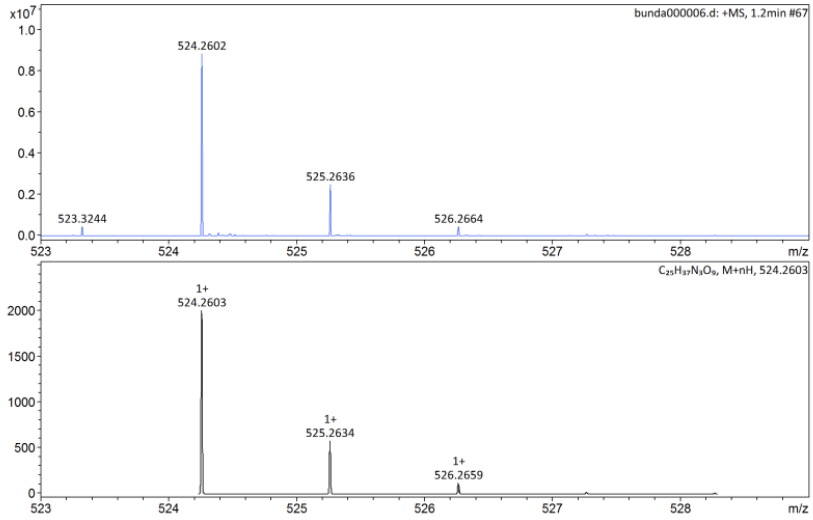

Figure A13. MS spectra of OPDMA tetraethyl ester ligand.

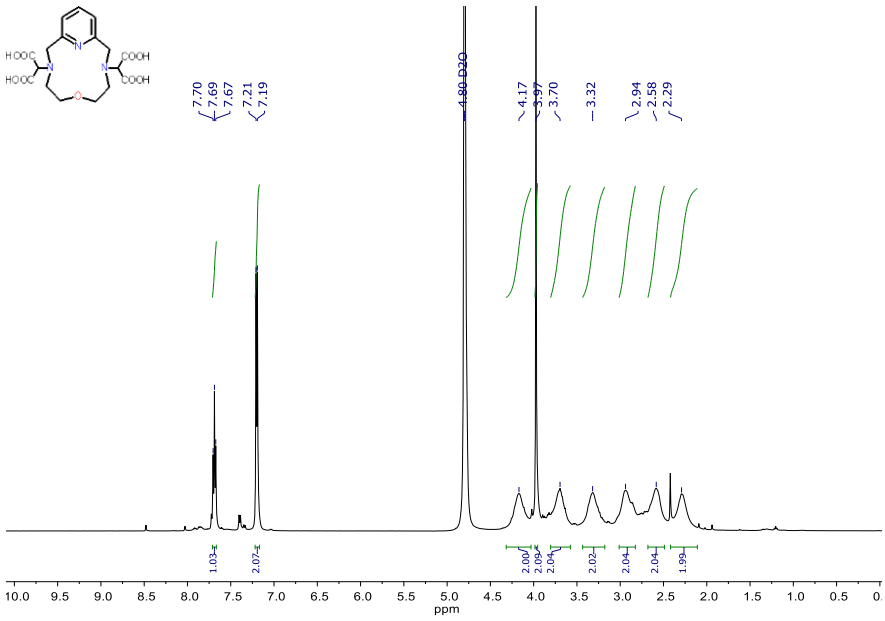

Figure A14. ^{1}H-NMR spectrum of H_4OPDMA ligand (D_2O).

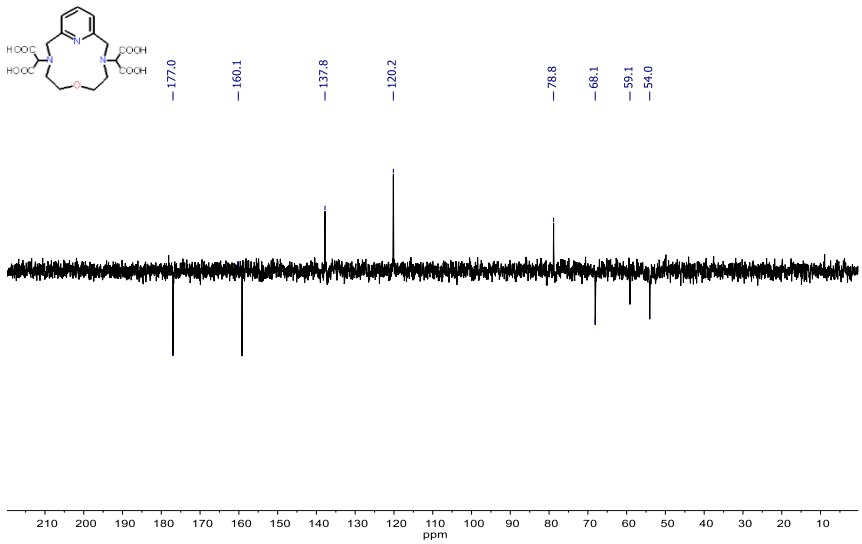

Figure A15. ^{13}C-NMR spectrum of H_4OPDMA ligand (D_2O).

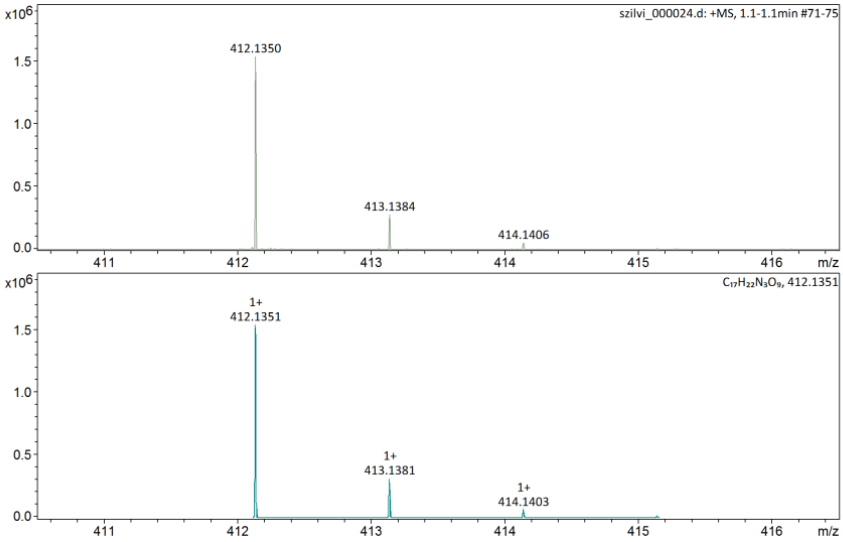

Figure A16. MS spectra of H_4OPDMA ligand.

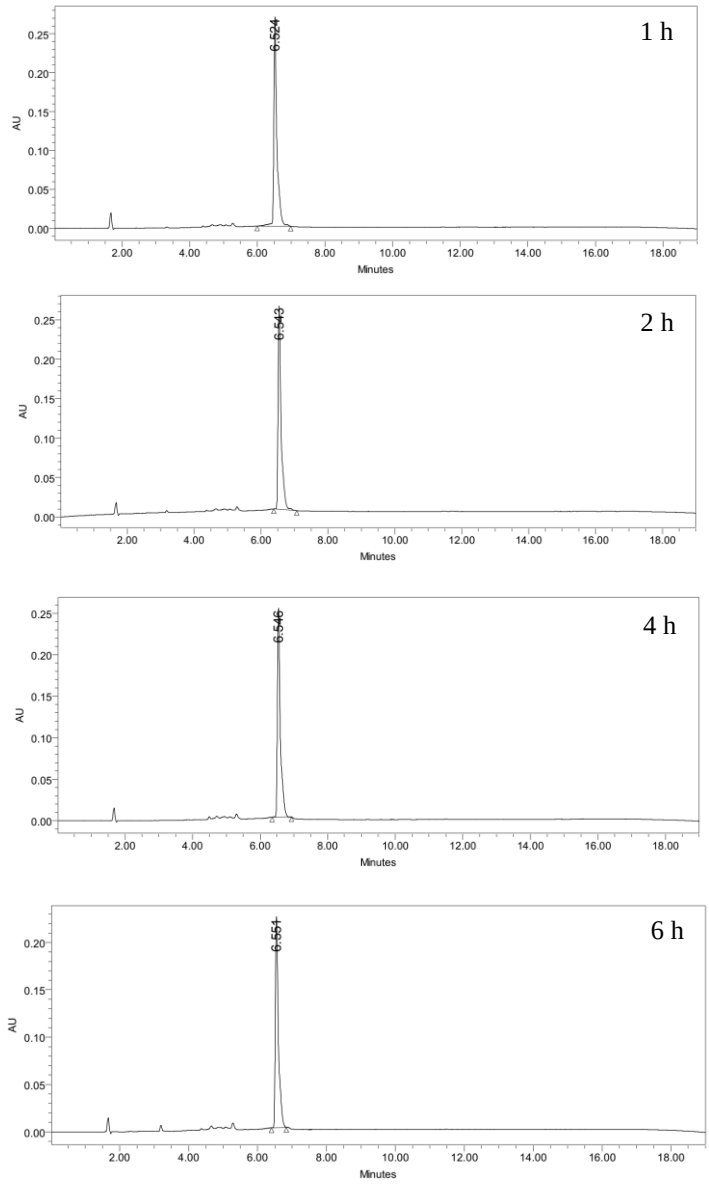

Figure A17. Stability determination of H_4OPDMA ligand in 1.0 M HCl solution in a 6 hours time period.

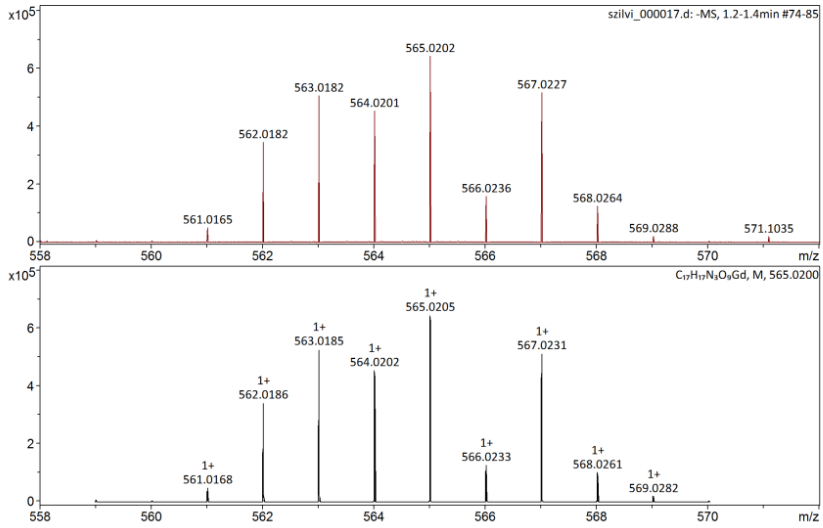

Figure A18. MS spectra of $[Gd(OPDMA)]^-$ complex. ESI-MS (negative mode): $[M+H]^-_{calc.}$: 565.0205; $[M+H]^-_{found}$: 565.0202.

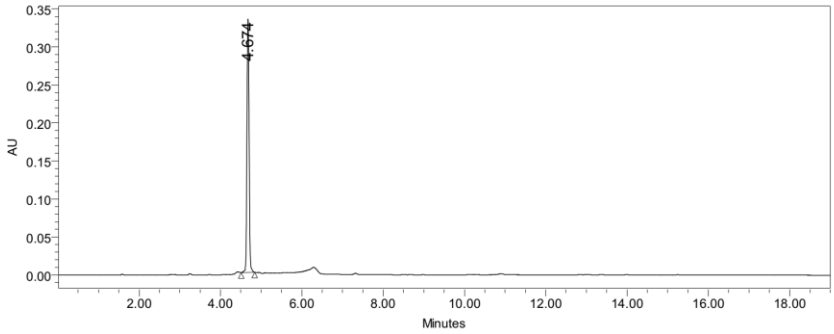

Figure A19. Analytical HPLC chromatogram of $[Gd(OPDMA)]^-$ complex (t_R= 4.674 min).

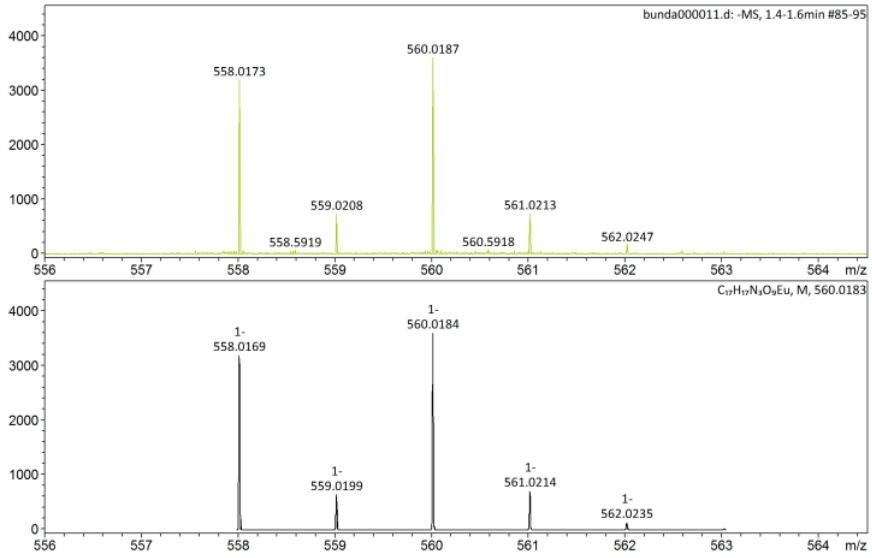

Figure A20. MS spectra of $[Eu(OPDMA)]^{-}$ complex.

ESI-MS (negative mode): $[M+H]^{-}_{calc.}$: 560.0184, $[M+H]^{-}_{found}$: 560,0187.

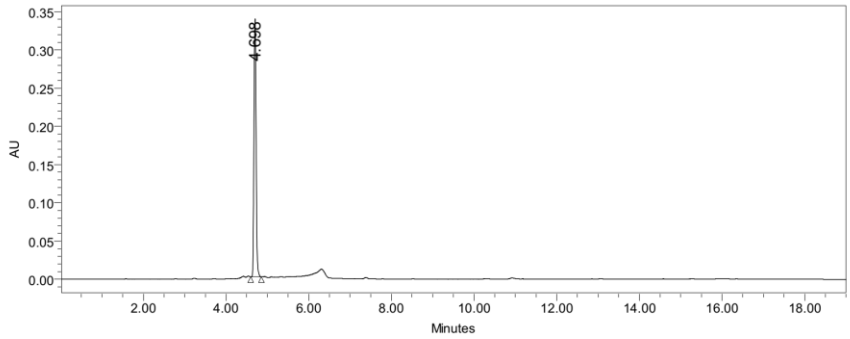

Figure A21. Analytical HPLC chromatogram of $[Eu(OPDMA)]^{-}$ complex (t_R= 4.698 min).

DFT calculations

Table A1. Energy and Cartesian coordinates of the heptadentate $[Gd(H_2O)(OPDMA)]^-$ complex.

Sum of electronic and zero-point Energies (Eh)	-1765.240359
Sum of electronic and thermal Energies (Eh)	-1765.207159
Sum of electronic and enthalpy Energies (Eh)	-1765.206214
Sum of electronic and thermal Free Energies (Eh)	-1765.302858
Number of Imaginary Frequencies	0

Molecular Geometry in Cartesian Coordinates

C	-1.999414	2.424559	-0.116483
C	-3.026641	1.328666	-0.185132
H	-3.474264	1.225203	0.806589
H	-3.834302	1.609511	-0.871080
C	-2.349761	-0.138399	-2.035877
H	-3.309149	0.071926	-2.525740
C	-1.288221	0.776037	-2.626378
C	-2.351615	3.751993	-0.352159
H	-3.375090	4.000847	-0.604592
C	-1.367863	4.732108	-0.277863
H	-1.611999	5.772364	-0.458083
N	-0.742739	2.057727	0.196477
N	-2.449063	0.019301	-0.563771
C	0.216769	3.002160	0.215177
C	1.611356	2.535276	0.518793
H	1.717282	2.505281	1.606747
H	2.344221	3.259248	0.141962
C	2.223315	1.199709	-1.447631
H	2.978991	1.959403	-1.686418
H	2.638445	0.233181	-1.716601
C	0.989729	1.471091	-2.295239
C	-0.058141	4.349587	-0.007542
H	0.746449	5.074207	0.013982
N	1.924568	1.176216	0.006530
H	-2.078830	-1.175806	-2.239038
H	0.593475	2.481074	-2.146766
H	1.252190	1.355398	-3.351145
H	-1.176894	0.569756	-3.694701
H	-1.545505	1.833809	-2.500509
O	-0.038575	0.518284	-1.958286
C	-3.240515	-1.050127	0.094010
H	-4.302419	-1.004786	-0.160260
C	-3.042659	-0.892275	1.633202
O	-3.979088	-1.146629	2.389944

O	-1.851158	-0.526295	1.964821
C	-2.668010	-2.435914	-0.242609
O	-3.408094	-3.388793	-0.469592
O	-1.372562	-2.462058	-0.194966
O	1.179676	-1.979439	-1.129247
H	2.049191	-1.946104	-1.605164
H	0.991531	-2.937636	-0.975730
C	3.035065	0.675115	0.888825
H	3.789497	1.462562	1.001732
C	3.776541	-0.583780	0.341561
O	3.551270	-1.677511	0.891659
O	4.560892	-0.359619	-0.634184
C	2.432603	0.358702	2.272173
O	3.147824	0.467916	3.268868
O	1.190330	-0.016898	2.271681
Gd	-0.079874	-0.466762	0.363317
O	3.559678	-2.014230	-2.403009
H	3.584312	-1.540212	-3.243540
H	4.101552	-1.454717	-1.771768
O	0.270823	-4.486023	-0.605197
H	-0.513383	-3.911099	-0.403806
H	0.573908	-4.800052	0.256056

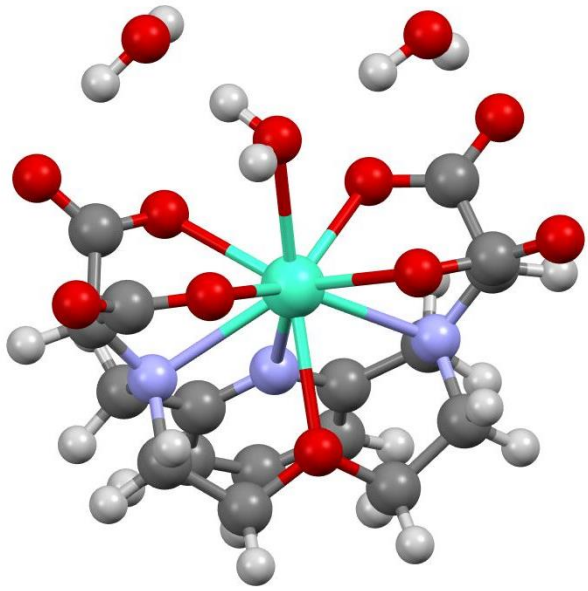

Figure A22. DFT calculated structure of the nonacoordinate $[Gd(H_2O)(OPDMA)]^-$ complex.

Table A2. Energy and Cartesian coordinates of the nonacoordinate $[Gd(H_2O)(OPDMA)]^-$ complex.

Electronic Energy (Eh)	-1765.68142946
Sum of electronic and zero-point Energies (Eh)	-1765.259684
Sum of electronic and thermal Energies (Eh)	-1765.226293
Sum of electronic and enthalpy Energies (Eh)	-1765.225349
Sum of electronic and thermal Free Energies (Eh)	-1765.32162
Number of Imaginary Frequencies	0

Molecular Geometry in Cartesian Coordinates

C	2.182482	1.866957	-1.095986
C	3.021852	0.667306	-0.728015
H	3.084451	0.022482	-1.606429
H	4.041052	0.987803	-0.481936
C	2.797054	0.426739	1.705822
H	3.876833	0.610922	1.779808
C	2.058420	1.716426	1.999478

C	2.769042	3.026017	-1.600639
H	3.844321	3.079051	-1.719325
C	1.954931	4.107684	-1.921216
H	2.385429	5.022199	-2.311985
N	0.850708	1.758762	-0.923888
N	2.435863	-0.123329	0.377970
C	0.068273	2.825191	-1.184017
C	-1.406090	2.667370	-0.902864
H	-1.870879	2.226382	-1.787168
H	-1.865066	3.650281	-0.744006
C	-1.533255	2.468005	1.542960
H	-2.074903	3.422807	1.533442
H	-1.976022	1.833034	2.309535
C	-0.085531	2.730494	1.904597
C	0.585299	4.014047	-1.693317
H	-0.074227	4.851533	-1.884685
N	-1.666312	1.767299	0.243079
H	2.524438	-0.312196	2.459063
H	0.385640	3.440518	1.216003
H	-0.027163	3.141360	2.917071
H	2.268506	2.038391	3.023838
H	2.354956	2.520562	1.316778
O	0.642903	1.487674	1.851287
C	2.797988	-1.553757	0.256126
H	3.876712	-1.732114	0.270289
C	2.161824	-2.123014	-1.034444
O	2.586331	-3.200567	-1.488348
O	1.157125	-1.468922	-1.481917
C	2.112835	-2.348369	1.406518
O	2.717764	-3.255738	1.970722
O	0.896585	-1.967843	1.624694
O	-1.067100	-2.765113	-0.128875
H	-0.707829	-3.148467	0.686263
H	-0.637756	-3.275260	-0.871834
O	0.093870	-4.149867	-2.151731
H	1.036552	-3.867739	-2.039954
H	-0.198169	-3.654586	-2.928164
O	-3.856193	-2.795769	-0.743546
H	-2.914165	-2.778880	-0.490953
H	-3.973996	-1.962452	-1.230137
C	-2.986534	1.107562	0.114208
H	-3.821196	1.813480	0.097164
C	-3.162960	0.106211	1.295305
O	-4.267969	-0.028475	1.816906
O	-2.077770	-0.524977	1.592490
C	-2.994743	0.231540	-1.161304
O	-4.078259	-0.029953	-1.700574
O	-1.843552	-0.226165	-1.504020
Gd	-0.158665	-0.343140	0.186426

Table A3. Energy values and Cartesian coordinates of [Mn(OPMMA)] complex.

Electronic Energy (Eh)	-2465.2113339
Sum of electronic and zero-point Energies (Eh)	-2464.825005
Sum of electronic and thermal Energies (Eh)	-2464.796012
Sum of electronic and enthalpy Energies (Eh)	-2464.795068
Sum of electronic and thermal Free Energies (Eh)	-2464.885553
Number of Imaginary Frequencies	0

Molecular Geometry in Cartesian Coordinates

C	-1.691665	-0.828839	1.555729
C	-0.628924	-1.908015	1.501318
H	0.059355	-1.746945	2.334844
H	-1.091755	-2.888525	1.662912
C	-0.451483	-2.735098	-0.805358
H	-0.727259	-3.721423	-0.409432
C	-1.677289	-2.097702	-1.435722
C	-2.818713	-0.932545	2.364704
H	-2.972711	-1.812162	2.977863
C	-3.744676	0.104422	2.353035
H	-4.633165	0.048691	2.970726
N	-1.484427	0.247223	0.787667
N	0.136914	-1.879391	0.242918
Mn	0.330893	0.338793	-0.543585
C	-2.390326	1.230845	0.738637
C	-2.072599	2.370703	-0.205598
H	-1.543556	3.147953	0.352990
H	-3.003292	2.813767	-0.577044
C	-1.892511	1.426239	-2.504121
H	-2.736306	2.069335	-2.782958
H	-1.172668	1.436265	-3.324550
C	-2.405764	0.012491	-2.306810
C	-3.540558	1.197935	1.518651
H	-4.264043	2.001958	1.461694
N	-1.192217	1.940052	-1.307185
H	0.299798	-2.884012	-1.580610
H	-3.161566	-0.032149	-1.514025
H	-2.864599	-0.345851	-3.234566
H	-2.048349	-2.734181	-2.246238
H	-2.486114	-1.968047	-0.707450
H	-0.623501	2.730264	-1.592937
O	-1.296553	-0.818318	-1.953646
C	1.582605	-2.092313	0.429142
H	1.832820	-3.090229	0.798408
C	2.126058	-1.017098	1.405112
O	2.988128	-1.326762	2.232861
O	1.627637	0.154509	1.223945
C	2.320127	-1.823552	-0.910607

O	3.288294	-2.528166	-1.216202
O	1.861703	-0.827056	-1.576010
O	1.826915	1.865701	-1.509596
H	2.440599	1.147915	-1.740298
H	2.336958	2.515984	-0.977780
O	2.450333	2.464953	2.530214
H	2.190564	1.603640	2.130015
H	2.737777	2.995479	1.767941
O	3.204405	3.783012	0.004070
H	4.156557	3.815837	-0.164484
H	2.887638	4.683599	-0.152942